

DESIGN AND DEVELOPMENT OF A MARINE CURRENT
ENERGY CONVERSION SYSTEM USING HYBRID
VERTICAL AXIS TURBINE

MD. JAHANGIR ALAM



**DESIGN AND DEVELOPMENT OF A MARINE CURRENT
ENERGY CONVERSION SYSTEM USING HYBRID
VERTICAL AXIS TURBINE**

BY

© MD. JAHANGIR ALAM

**A THESIS SUBMITTED TO THE SCHOOL OF GRADUATE STUDIES
IN PARTIAL FULFILMENT OF THE REQUIREMENTS FOR THE DEGREE OF
MASTER OF ENGINEERING**

**FACULTY OF ENGINEERING AND APPLIED SCIENCE
MEMORIAL UNIVERSITY OF NEWFOUNDLAND
ST. JOHN'S, NEWFOUNDLAND**

JULY, 2009

.....*To my beloved parents and wife*

Abstract

The Ocean Network Seafloor Instrumentation (ONSFI) Project, which commenced in 2007, is a five year multidisciplinary R&D project to design, fabricate and validate a proof-of-concept seafloor array of wireless marine sensors for use in monitoring seabed processes, including applications such as geological imaging and earthquake detection. Individual compact, low-cost sensors, called 'SEAformatics' pods, will be self-powered through ocean bottom currents and will be able to communicate with each other and to the Internet through surface master units to facilitate observation of the ocean floor from shore.

One of approaches to power the SEAformatics sensor pods is using small marine current turbines that are equipped with an energy conversion system. For such application of a turbine, main constraint is a very low cut-in speed. Slow ocean currents require a low cut-in speed marine current turbine for continuous power to those pods. To alleviate the water speed issue, a self starting, low cut-in speed hybrid vertical axis marine current turbine have been designed and developed at the Faculty of Engineering and Applied Science, Memorial University of Newfoundland. The developed marine current power generation system is composed of the designed hybrid vertical axis turbine, a permanent magnet generator, an ac-dc rectifier, a dc-dc converter and a battery. The hybrid vertical axis turbine is designed with a drag type *Savonius* and a lift type *Darrieus* turbines. Moreover, the battery is required for the stand-alone applications of marine current power generation systems. In order to get maximum available power at load side, a low cost microcontroller based maximum power point tracker have been developed as a part of proposed energy conversion system . This thesis provides details of system design and test results.

Acknowledgements

“*Appreciation*” might not be an appropriate word to be used for those individuals who were directly or indirectly associated with this research work. Because, their contributions are worth much more than the word itself can express.

My first appreciation is for Dr. Tariq Iqbal, who was directly associated in introducing a sophisticated technology related to the sustainable future development in the area of power system. I really acknowledge his contribution in guiding me in the design and development of a successful turbine with its other signal conditioning circuits. He has been a really good mentor throughout this time. He did not only guide me throughout this research technically; He also spurred my ability to accommodate myself in a new environment, here in Canada. I had really a great honor to work with such an individual, who was humble even during the hard times, to show me the right track and boost up my confidence in this research.

I really appreciate the co-operation of Dr. Michael Hinchey and Dr. Vlastimil Masek. Their efforts have been ceaseless in implementing the design idea into its final form. Their experience and knowledge has also assisted in shaping the research work in a fruitful manner.

I am also delighted to acknowledge Paul Bishop and Brian Pretty, who were directly involved in making the prototype in its final form, and assisting me in testing the hybrid turbine.

There are many other people who have triggered my enthusiasm since the beginning. I greatly appreciate the contribution of my beloved parents Md. Ansar Ali and Gul Nehar Begam, who deserve the real honors for this achievement. Their love and guidance

Acknowledgements

assisted in making my dream come true. I cannot deny the endless support of my brothers and sister, throughout this time. It cannot adequately express the contribution of my beloved wife, Rizvi Sultana, with words. She was really caring, loving and the source of inspiration for this success. Endless support from my friends is greatly appreciated. Their company assisted me in going through the challenging situations. I can never forget it.

List of Figures

Figure 1.1 A block diagram of a marine current energy conversion system.....4

Figure 1.2 Turbine Output Power (P) vs. Turbine/Rotor Speed (ω).....5

Figure 2.1 Ocean Tides (spring and neap).....10

Figure 2.2 Gulf Stream.....13

Figure 2.3 Global Thermohaline Circulation.....14

Figure 2.4 The North Atlantic Current (MGSVA representation).....16

Figure 2.5 Classification of MCT.....17

Figure 2.6 Vertical Axis Water Current Turbines (VAWCT).....19

Figure 2.7 Davis Turbine.....20

Figure 2.8 Horizontal Axis Water Current Turbines (HAWCT).....21

Figure 2.9 MCT's "Seaflow" (left) & Artists impression of "Seagen" (right).....23

Figure 2.10 Stingray device elements (Left) and its demonstration (Right).....24

Figure 3.1 (a) Savonius View (b) Direction of Rotation.....30

Figure 3.2 Characteristic curves of several conventional rotors (C_p vs. λ).....32

Figure 3.3 The Savonius rotor:
(a) Front view (single step) (b) top view (with a central shaft).....33

Figure 3.4 A four bladed H-Darrieus turbine (top view).....34

Figure 3.5 Two Possible Hybrid Configurations of Darrieus and Savonius Rotor.....37

Figure 3.6 Designed Prototype (Snap Shot).....40

Figure 3.7 Expected Output Power of Hybrid Turbine.....41

Figure 3.8 (a) Aluminum sheets (b) Styrofoam pieces (c) piece of Renshape.....42

Figure 3.9 Hydrodynamics of the hybrid turbine.....44

Figure 4.1 Flume Tank (Left), Immersed Hybrid Turbine (Right).....48

Figure 4.2 Torque and speed data collection.....49

Figure 4.3 DAQ Board and Data Collection Terminal.....50

Figure 4.4 Associated parts (CAD View, SolidWorks).....51

Figure 4.5 (a) Double step Savonius turbine (b) Experimental power output52

Figure 4.6 The H-Darrieus Turbine (a) 4-bladed prototype (b) power output.....53

Figure 4.7 C_{pd} vs. TSR (λ) for H- Darrieus turbine.....54

Figure 4.8 Power plots for the Savonius, Darrieus and hybrid turbine.....55

Figure 4.9 P vs. ω (Hybrid Turbine).....57

Figure 4.10 C_p vs. TSR (λ) for Hybrid Turbine.....58

Figure 5.1 Marine Current Energy Conversion System.....61

Figure 5.2 (a) Radial Flux and (b) Axial Flux PMG.....63

Figure 5.3 Basic Switching converter components.....68

Figure 5.4 (a) Fundamental switching converter circuit (b) voltage waveform across output resistor, R_L69

Figure 5.5 Voltage ratio and duty cycle of dc-dc converters71

Figure 5.6 Circuit diagram of a boost converter.....72

Figure 5.7 Waveforms for the boost converter.....73

Figure 5.8 Mode1 equivalent circuit for the boost converter ($0 < t \leq t_{on}$).....74

Figure 5.9 Mode2 equivalent circuit for the boost converter ($t_{on} \leq t < T$).....75

Figure 5.10 The schematic diagram of the designed boost converter (using microcontroller).....78

Figure 5.11 The designed dc-dc boost converter.....80

Figure 5.12 Output voltage vs. input voltage.....81

Figure 5.13 Output current vs. output voltage.....82

Figure 5.14 Output power vs. input voltage.....82

Figure 5.15 Efficiency vs. input voltage.....83

Figure 5.16 Generated PWM Signal with 66.67% Duty Ratio.....85

Figure 6.1 Conventional MPPT-based Energy Conversion Systems90

Figure 6.2 Control system based on wind-speed measurements (WG MPPT Method)...90

Figure 6.3 The structure of the proposed marine current energy conversion system with MPPT-based control.....93

Figure 6.4 The MPPT-based controlled power supply control blocks.....94

Figure 6.5 Conventional P & O Method.....95

Figure 6.6 MPPT Actions (Graphical View).....96

Figure 6.7 The MPPT Flow chart.....97

Figure 6.8 The experimental structure of the proposed marine current energy conversion system98

Figure 6.9 Experimental Marine Current Energy Conversion System (Lab Setup).....99

Figure 6.10 LTS 15-NP and its characteristic curve (right).....101

Figure 6.11 The LTS 15-NP current sensor (diagram, pin connections).....102

Figure 6.12 Voltage Sensor.....102

Figure 6.13 (a) Maximum Duty Ratio (when $V_{out} < V_{ref}$).....104

Figure 6.13 (b) Minimum Duty Ratio (when $V_{out} \geq V_{ref}$).....104

Figure 6.14 Maximum Duty Ratio (when $V_{out} < V_{ref}$).....105

List of Tables

Table 2.1 Mean potential tidal current energy (Canada).....11

Table 2.2 Average Water flow of St.John's, Newfoundland Areas.....16

Table 3.1 Comparison between Savonius and H- Darrieus Turbine.....36

Table 3.2 Turbine Specifications (For Hybrid Configuration).....39

Table 5.1 Designed Boost Converter Components.....80

Table 5.2 Pb-acid, NiCad and NiMH Battery Comparison.....87

Table 6.1 MPPT Actions.....96

Table 6.2 Component of the proposed MCECS.....100

List of Symbols

Mechanical Parameters

P_w	Available water power
V	Speed of Water
ω	Angular Velocity
$P = \tau\omega = P_{\text{mech}}$	Hydrodynamic Power
C_p	Turbine (Hybrid) Power Coefficient
$U = \omega \times R$	Tip Peripheral Velocity
A_a	Aspect Ratio (Savonius)
β	Overlap Ratio (Savonius)
$A = H \times D$	Rotor Swept Area
$\lambda = \frac{\omega R_d}{V}$	Tip Speed Ratio (Hybrid)
D_f	Drag Force
L_f	Lift Force
C_D	Drag Coefficient
C_L	Lift Coefficient
R_e	Reynolds Number
μ	Dynamic viscosity
α	Angle of Attack
a	Diameter of Central Shaft (Savonius)
r_a	Overlap

Electrical Parameters

V	Voltage
I	Current
P	Power
D	Duty Cycle
η	Conversion Efficiency
T_s	Switching Time Period
f_s	Switching Frequency
R	Resistance
L	Inductance
C	Capacitance

Design and Development of a Marine Current Energy Conversion System using Hybrid Vertical Axis Turbine

Table of Contents

Abstract	i
Acknowledgement	ii
List of Figures	iv
List of Tables	vii
List of Symbols	viii
Chapter -1: Introduction	1
1.0 Global Energy Review.....	1
1.1 Marine Current Energy.....	3
1.2 Marine Current Energy Conversion System.....	4
1.3 Thesis Objective.....	6
1.4 Thesis Outline.....	6
Chapter -2: Marine Current and Underwater Turbines	8
2.0 Introduction.....	8
2.1 Marine Currents.....	9
2.1.1 Tidal Currents.....	9
2.1.2 Wind Driven Currents.....	12
2.1.3 Thermohaline (THC) Circulation.....	13
2.3 North Atlantic Marine Current.....	15

2.4 Marine Current Turbines.....	17
2.4.1 Vertical Axis Water Current Turbine (VAWCT).....	18
2.4.1.1 VAWCTs Industrial Designs.....	19
2.4.2 Horizontal Axis Water Current Turbine (HAWCT).....	20
2.4.2.1 HAWCTs Industrial Designs.....	22
2.4.3 Reciprocating Hydrofoils (RH).....	23
2.4.3.1 RHs Industrial Designs.....	24
2.5 Environmental impact.....	25
2.6 Conclusion.....	27
Chapter -3: Hybrid Turbine Design.....	28
3.0 Introduction.....	28
3.1 Turbine selection.....	29
3.2 Savonius Rotor.....	29
3.3 H-Darrieus Rotor.....	34
3.4 The Darrieus-Savonius Hybrid Turbine.....	36
3.4.1 Possible Hybrid Configuration.....	37
3.4.2 Design Equations and Parameters.....	38
3.4.3 Material Selection.....	41
3.5 Hydrodynamics.....	43
3.6 Conclusion.....	45
Chapter -4: Experimental Setup and Test Results.....	47
4.0 Introduction.....	47
4.1 Experimental Setup.....	48
4.2.1 Associated parts.....	50

4.2 Test Results.....	51
4.2.1 Savonius turbine test results.....	52
4.2.2 Darrieus turbine test results.....	52
4.2.3 Hybrid turbine experimental test results.....	54
4.2.3.1 Electrical generated power with water speed.....	55
4.2.3.2 Electrical generated power with turbine speed.....	56
4.2.3.3 Power Coefficient (C_p) with Tip Speed Ratio (λ).....	57
4.3 Conclusion.....	59
Chapter -5: Marine Current Energy Conversion System (MCECS).....	60
5.0 Introduction.....	60
5.1 Marine Current Energy Conversion System (MCECS).....	61
5.2 Generator Selection for MCT.....	62
5.2.1 Permanent Magnet Generator.....	62
5.2.3 Cogging Torque.....	64
5.2.4 Elimination of Cogging Torque.....	65
5.2.5 Generator Losses.....	66
5.3 Power Electronic Converters.....	67
5.3.1 DC-DC Converter.....	67
5.3.2 Boost Converter Design Equations.....	72
5.3.3 Designed Boost Converter.....	78
5.3.3.1 Theoretical and Experimental results.....	80
5.3.3.2 Pulse Width Modulation (PWM).....	83
5.4 Energy Storage System.....	86
5.5 Conclusion.....	88

Chapter -6: Experimental Energy Conversion System.....	89
6.0 Introduction.....	89
6.1 Existing Energy Conversion Systems (MPPT based).....	90
6.2 Proposed MCECS.....	92
6.3 Maximum Power Point Tracking.....	93
6.3.1 Conventional P & O Method.....	95
6.3.2 Proposed MPPT Algorithm.....	96
6.4 Experimental setup of the proposed MCECS	98
6.4.1 Current Sensor.....	101
6.4.2 Voltage Sensor.....	102
6.5 Test Results.....	103
6.6 Conclusion.....	105
Chapter -7: Conclusions.....	106
7.0 Research Conclusion.....	106
7.1 Thesis Contribution.....	107
7.2 Future Work & Suggestions.....	108
Bibliography.....	110
Appendix A.....	114
Appendix B.....	121
Appendix C.....	132
Appendix D.....	135

CHAPTER 1

INTRODUCTION

1.0 Global Energy Overview

No doubt that the energy demand in this contemporary world is following an increasing trend since the past century and it is expected to grow even further and faster in the near future than ever before. Recent IEA (International Energy Agency) and other scenarios (OECD/IEA, 2008) have demonstrated that a large basket of sustainable energy technologies will be needed to address the challenges of moving towards clean, reliable, secure and competitive energy supply. Renewable energy sources (RES) and technologies (RETs) can play an important role in achieving this goal. Many countries

have made progress in promoting renewables in their energy production. However, there remain obstacles and required efforts to realize such trends of energy production. .

By the year of 2030, renewables are projected to contribute 29% to electric power generation and 7% of transport fuels according to the IEA *World Energy Outlook (WEO) Alternative Policy Scenario 2007*. Such policies are currently under consideration to be put in effect. By the year of 2050, the contribution of renewables could rise even further to almost 50% electric power generation if the ambitious goal of a 50% global reduction in CO₂ emissions over that time horizon is met (see the BLUE scenarios in the IEA *Energy Technology Perspectives (ETP) 2008*). While attainable, this objective will require very strong political and financial commitment as well as immediate action by all governments.

Modern renewable technologies have grown rapidly, overtaking gas to become the second-largest source of generated electric power, behind coal, soon after the year of 2010. Falling costs as renewable technologies mature, assumed higher fossil-fuel prices and strong policy support provide an opportunity for the renewable industry to eliminate its reliance on subsidies and to bring emerging technologies into the mainstream.

Excluding biomass, non-hydro renewable energy sources — wind, solar, geothermal, tide and wave energy — together grow faster than any other source worldwide, at an average rate of 7.2% per year over the projection period (OECD/IEA, 2008). Most of the increase occurs in the power sector.

Renewable resources are the source of energy replenished by the natural phenomena. Top 7 renewable resources are: Solar energy, Wind energy, Hydropower, Biomass energy, Hydrogen, Geothermal energy and Ocean energy.

Though the hydropower is used since long time in power sector, wind and solar energy industries have also started to contribute their production for stand-alone as well as grid-connected systems. In spite of having a higher energy density in ocean resources, their industrial production is in early stages. Several researches are still going on to harness the available energy in the ocean with an efficient energy conversion system.

1.1 Marine Current Energy

Marine currents are being recognized as a resource to be exploited for the sustainable generation of electrical power. The high load factors resulting from the fluid properties and the predictable resource characteristics make marine currents particularly attractive for electric power generation. These two factors makes electric power generation from marine currents much more appealing when compared to other renewables. Marine current turbine installations could also provide base grid power.

However, Speed and density of flowing bodies determine the kinetic energy that can be converted into mechanical energy using turbine. Though the wind speed is much higher than the water speed, water is about 835 times denser than wind. Worldwide, the total estimated power in ocean currents is about 5,000 GW, with power densities of up to 15kW/m^2 [1]. Marine currents utilized for electric power generation have the following advantages [1]:

- Marine (tidal) currents are predictable being dependent on the movement of tide; therefore unlike most of other renewables, the future availability of energy can be known and planned for.

- The resource is potentially large and can be exploited with little environmental impact, thereby offering one of the least damaging methods for large-scale electric power generation.
- A marine current turbine rated at 2–3 m/s in seawater can results in four times as much energy per year/m² of rotor swept area as similarly rated power wind turbine.
- Although accessing tidal stream energy may be costly, the high energy availability if exploited will more than to compensate for the higher costs.

The above mentioned advantages can provide motivations for a research to exploit the available marine energy for a clean and sustainable environment.

1.2 Marine Current Energy Conversion System

A marine current energy conversion system may consist of a mechanical device (for example, turbine) capable of converting water kinetic energy into mechanical energy, gearbox (if needed), a generator (from mechanical to electrical energy conversion), signal conditioning circuits (may include inverter, ac-dc rectifier, dc-dc converter, etc.) as well as an energy storage unit (for example; battery, for stand-alone application).

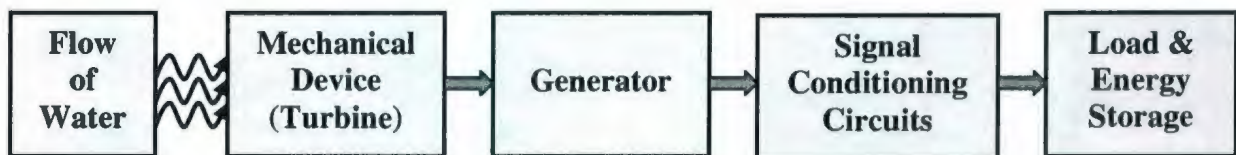


Figure 1.1 A block diagram of a marine current energy conversion system

The power available in water flow for a specific area is determined as,

$$P_w = 0.5 \times A \times \rho \times V^3 \quad (1.1)$$

Where,

P_w is the available water power (W)

ρ is the density of water (kg/m^3) (depends on water temperature, salinity etc.)

A is the area under consideration (m^2)

V is the speed of water (m/s)

Extractable power by the mechanical device (turbine) can be expressed as,

$$P = C_p \times 0.5 \times A \times \rho \times V^3 \quad (1.2)$$

Where, C_p is the percentage of power that can be extracted from the fluid stream and furthermore, takes into account losses due to Betz' law and those assigned to the internal mechanisms within the turbine. The percentage C_p is known as the power coefficient; that has a typical value of approximately 0.3 for a machine with low mechanical losses. In addition, the available water power may undergo further reductions due to power losses in the generator and signal conditioning circuits.

A marine current energy conversion may also consist of Maximum Power Point Tracker (MPPT). If the turbine output power is plotted with rotor speed for a particular water flow (Shown in figure 1.2), then for a particular turbine speed maximum power is achieved (MPP point). If the turbine power is tracked and maximum available power is delivered to the load, then the tracking device is known as maximum power point tracker.

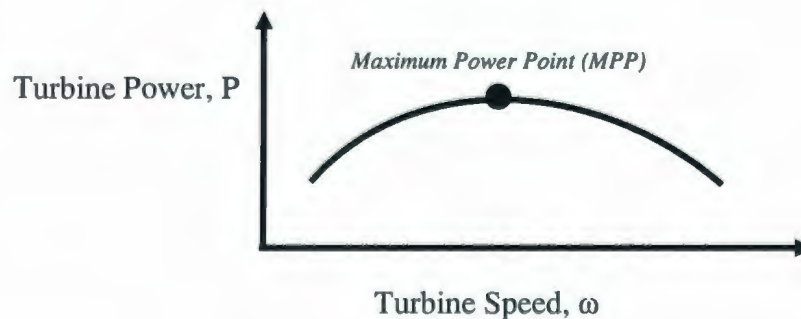


Figure 1.2 Turbine Output Power (P) vs. Turbine/Rotor Speed (ω)

1.3 Thesis Objective

The objective of the thesis is to design a marine current energy conversion system using a low cut-in speed hybrid vertical axis marine current turbine to meet the challenges in low speed North Atlantic marine currents. Marine currents data which are collected at the coastal areas of St.John's, Newfoundland, Canada, are employed in turbine design steps. However, this complete conversion system is intended to deploy at the sea bed for marine sensor power supply. The stand alone energy conversion system which has been studied in this research consists of a low cut-in speed hybrid vertical axis turbine, low speed permanent magnet generator, ac-dc rectifier, dc-dc converter and battery. A microcontroller based control system has been implemented comprising a Maximum Power Point Tracker.

1.4 Thesis Outline

This thesis is composed of seven chapters. Every chapter is organized to give specific information associated with this research work. Though the introduction is given at the beginning of every chapter, a brief information about the chapters is given below-

Chapter one provides the information about the necessity of clean energy development and emphasized in the arena of marine current energy conversion. This chapter provides the thesis objective as well.

Chapter two is enriched with the background information about the marine currents and their sources. Further information has been given on North Atlantic Current (NAC) and the situation of marine currents at the coastal areas of St.John's, Newfoundland, Canada.

Chapter three explains the design requirements for a specific turbine for low marine current application. In later part, it explains about the design details of a hybrid vertical axis turbine to meet those requirements.

Chapter four provides information about the turbine test setup. It also describes the test results of the designed hybrid vertical axis turbine.

Chapter five consists of information about Marine Current Energy Conversion System (MCECS) in details. A designed boost converter, with its test results is also explained.

Chapter six is composed of a laboratory setup for marine current energy conversion system with Maximum Power Point Tracker.

Chapter seven concludes the research work with research contribution and suggestions for future work.

CHAPTER 2

MARINE CURRENT AND UNDERWATER TURBINES

2.0 Introduction

This chapter introduces different types of marine currents and briefly illustrated their formation and behavior. In later part, North Atlantic Ocean current has been described. As a principal device for marine current energy conversion system, turbines are explained with some of their existing commercial designs. Lastly, some possible environmental impacts are pointed out from these type energy conversion devices.

2.1 Marine Currents

Horizontal movement of water is called current. Oceanic currents are driven by several factors. The first factor is the rise and fall of the tides, which is driven by the gravitational attraction of the sun and moon on Earth's oceans. Tides create a current in the oceans, near the shore, and in bays and estuaries along the coast. These are called "tidal currents." Tidal currents are the only type of currents that change in a very regular pattern and can be predicted for future dates.

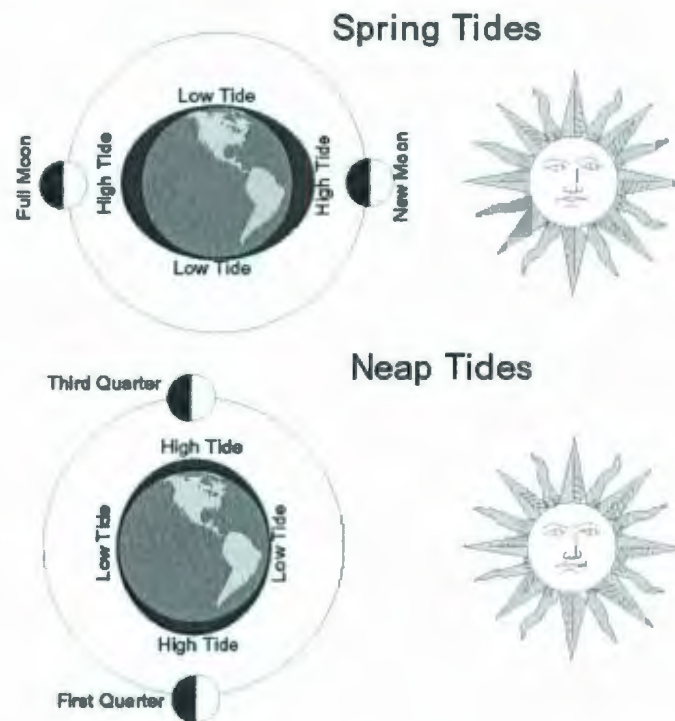
The *second* factor that drives ocean currents is wind. Winds drive currents that are at or near the ocean's surface. These currents are generally measured in meters per second or in knots (1 knot = 0.514 m/s or 1.15 miles per hour or 1.85 kilometers per hour). Winds drive currents near coastal areas on a localized scale and in the open ocean on a global scale.

The *third* factor that drives currents is thermohaline circulation - a process driven by density differences in water due to temperature (thermo) and salinity (haline) in different parts of the ocean. Currents driven by thermohaline circulation occur at both deep and shallow ocean levels and move much slower than tidal or surface currents.

2.1.1 Tidal Currents

Tides are the vertical rise and fall of the water. Tidal currents are the horizontal movement of the water caused by the tides. The gravitational attraction of the moon and sun affect the tides on Earth. The magnitude of this attraction depends on the mass of the object and its distance away, as described by the Newton's universal law of attraction. The moon has the greater effect on earth despite having less mass than the sun because it

is so much closer. The gravitational force of the moon causes the oceans to bulge along an axis pointing directly at the moon. The rotation of the earth causes the rise and fall of the tides. When the sun and moon are in line their gravitational attraction on the earth combine and cause a “spring” tide (see Figure 2.1). When they are as positioned in the figure below, 90° from each other, their individual gravitational attraction pulls water in different directions, causing a “neap” tide. However, the largest marine currents (due to tides) occur during the spring tide.



Source: www.atlantickayaktours.com

Figure 2.1 Ocean Tides (spring and neap)

The rotational period of the moon is around 4 weeks, while one rotation of the earth takes 24 hours; this results in a tidal cycle of around 12.5 hours. This tidal behavior is easily

predictable, which indicates that tidal energy could generate power over pre-defined periods of time.

According to the technical report by A. Cornett [2] from Canadian Hydraulics Centre, the mean potential tidal current energy in several places of Canada as provided in Table 2.1.

Table 2.1 Mean potential tidal current energy (Canada)

Province	Potential Tidal Current Energy (MW)	Number of Sites	Average Size(MW)
Northwest Territories	35	4	9
British Columbia	4,015	89	45
Québec	4,288	16	268
Nunavut	30,567	34	899
New Brunswick	636	14	45
PEI	33	4	8
Nova Scotia	2,122	15	141
Newfoundland	544	15	36
TOTAL	42,240	191	221

2.1.2 Wind Driven Currents

Wind driven currents are, as the name implies, currents that are created by the force of the wind exerting stress on the sea surface. This stress causes the surface water to move and this movement is transmitted to the underlying water to a depth that is dependent mainly on the strength and persistence of the wind. Most ocean currents are the result of winds that tend to blow in a given direction over considerable amounts of time. In many cases the strength of the wind may be used as a rule of thumb for determining the speed of the current.

A wind-driven current does not flow in exactly the same direction as the wind, but is deflected by Earth's rotation. The deflecting force (Coriolis force [3]) is greater at high latitudes and more effective in deep water. It is to the right of the wind direction in the Northern Hemisphere and to the left in the Southern Hemisphere. In general, the angular difference in direction between the wind and the surface current varies from about 10° in shallow coastal areas to as much as 45° in some open ocean areas. Each layer of a moving water sets the layer below in motion. Moreover, the layer below is then deflected by the Coriolis effect, causing the below layer to move to the right of the overlying layer. In general, deeper layers move more slowly because energy is lost in each transfer between layers. Some major wind-driven currents are the West Wind Drift in the Antarctic, the North and South Equatorial Currents that lie in the trade wind belts of the ocean, and the seasonal monsoon currents of the Western Pacific.

As an example of a wind driven current, The Gulf Stream, as represented by the Mariano Global Surface Velocity Analysis (MGSVA) [4, 5], is shown in figure 2.2. The Gulf Stream is the western boundary current of the N. Atlantic subtropical gyre, which

transports significant amount of warm water (heat) poleward. The averaging of velocity data from a meandering current produces a wide mean picture of the flow. The core of the Gulf Stream current is about 90 km wide and has peak velocities of greater than 2 m/s.

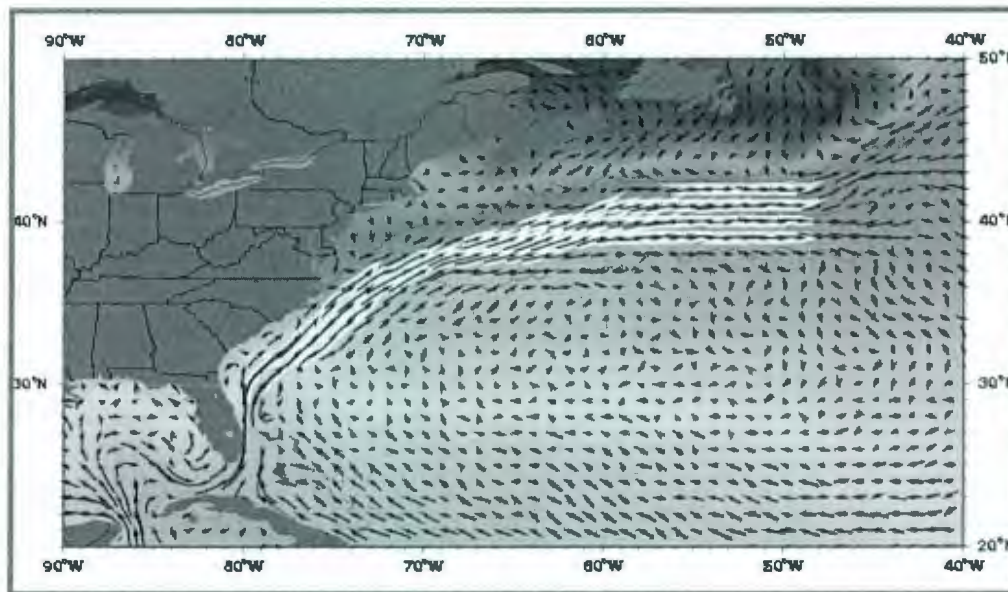
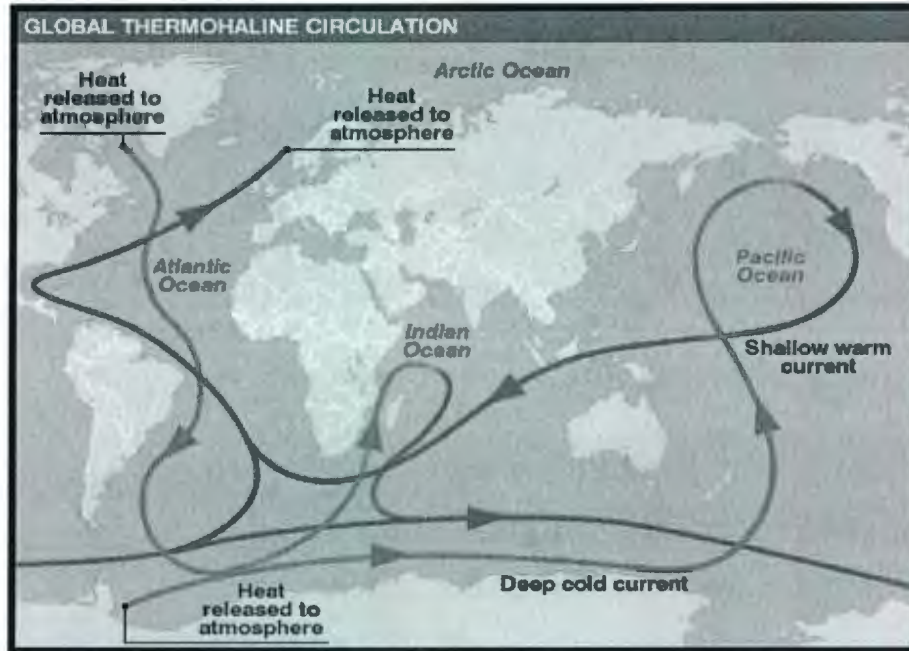


Figure 2.2 Gulf Stream

2.1.3 Thermohaline (THC) Circulation

As opposed to wind-driven currents and tides, the thermohaline circulation is that part of the ocean circulation which is driven by density differences. Sea water density depends on temperature and salinity, hence the name thermo-haline. The salinity and temperature differences arise from heating/cooling at the sea surface and from the surface freshwater fluxes (evaporation and sea ice formation enhance salinity; precipitation, runoff and ice-melt decrease salinity). Heat sources at the ocean bottom play a minor role. The Global Thermohaline Circulation is shown in Figure 2.3.



Source: www.acia.uaf.edu

Figure 2.3 Global Thermohaline Circulation

In contrast to the wind-driven currents, the THC is not confined to surface waters but can be regarded as a big overturning of the world ocean, from top to bottom. The thermohaline circulation consists of the followings,

- *Deep water formation:* the sinking of water masses, closely associated with convection, which is a vertical mixing process. Deep water formation takes place in a few localized areas: the Greenland-Norwegian Sea, the Labrador Sea, the Mediterranean Sea, the Wedell Sea, the Ross Sea.
- *Spreading of deep waters* (e.g., North Atlantic Deep Water, NADW, and Antarctic Bottom Water, AABW), mainly as Deep Western Boundary Currents (DWBC).

- *Upwelling of deep waters:* this is not as localized and difficult to observe. It is thought to take place mainly in the Antarctic Circumpolar Current region, possibly aided by the wind (Ekman divergence).
- *Near-surface currents:* these are required to close the flow. In the Atlantic, the surface currents compensating the outflow of NADW range from the Benguela Current off South Africa via Gulf Stream and North Atlantic Current into the Nordic Seas off Scandinavia (Note that the Gulf Stream is primarily a wind-driven current, as part of the subtropical gyre circulation. The thermohaline circulation contributes only roughly 20% to the Gulf Stream flow).

There are other physical characteristics which are associated with ocean currents are Salinity, Water temperature, Sediment Transport, Turbidity (measure of the ability of light to transmit down through the water column) etc.

2.3 North Atlantic Marine Current

The North Atlantic Current (NAC) originates between the Grand Banks and Mid Atlantic Ridge near the Newfoundland Ridge at the branch point of the Gulf Stream. In figure 2.4, the Gulf Stream is located at 40°N 50°W and the Slope Water current at 41°N 50°W [6]. The NAC represents the bulk of the Gulf Stream continuation past its branch point and comprised of waters from the Slope Water Current.

The NAC is strengthened by the Labrador Current as well. The Labrador Current flows from the Arctic Ocean south along the coast of Labrador and passes around Newfoundland, continuing south along the east coast of Nova Scotia. It is a continuation of the West Greenland Current and the Baffin Island Current.

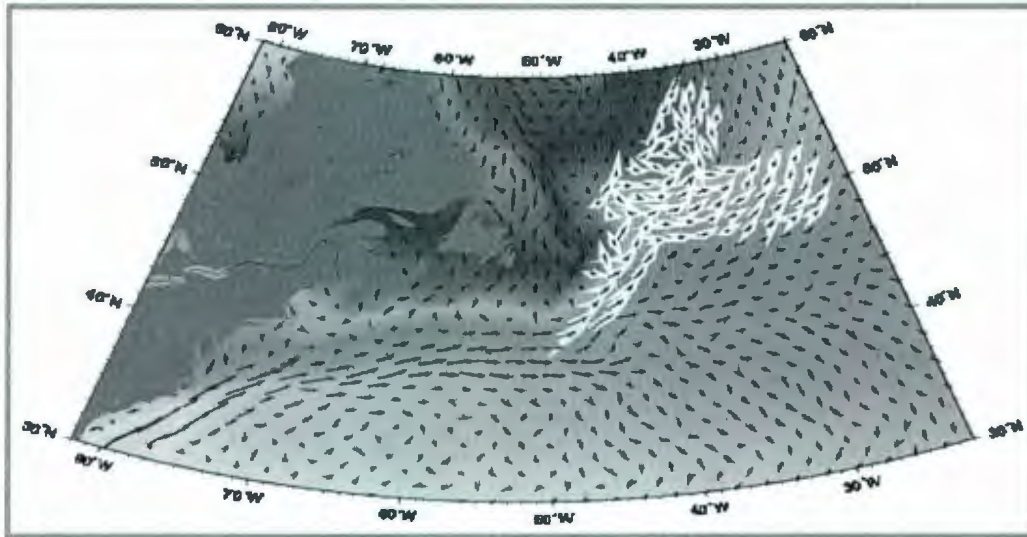


Figure 2.4 The North Atlantic Current (MGSVA representation)

Although, NACs are part of the Atlantic Ocean, these currents are more saline and cold (less than 90°C) than Pacific and Indian Ocean currents. These quantities directly affect the energy associated with marine current. Nevertheless, previous researches [found by Reynaud et al. (1995)] shown that the NAC speed can vary from 0.3 to 0.5 m/s.

From a Seaformatics group research [7], the water speed data (one-year hourly) for four different depths in the eastern part of St. John's are given in table 2.2.

Table 2.2 Average Water flow of St. John's, Newfoundland Areas

Water Depth (in m)	Average Water Flow (m/s)
20	0.146
45	0.132
80	0.112
Near Bottom	0.07

These data seems to be much less than the previous researches. It may be due to the sensors placed in different areas. However, the exploitation of marine current energy is likely to be in areas of high current speeds.

2.4 Marine Current Turbines

Marine Current Turbines (MCT) are used to exploit currents in the seas whether they are driven by the wind, tides or by oceanic circulations. This technology is part of a family of energy technologies at various stages of development, including tidal stream or tidal kinetic energy conversion, tidal barrage, wave, Ocean Thermal Energy Conversion, etc. These are collectively referred to as “marine renewables”. Marine current energy shares a number of advantages over other marine renewables and those under development, as well as over the more traditional energy generation technologies currently in use.

Marine current turbines are also known as underwater or hydrokinetic turbine. Based on the alignment of their rotor axis, with respect to water flow, these MCTs [8] could form two generic classes, namely, the axial flow and cross flow turbines. The axial turbines have axes parallel to the fluid flow and employ propeller type rotors. On the other hand, the cross flow types encounter water flow orthogonal to the rotor axis and mostly appear as cylindrical rotating structures. Different marine current turbines have shown in fig.2.5.

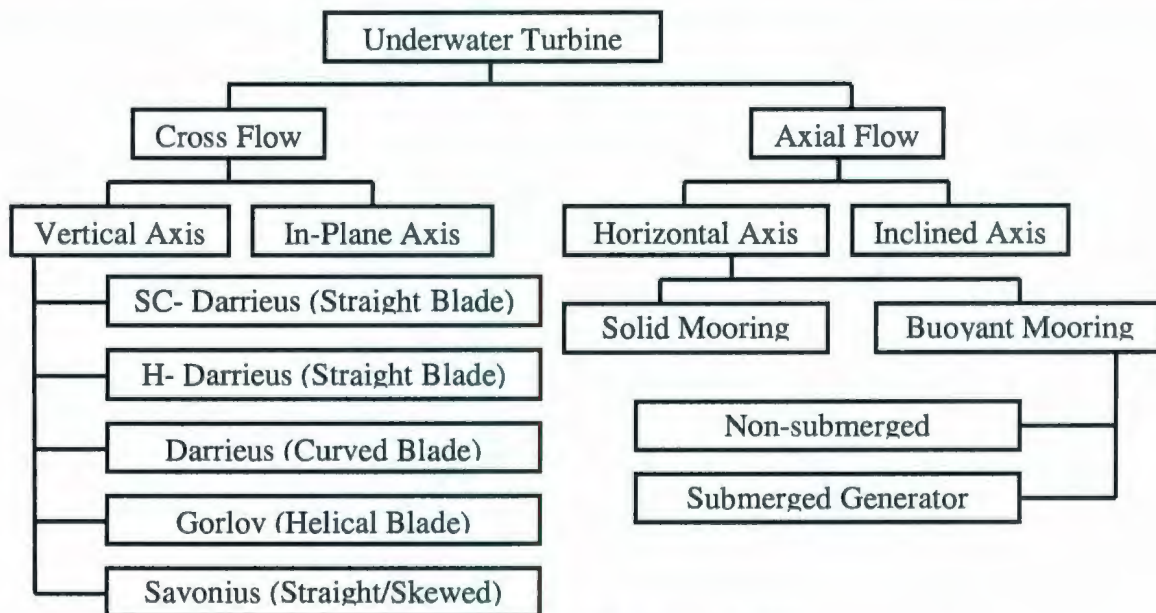


Figure 2.5 Classification of MCT

Beside these turbine types, reciprocating hydrofoils [9] are also used to harness marine current energy. The Vertical and Horizontal axis turbines are very similar to modern day wind turbines from design and structural point of view. In-plane axis turbines are better known as floating waterwheels. These are mainly drag based devices and inherently less efficient than their lift based counterparts. Inclined axis turbines have mostly been studied for small river energy converters. However, the most common vertical and horizontal axis turbines as well as reciprocating hydrofoils are explained in the next sections.

2.4.1 Vertical Axis Water Current Turbine (VAWCT)

Vertical-axis turbines (shown in figure 2.6) are a type of turbine where the main rotor shaft runs vertically. These turbines can rotate unidirectionally even with bi-directional fluid flow. Some features of the vertical axis turbine are includes the following;

- Simple in Construction
- Both Drag and Lift type.
- Fixed/Variable Pitch control
- Gearbox and generator can be at one end of the rotor axis (above the water or near to the seabed)
- Do not need yaw mechanism.
- Not always self-starting but a hybrid combination or pitch control can mitigate this problem.
- Low efficiency in comparison to horizontal axis turbines, etc.

Five major vertical axis turbines are,



(a) Savonius (b) Squirrel Cage Darrieus (c) Gorlov (d) H-Darrieus (e) Egg Beater Darrieus

Figure 2.6 Vertical Axis Water Current Turbines (VAWCT)

In the vertical axis domain, Darrieus turbines are the most prominent options. Even though examples of H-Darrieus or Squirrel Cage Darrieus (straight bladed) are rather common, instances of Darrieus turbines (curved blades) being used in hydro applications are non-existent. The Gorlov turbine is another member of the vertical axis family, where the blades are of helical structure. Savonius turbines are drag type devices, which may consist of straight or skewed blades.

2.4.1.1 VAWCTs Industrial Designs

There are several companies who develop and manufacture VAWCT for industrial applications, among them is Blue Energy. The Blue Energy turbines are manufactured with power ratings ranging from kW to MW ratings.

Established by veteran aerospace engineer Barry Davis, the Blue Energy vertical-axis turbine represents two decades of Canadian research and development. Four fixed hydrofoil blades of the turbine are connected to a rotor that drives an integrated gearbox attached to the shaft of an electrical generator. The turbine is mounted in a durable concrete marine caisson, which anchors the unit to the ocean floor, directs flow through the turbine further concentrating the resource supporting the coupler, gearbox, and

generator above it. These sit above the surface of the water and are readily accessible for maintenance and repair. The hydrofoil blades employ a hydrodynamic lift principal that causes the turbine foils to move proportionately faster than the speed of the surrounding water. Computer optimized cross-flow design ensures that the rotation of the turbine is unidirectional on both the ebb and the flow of the tide.

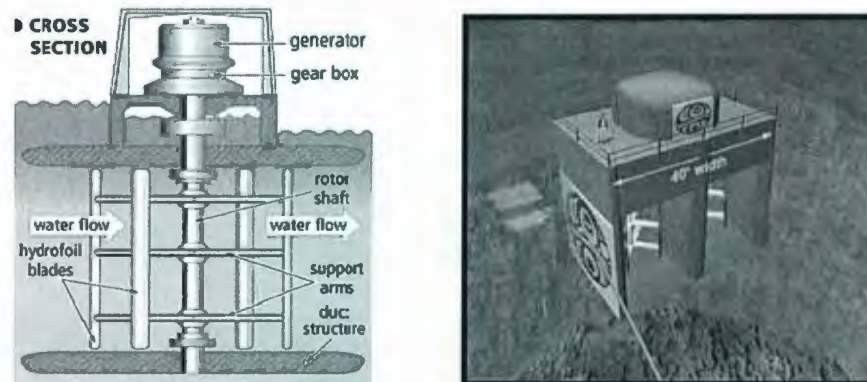


Figure 2.7 Davis Turbine [www.bluenergy.com]

The design of the Blue Energy Ocean Turbine requires no new construction methodology; it is rather structurally and mechanically straightforward. The transmission and electrical systems are similar to thousands of existing hydroelectric installations. Power transmission is by submersible kV DC cabling and safely buried in the ocean sediments with power drop points for coastal cities and connections to the continental power grid. A standardized high production design makes the system economic to build, install and maintain.

2.4.2 Horizontal Axis Water Current Turbine (HAWCT)

Horizontal-axis turbines (shown in figure 2.8) are a type of turbine where the main rotor shaft runs horizontally. These turbines generally depend on the fluid flow direction, which demands mitigation through pitching as well as yaw mechanisms. Different

mooring structure makes the distinction between HAWCTs. Turbines with solid mooring structure require the generator unit to be placed near the seabed. Horizontal axis rotors with a buoyant mooring mechanism may allow a non-submerged generator to be placed closer to the water surface.

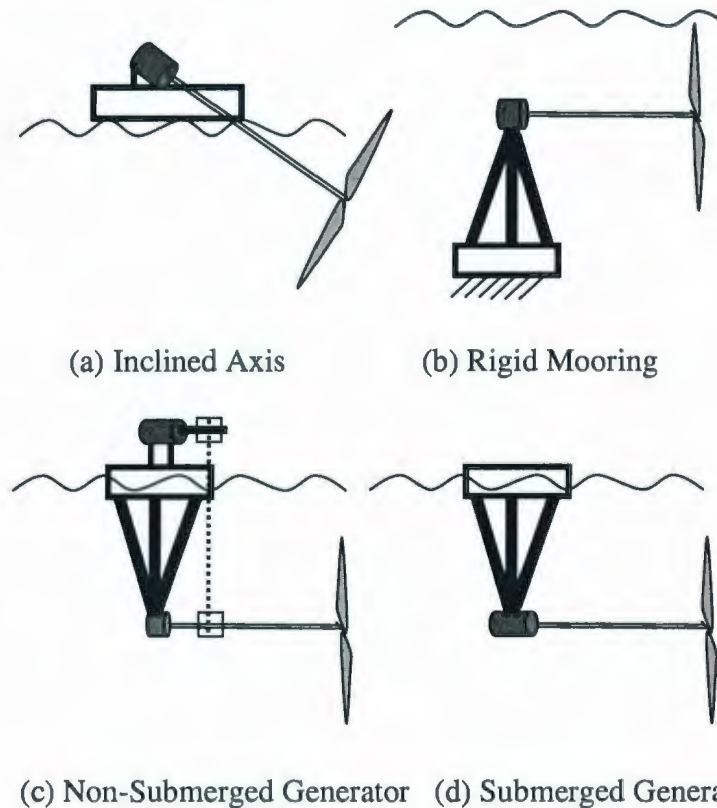


Figure 2.8 Horizontal Axis Water Current Turbines (HAWCT)

Inclined axis turbines have mostly been studied for small river energy converters.

Horizontal axis turbines have features that include;

- High efficiency, since the blades always moves perpendicularly to the water, receiving power through the whole rotation. In contrast, all vertical axis water turbines involve various types of reciprocating actions requiring airfoil surfaces to backtrack against the water for part of the cycle. Backtracking against the water leads to inherently lower efficiency.

- Gearbox and generator can be at one end of the rotor axis (above the water or submerged)
- Lift type turbine
- Fixed/Variable Pitch control
- Construction becomes complex when yaw mechanism or pitch control is introduced for multidirectional currents.

2.4.2.1 HAWCTs Industrial Designs

Among several companies, Marine Current Turbines Ltd. is one of the world leaders in the development and manufacturing of new technologies using HAWCT for exploiting tidal currents for large-scale electric power generation. Their design based on a horizontal axis turbine is also available for wind energy system applications. They can be installed in the sea at places with high tidal current velocities, or in places with fast enough continuous ocean currents, to take out copious quantities of energy from these huge volumes of flowing water. MCTs “Seaflow” is shown in figure 2.9 (Left).

The technology under development by MCT known as “SeaGen” (shown in figure 2.9, right) consists of twin axial flow rotors of 15m to 20m in diameter (the size depending on local site conditions), each driving a generator via a gearbox much like a hydro-electric turbine or a wind turbine. These turbines have a patented feature by which the rotor blades can be pitched through 180° in order to allow them to operate in bi-direction flows – that is on both the ebb and the flood tides. The twin power units of each system are mounted on wing-like extensions either side of a tubular steel monopile some 3m in

diameter and the complete wing with its power units can be raised above sea level to permit safe and reliable maintenance.



Figure 2.9 MCT's "Seaflow" (left) & Artists impression of "Seagen" (right)

2.4.3 Reciprocating Hydrofoils (RH)

Reciprocating Hydrofoils work like a fish tail and controlled by a pitch. The oscillating hydrofoil induces hydrodynamic lift and drag forces due to a pressure difference on the foil section caused by the relative motion of the tidal current over the foil section. These forces induce a resultant tangential force to the fixing arm which by driving reciprocating hydraulic rams pump, high pressure hydraulic fluid to turn a hydraulic motor and electrical generator.

2.4.3.1 RHs Industrial Designs

Engineering Business Ltd. developed the “Stingray” oscillating hydrofoil (Figure 2.10) as a developmental prototype to prove the robustness of the concept, the design and technology and the economical feasibility. As it stands the inflated development costs of this device in the current economic climate is prohibitive and has caused the project to be suspended. Lessons learned from the development and testing of the full scale 150kW prototype and have employed for a large scale second generation model to be developed and tested at a later date.

The main principal of operation as introduced above is relatively quite simple. It uses the force exerted on to it by the tidal stream to drive a hydroplane up and down, thus causing a mechanical arm supporting the plane to oscillate. This motion causes a hydraulic cylinder, attached to the main arm, to produce high pressurized oil, as it extends and retracts.

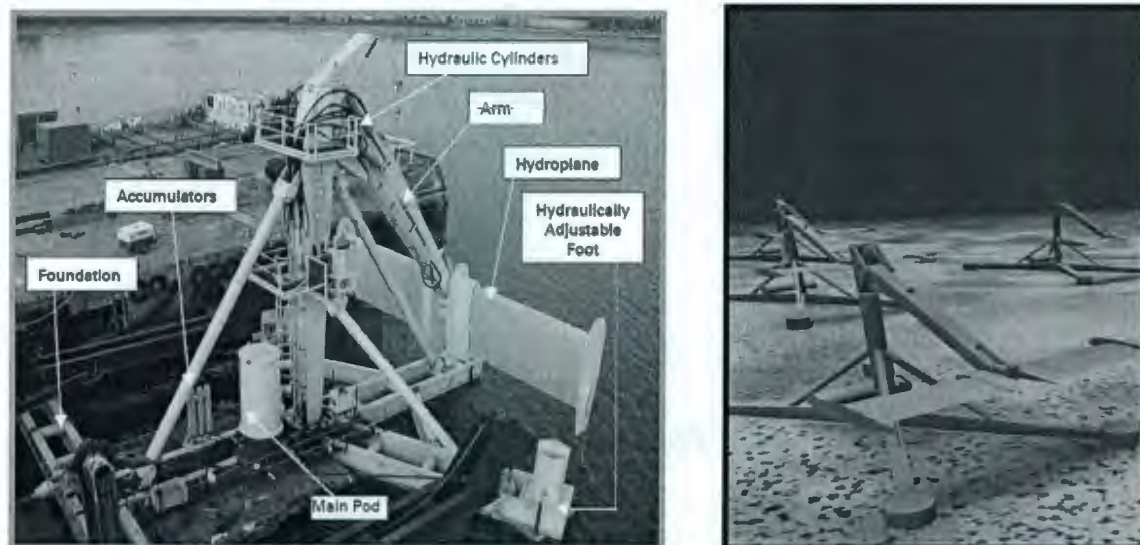


Figure 2.10 Stingray device elements (Left) and its demonstration (Right)

The pressurized oil is delivered to a hydraulic motor driving a generator and electricity is produced. The hydroplanes attack angle, relative to the approaching water stream, is controlled to maintain an optimal angle through the entire oscillation. As a result, when the current lifts the hydroplane the mechanical arm is lifted until it reaches its upper limit, then the angle of the hydroplane is reversed such that it causes a downwards drag until the motion is repeated. Thus the hydroplane is oscillated vertically in a non stopping cycle as the motion is repeated. The mechanical arm, to which the hydroplane is attached, is joined to a seabed support structure that is fixed onto the seabed using gravitation. The device is deemed suitable for a water depth down to 100 m.

2.5 Environmental impact

Marine current energy conversion are likely to be environmentally benign [10] comparing with other power generation techniques. But the majority of the proposed methods for marine current harvesting consist of modular devices that are likely to be deployed in farm arrays. So far a few environmental impact assessments have been conducted where of most of these cover short-term deployed single units. There is a general lack of proven facts on how a farm or individual deployed units would impact on fauna and benthic flora, owing to that the exact environmental effects of modular devices still needs to be fully assessed. Nevertheless some companies/organizations have progressed further than other developers and have supplied valuable information, which has been combined with knowledge from other offshore industries to permit an approximated potential environmental impact to be assessed covering the modular devices for tidal current harvesting.

From the environmental point of view, three types [11] of issues should be considered which are ecological, physical and socio-economical. Among such impacts are the following:

- Impact on fishes and marine mammals from collision with rotors
- Impact from installation, maintenance and decommission of device
- Environmental footprints from maintenance vessel on the seabed made by anchors or jack up barges
- The physical/chemical characteristics of material arising from the installation of the turbine and the effects of their deposition
- Pollution of sea with leaked substances from devices and antifouling substances on device elements
- Impact on seabed from support structure or moorings
- Impact of marine electrical cables on fauna
- Withdrawal of energy from current
- Erosion caused by scouring around the base of the support structure
- Noise emitted by some of the proposed devices

Mostly, the environmental impacts of a marine current energy conversion system are site specific. However, by prudent planning, spacing of units and improving the design, these impacts can be minimized to a local affect.

2.6 Conclusion

As a continuous and predictable resource for energy, marine currents open a wider scope to harness power from the sea. Though some existing commercial turbines are quite successful for both stand alone or grid connected system, they are mostly site specific because of the necessity in high speed of water current. Despite having some environmental impacts, marine current energy conversion is comparatively environmental friendly.

CHAPTER 3

HYBRID TURBINE DESIGN

3.0 Introduction

This chapter provides technical descriptions of both the drag type Savonius and lift type H-Darrieus turbines. Also this chapter elaborates the design process of a hybrid combination of both turbines to meet the design requirements for North Atlantic Ocean Current. The hydrodynamics associated with it is also explained. Some recommendations are included as a part of conclusive comment.

3.1 Turbine selection

The North Atlantic current profile, which was discussed in the previous chapters, can be used to select a turbine that meets the following criteria:

1. Good self-starting characteristic (or low cut-in speed), for low speed marine current.
2. High power coefficient (C_p) in order to achieve maximum output from the available power.
3. High Tip Speed Ratio (TSR) in order to avoid gearbox.
4. Good ability to produce power for different sea current (multidirectional) conditions.
5. Low environmental impact.

The first three conditions can be achieved by using horizontal or vertical axis turbine comprising a hybrid combination or pitching mechanism. On the other hand, criterion 4 facilitates making a decision about a vertical axis turbine. Though the high power coefficient can be achieved by HAWCT, a proper design of VAWCT can increase the turbine efficiency towards acceptable levels. Moreover, Vertical axis turbines operate in turbulent water patterns better than horizontal designs.

Among the VAWCT turbines, discussed in the previous chapter, Savonius and H-Darrieus types are being used for a long time for wind applications due to their simplicity in construction, technical advantages and commercial availability. Brief description and background about the Savonius and Darrieus Turbines are presented in the following sections.

3.2 Savonius Rotor

The Savonius turbine uses a rotor that was formed by cutting the Flettner cylinder into two halves along the central plane and then moving the two semi cylindrical surfaces

sideways along the cutting plane so that the cross-section resembled the letter “S”. It may be the mirror image of “S” (see in Figure 3.1). In addition, the Savonius turbine relies on stagnation principles to convert current into rotational energy. The Savonius rotor uses stagnation pressure on one side to promote rotation around a central vertical axis (as shown in Figure 3.1b). The blade turning redirects water around itself with its rounded shape so that, any tangential flow of water will produce a positive force on the rotor.

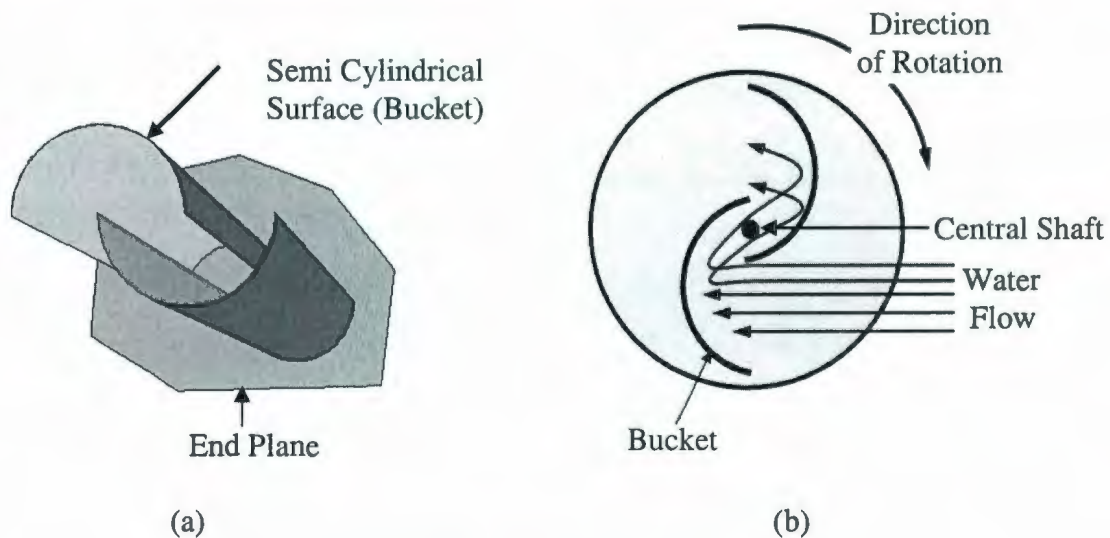


Figure 3.1 (a) Savonius View (b) Direction of Rotation

Savonius rotors [12] are used in applications; where cost or reliability is of high importance. Larger Savonius turbines have been used to generate electric power on deep-water buoys, which need small power and very little maintenance. These turbines have simple designs because, unlike horizontal-axis turbines, no pointing mechanism is required to allow for shifting water or wind direction and the turbine is self-starting.

Due to its simple and low cost construction, acceptance of water from any direction, high starting torque, low operating speed and less maintenance, Savonius rotor became popular among the design engineers and turbine manufacturers.

The Savonius design relies on the pressure of the water current against the rotor blade to create torque. As such, the Savonius design cannot exceed the speed of the water and operates at a lower angular speed ranges than would a horizontal axis or other lift type VAWCT turbines. It is worth mentioning that these turbines have the advantage of producing large torque.

If C_{Ps} is the power coefficient of a Savonius turbine then the turbine generated power (P) can be obtained from water as [12],

$$P = 0.5 \times C_{Ps} \times A_s \times \rho \times V^3 \quad (3.1)$$

Where,

P = Output power (W)

ρ = Density of water (kg/m^3)

A_s = (Height \times Diameter) = ($H_s \times D_s$), is the swept area of Savonius rotor (m^2)

V = Speed of water (m/s)

$$\text{The tip peripheral velocity of the rotor, } U = \omega_s \times R_s \quad (3.2)$$

Where, ω_s = is the angular velocity of Savonius rotor

R_s (= $D_s/2$) is the radius of the Savonius rotor

Now the Tip Speed Ratio (TSR) of a Savonius turbine is defined as

$$\text{TSR} = \lambda_s = \frac{U}{V} = \frac{\omega_s R_s}{V} \quad (3.3)$$

Turbines are usually characterized by performance curves, which give C_p as a function of λ . It is known (Betz theory) that for a horizontal axis wind turbine, the power coefficient is always inferior to the theoretical value of 0.593. In fact, the best modern machines have maximum value less than 0.45. C_p as a function of λ curves for many turbines are shown in Figure 3.2.

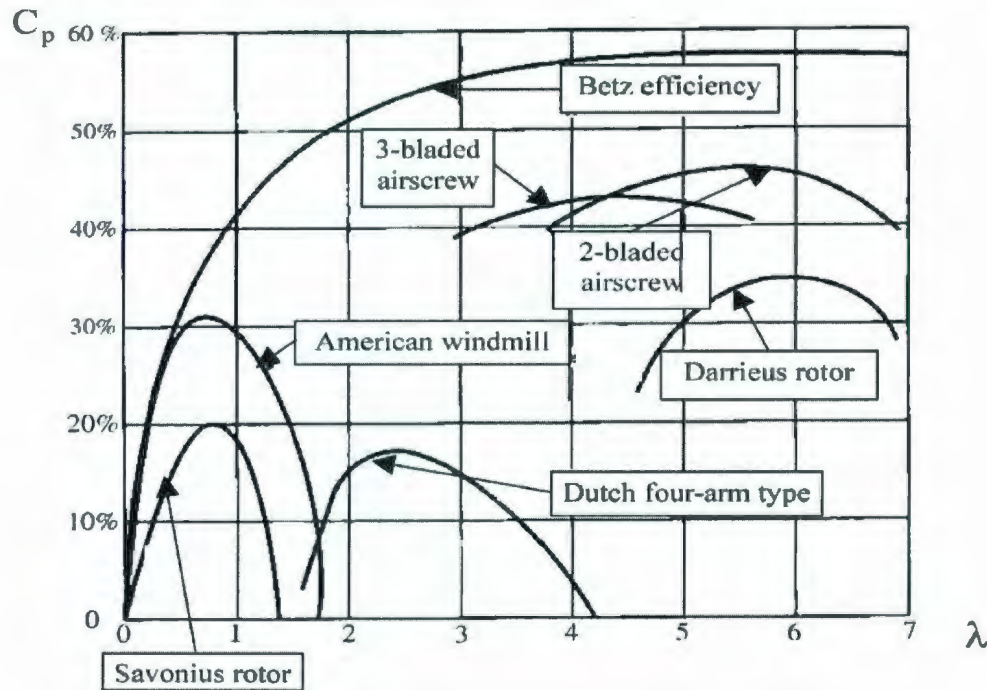


Figure 3.2 Characteristic curves of several conventional rotors (C_p vs. λ)

The aspect ratio (A_a) represents the height (H_s) of the rotor relatively to its diameter (D_s).

This is also an important criterion for the performance of the Savonius rotor:

$$A_a = \frac{H_s}{D_s} \quad (3.4)$$

In general, a value of A_a is selected larger than 1 to improve the efficiency [12].

It is known that end plates lead to better hydrodynamic performances. The influence of the diameter D_f (in figure 3.3b) of these end plates relatively to the diameter D_s of the rotor has been experimentally studied. The higher value [13] of the power coefficient is obtained for a value of D_f (shown in figure 3.3) around 10% more than D_s , irrespective of the velocity coefficient.

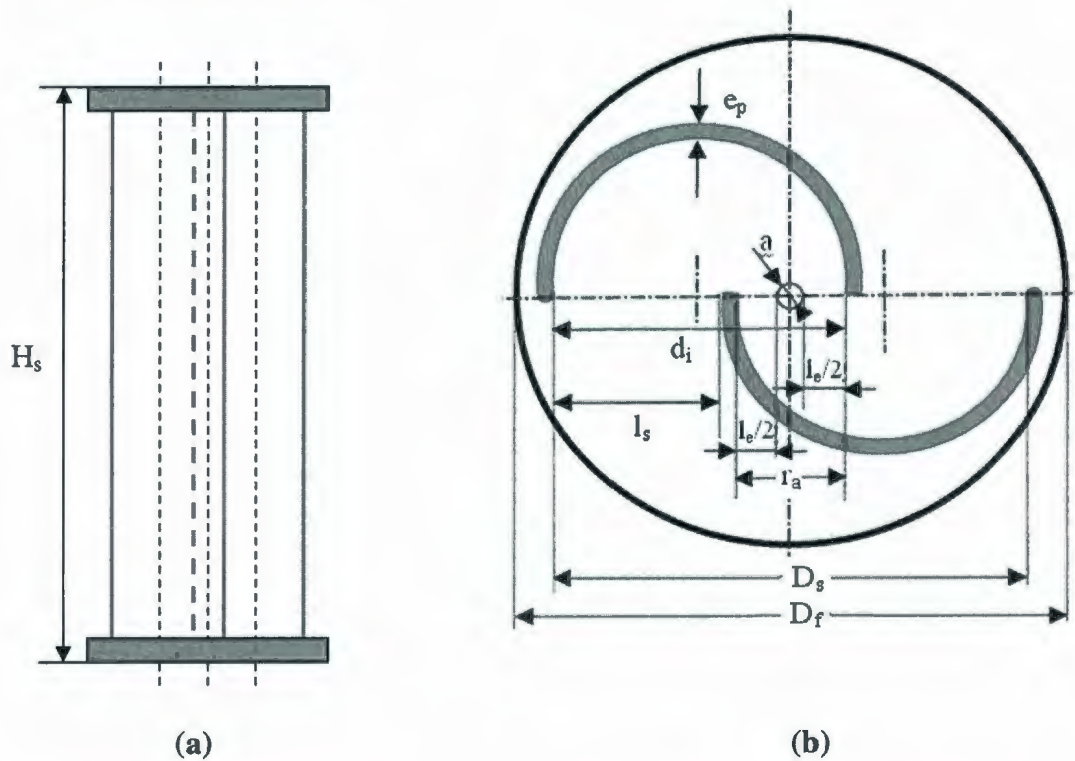


Figure 3.3 Savonius rotor: (a) Front view (single step) (b) top view (with a central shaft)

When a central shaft is chosen (see Figure 3.3b), then the overlap ratio β can be defined as [12],

$$\beta = \frac{(r_a - a)}{d_i} \quad (3.5)$$

Where, r_a is the overlap.

The best efficiencies are obtained for values of β between 20% and 30% [13].

For the two bladed Savonius turbine, starting torque would be close to zero if water direction is perpendicular to the cutting edge of the blade. Because of this reason many prefer to use the double-step Savonius rotor, where the upper and the lower paddle pairs are set at 90° to each other. The double-step rotor is found to be slightly better [13]

compared to the corresponding single-step turbine (the conventional Savonius rotor) in both torque and power characteristics. That is why, the double step Savonius turbine has been selected for the hybrid design.

3.3 H-Darrieus Rotor

The H-Darrieus configuration consists of vertical airfoils (also known as hydrofoil) mounted on a vertical shaft (See in Figure 3.4) at some distance or radius from the shaft. These machines take advantage of the lift generated by the airfoils as they move through the water or wind. Theoretically, higher rotational speed of the Darrieus turbine is an advantage for its application in generating electrical power from the energy carried in the water. In the H-Darrieus design, the airfoils used are symmetrical and have a zero pitch angle. This arrangement is equally effective regardless of the direction of the water flow. When the Darrieus rotor is spinning, the airfoils are moving forward through the water in a circular path.

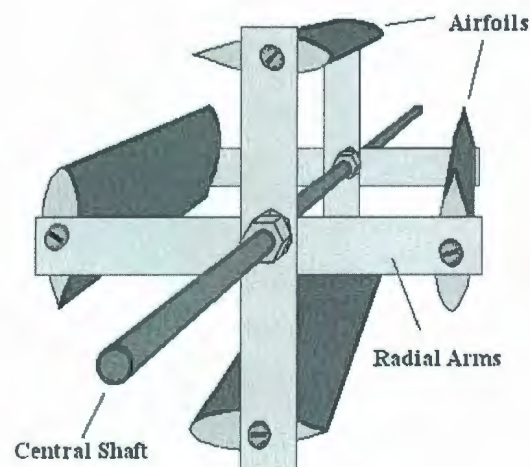


Figure 3.4 A four bladed H-Darrieus Turbine (top view)

The airfoil design and selection [14] are based on the following;

- i) Relevant design Reynolds number

- ii) Airfoil thickness, according to the amount of centrifugal stiffening and desired blade rigidity
- iii) Roughness insensitivity
- iv) Low drag (not as important for small marine current turbines)
- v) High lift root airfoil to minimize inboard solidity and enhanced starting torque

Popular symmetrical airfoil shapes for Vertical Axis Wind/Water Turbines (VAWT) are NACA-0012, NACA-0015, and NACA-0018. The primary difference between the three shapes is the chord to thickness ratio. Increasing the thickness assist airfoils to increase their lift force, but the drag also increases. These symmetrical airfoils are comparatively easy to design than a cambered airfoil.

The recorded experimental data can be used to calculate the power generated, angular velocity, Tip Speed Ratio (TSR), power available from the water, shaft power, efficiency of the turbine as well as the overall efficiency. The solidity ratio [15] and the TSR can be calculated from equations (3.6) and (3.7), respectively.

$$\text{Solidity Ratio} = \frac{\text{No. of Blades} \times \text{Airfoil Chord length}}{\text{Rotor Diameter}} \quad (3.6)$$

$$\text{Tip Speed Ratio (TSR)} = \frac{\text{Blade tip speed}}{\text{Water speed}}$$

$$\therefore \text{TSR}(\lambda_d) = \frac{\omega_d R_d}{V} \quad (3.7)$$

Where, R_d is the radius of the Darrieus rotor

ω_d is the angular velocity of the Darrieus rotor.

From the momentum model [15] for the Darrieus rotor, the power coefficient C_p for a machine with different solidity at various TSR can be determined.

The power available from water can be determined as:

$$P_w = 0.5 \times A_w \times \rho \times V^3 \quad (3.8)$$

Where, A_w is the cross sectional area under consideration

The power available at the shaft for conversion to mechanical or electrical energy can be calculated as,

$$P_{\text{shaft}} = 0.5 \times C_{Pd} \times A_d \times \rho \times V^3 \quad (3.9)$$

Where, C_{Pd} is power coefficient of the Darrieus rotor

$$A_d = (\text{Height} \times \text{Diameter}) = (H_d \times D_d), \text{ is the swept area of the Darrieus rotor (m}^2\text{)}$$

In general, stating some basic characteristics of both the Savonius and Darrieus turbines can provide the following comparison.

Table 3.1 Comparison between Savonius and H- Darrieus Turbine

VAWCT Type	Hydrodynamic	Self-Start	C_p	Keynotes
Savonius	Drag	good	Low	High Torque, Low Speed, Poor Efficiency
H-Darrieus	Lift	poor	High	Low Torque, High Speed, High Efficiency

From Table 3.1, it is evident that the drag type Savonius can be used as a drag device for a modified version of the H-Darrieus turbine with appropriate design to achieve higher starting torque at low speed water current. Details of the design process of a hybrid turbine are presented in the next section.

3.4 The Darrieus-Savonius Hybrid Turbine

During the prototype design of hybrid turbine, the Darrieus rotor will be used as a main device, while the Savonius rotor as a start-up device. They are attached permanently to

the same shaft. In order to obtain a good start-up characteristics regardless of the water direction, the Savonius rotor is divided into two (upper and lower) stages, with the two parts having a twist angle of 90° [13].

3.4.1 Possible Hybrid Configuration

There can be two possible configurations for the designing hybrid turbine as: 1) Savonius rotor can be installed inside the rotational closed space (Type A) and 2) outside the rotational closed space (Type B). These two possible designs are shown in Figure 3.5. Though the first configuration provides water interference between the rotors, the second configuration increases the height of the turbine.

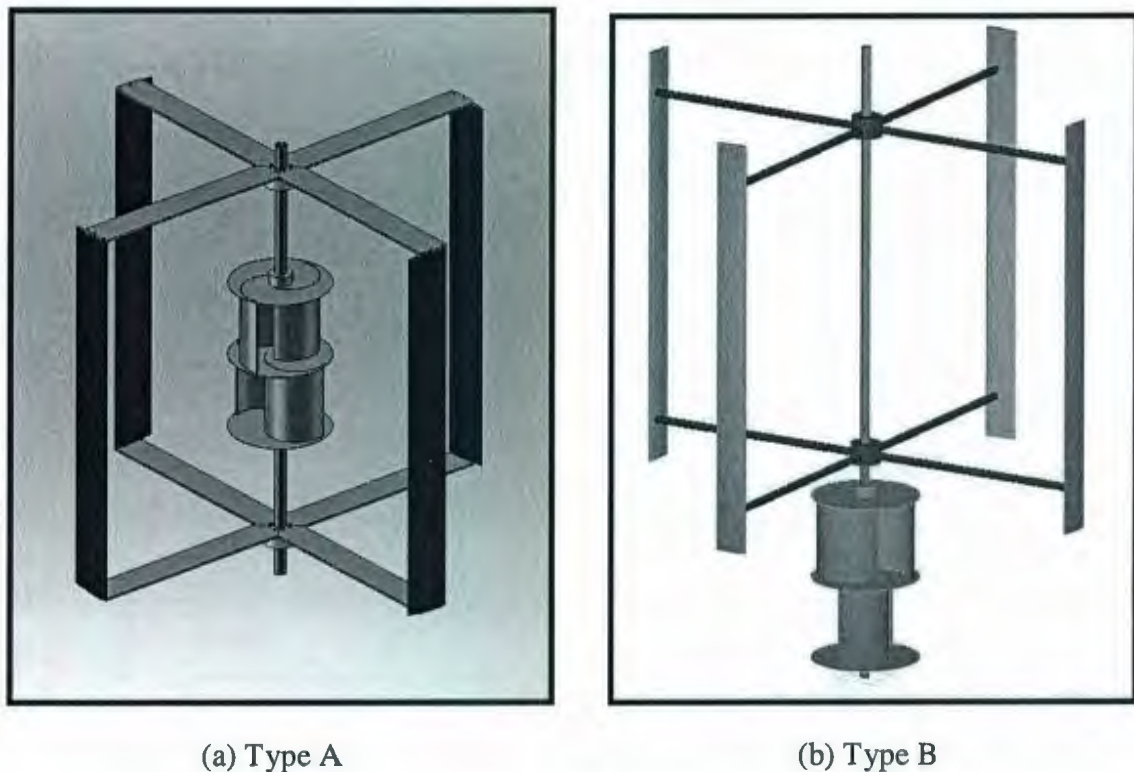


Figure 3.5 Two Possible Hybrid Configurations of Darrieus and Savonius Rotor

As reported in previous researches [16], the applications of the egg beater type Darrieus in wind turbines shows that both configurations (Types A and B) meet the requirements

with slight differences in their performance characteristics. In order to reduce the rotational axis length that can spur axial friction, rise in moment of inertia and increase the compactness, type A has been chosen as the prototype to be designed and tested for this research work.

3.4.2 Design Equations and Parameters

The power available in the water can be found using equation (3.8), which is directly proportional to the cube of the water speed. Also, the output power (P), as well as Tip Speed Ratio (TSR) of the hybrid turbine can be found using equations as:

$$P = 0.5 \times \rho \times V^3 \times (A_s \times C_{ps} + (A_d - A_s) \times C_{pd}) \quad (3.10)$$

$$\text{and, Tip Speed Ratio } (\lambda) = \frac{\omega R_d}{V} \quad (3.11)$$

Where,

A_s = Swept area by Savonius rotor in m^2

A_d = Swept area by Darrieus rotor in m^2

C_{ps} = Power coefficient of Savonius rotor

C_{pd} = Power coefficient of Darrieus rotor

ρ = Water density in Kg/m^3

ω = Shaft speed in rad/s

λ = TSR of Hybrid turbine

R_d = Maximum rotational radius (Darrieus)

By using the characteristic curve of Figure 3.2, desired values of the power coefficient for a particular TSR for both the turbines during hybrid configuration are determined as:

$$C_{ps} = 0.18 \text{ for } \lambda_s = 1 \text{ [The Savonius turbine]}$$

And, $C_{Pd} = 0.3$ for $\lambda_d = 5$ [the Darrieus turbine]

Using equations (3.3) and (3.7) for both turbines (taking same rotational speed, as they are connected by a shaft), the following can be derived,

$$\lambda_s / \lambda_d = R_s / R_d = 1/5 = 0.2$$

If, $R_s = 0.1\text{m}$, then $R_d = 0.5\text{m}$

The values for the radius ratio (R_s/R_d) of the Darrieus and Savonius turbine have a significant impact on the output characteristics of the desired hybrid turbine. This concern must be given serious consideration when designing a hybrid turbine. From previous researches [16] of wind applications, it has been found that for both turbines (using a Egg beater type Darrieus), the maximum power coefficient ratio ($C_{p_{\max_H}}/C_{p_{\max_D}}$) falls sharply when radius ratio goes beyond 0.3.

Specifications for both the turbines in their hybrid configuration are given in Table 3.2.

Table 3.2 Turbine Specifications (For Hybrid Configuration)

Savonius Rotor	
Rotor Height (H_s)	400mm
Nominal diameter of the paddles (d_i)	130mm
Diameter of the shaft (a)	20mm
Rotor diameter (D_s)	200mm
Overlap ratio (β)	0.298
Swept area (A_s)	0.08m ²
Darrieus Rotor	
Airfoil Section	NACA 0015
Number of Blades	4
Solidity Ratio [15]	0.40
Rotor diameter (D_d)	1m
Rotor Height (H_d)	1m
Swept area (A_d)	1m ²
Chord length (C)	100 mm

A snap shot of the designed hybrid structure is given below,



Figure 3.6 The designed prototype turbine (Snap Shot)

For a water speed of 1m/s, the maximum mechanical output power can be calculated using equation (3.10) as,

$$P_{\text{mech}} = 145.2 \text{ Watt}$$

Considering friction losses, actual power may be much less than 145.2 Watt.

In order to find out the shaft speed at this output, equations (3.3) and (3.7) can be used as:

$$\text{For Savonius, } 1 = (\omega_s \times 0.1) / 1$$

$$\text{For Darrieus, } 5 = (\omega_d \times 0.5) / 1$$

$$\text{So, } \omega_s = \omega_d = \omega = 10 \text{ rad/s}$$

$$\text{Therefore, } n = (60/2\pi) \times 10 = 95 \text{ rpm}$$

The Expected output power of the designed turbine using equation (3.10) is shown in figure 3.7 (Assuming ideal conversion efficiencies),

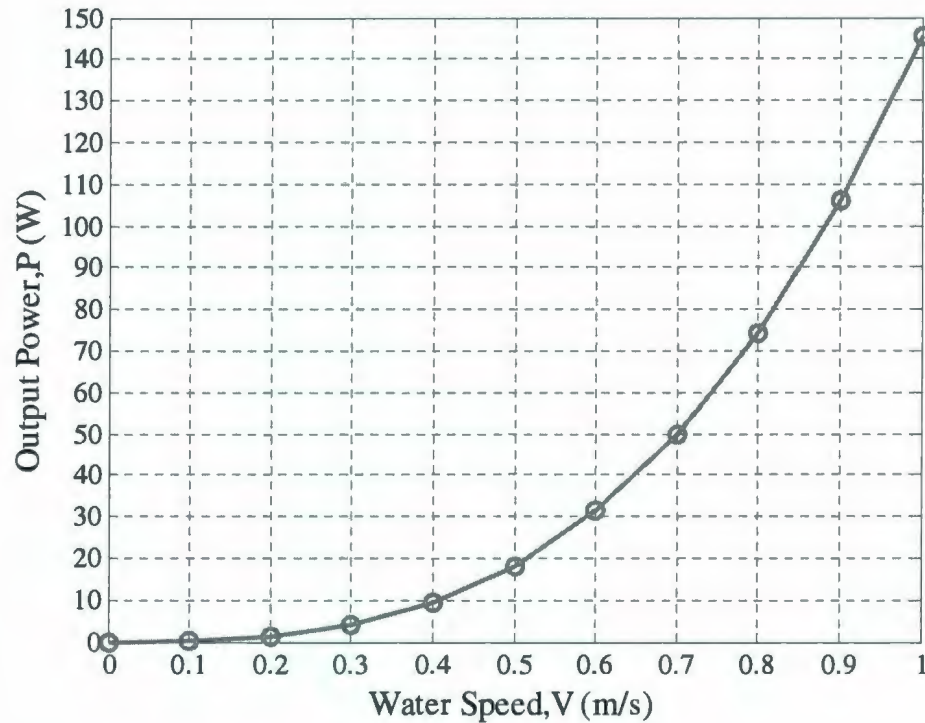


Figure 3.7 Expected output power of hybrid turbine

3.4.3 Material Selection

The choice of the material is obviously crucial. Different criteria for such selection can be the low cost, easy construction, light weight, good corrosion resistance as well as rigidity, recyclable material etc. In case of the Savonius turbine, aluminum (see Figure 3.8a) has been selected to meet the above criteria. Moreover, it requires a rugged construction as it has been designed to provide high starting torque.

The blade manufacturing and material selection is also a decisive aspect of a water turbine design, which directly affects the turbine performance. Some manufacturers are

selling airfoils, which are specially designed for test purposes. However, the above mentioned criteria are not fully consulted due to cost consideration. In this hybrid design, available airfoils in the market made with aluminum are not suitable because the total weight of the hybrid turbine increases, resulting high moment of inertia. The SEAformatics Group has cut Styrofoam (see Figure 3.8b) with a thin layer of glass fibre wrapped around the designed NACA 0015 profile. Renshape (see Figure 3.8c) pieces are added at both ends of airfoils to screw radial flat plat arms.

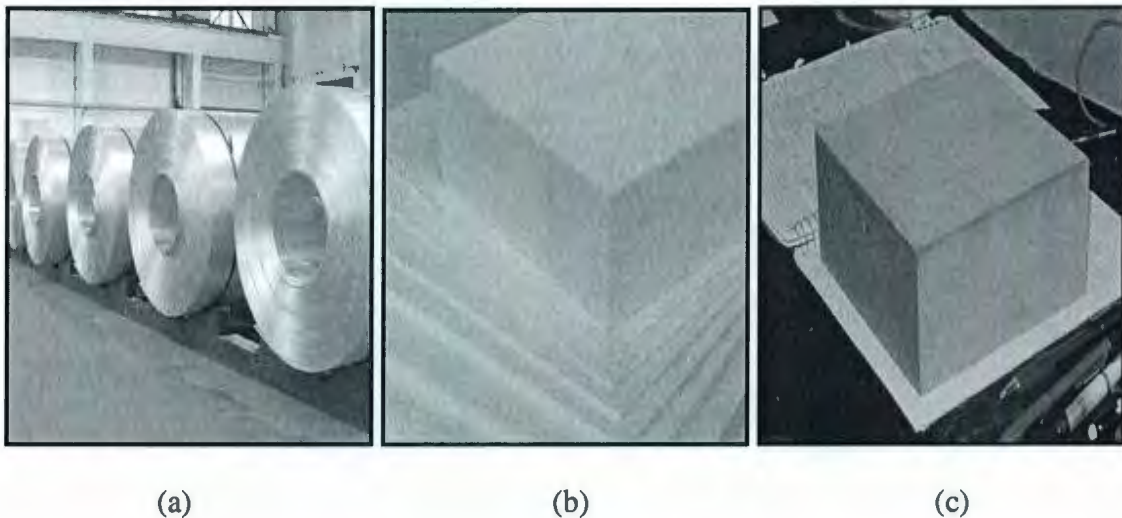


Figure 3.8 (a) Aluminum sheets (b) Styrofoam pieces and (c) piece of rensape

Miley [17] argues that the surface roughness has a generally adverse effect on the performance of airfoils. These effects become more pronounced as Re increases. In order to remove the surface roughness, scrubbing pads as well as thick paint are used.

3.5 Hydrodynamics

There are two basic forces that act on the designed turbine that are the drag and lift. The Savonius turbine provides high drag to overcome the rotor inertia and assist the hybrid turbine to start in a counter-clockwise direction. On the other hand, the Darrieus turbine is powered by the phenomenon of lift force. This lift force is created because of the airfoil shape of the turbine blades. These blades cut through the water with an angle of attack to the water causing a pressure differential. The resulting pressure differentials cause a force called lift, which propels the blade forward. In order to propel the turbine, the net torque caused by lift forces must be greater than the net torque caused by drag forces.

Drag force can be found as:

$$D_f = 0.5 \times C_D \times \rho \times A \times V^2 \quad (3.12)$$

And, the lift force can be found as:

$$L_f = 0.5 \times C_L \times \rho \times A \times V^2 \quad (3.13)$$

Where, C_D = Drag Coefficient (0.045 for an Airfoil, but it varies)

C_L = Lift Coefficient

A = Airfoil/ Frontal Area

Drag force depends on the Reynolds Number, which is defined as:

$$R_e = V \times L \left(\frac{\rho}{\mu} \right) \quad (3.14)$$

Where,

R_e = Reynolds number, which is dimensionless (It is a ratio of two quantities with the same unit (dynamic pressure/shearing stress)).

μ = Dynamic viscosity

V = Velocity of the Water in m/s.

L = Characteristic length, in this case the largest cross section of the frontal area in meter.

The forces driving the designed hybrid turbine can be described in more detail with the assistance of Figure 3.9. There are two important velocity components. The first one is the velocity of the airfoil relative to the shaft, which is at all times parallel to the chord, having a magnitude equal to the rotational speed (ω) multiplied by the radius (R). The second one is the velocity of the water (V), which is approximated as a constant velocity in one direction (it is upside down). The resultant of these two velocities is the effective velocity of the water relative to the airfoil. The angle between this resultant velocity and the chord of the airfoil is called the angle of attack (α).

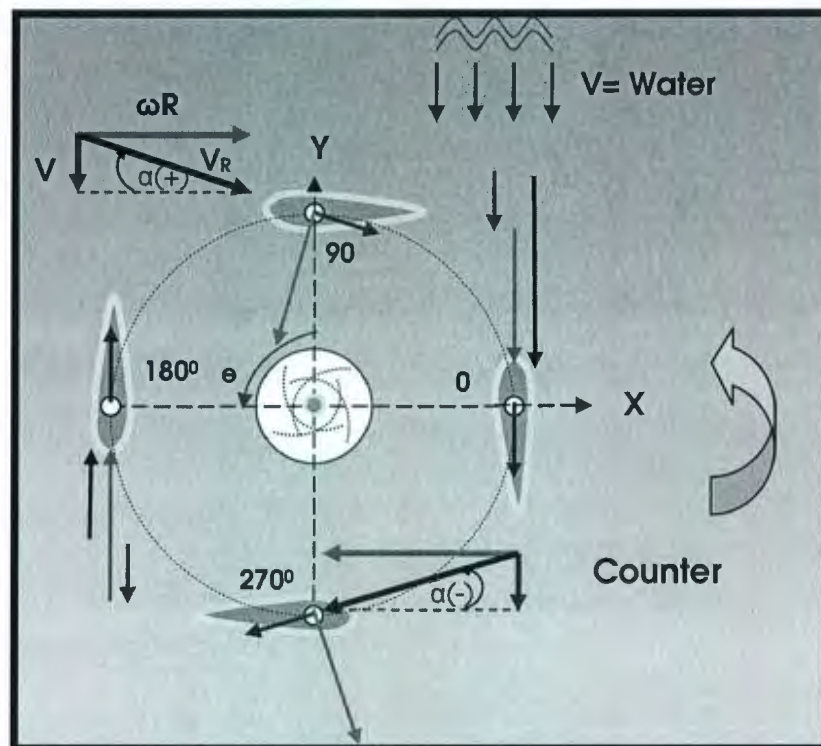


Figure 3.9 Hydrodynamics of the hybrid turbine

The Lift is created by a pressure differential, which is perpendicular to the drag force and whenever there is an angle of attack (α) not equal to zero. In 0° and 180° position of θ (Azimutal or orbital blade position shown in Figure. 3.9), the angle of attack (α) is 0° . At this point, only a drag force exists. The lift begins to be created as the blades rotate out of these two positions and α increase. This lift is perpendicular to the resultant water direction (or drag created at $\frac{1}{4}$ th of chord length) but, most importantly, it always introduces counter-clockwise rotation for this designed structure regardless the direction of water flow.

The resultant water speed can be found as [18]:

$$V_R = V\sqrt{1 + 2\lambda \cos \theta + \lambda^2} \quad (3.15)$$

And the angle of attack (α) or incidence angle can be found as:

$$\alpha = \tan^{-1}\left(\frac{\sin \theta}{\cos \theta + \lambda}\right) \quad (3.16)$$

Where, λ represents TSR for the designed hybrid turbine.

3.6 Conclusion

The design process of a hybrid turbine needs a proper combination and sizing of both the turbines. Solidity ratio of the Darrieus rotor as well as radius ratio of the turbines also has a great impact on the hybrid turbine design. The material selection, incase of the Darrieus hydrofoils, were according to the flexibility needed to cut a symmetrical NACA shape for prototype design in the workshop. Furthermore, during the application phase, the materials are selected to provide a rigid structure by keeping the weight to a minimum tolerance label so as to reduce the starting moment of inertia. Possible materials are fiber

glass, PVC (third most widely used thermoplastic polymer after polyethylene and polypropylene) etc. As emphasized, surface roughness should be taken into account during this material selection.

CHAPTER 4

EXPERIMENTAL SETUP AND TEST RESULTS

4.0 Introduction

This chapter introduces the turbine experimental test environment in the Flume tank. Several experimental tests are conducted using sensors and Data Acquisition (DAQ) systems. In order to perceive the experimental stages, some snap shots are provided. The experimental test results are presented and discussed in this chapter.

4.1 Experimental Setup

The designed hybrid turbine has been built and tested in the flume tank located at the Marine Institute of Memorial University of Newfoundland, Canada. The Flume Tank dimension is 8m wide, 4m deep and 22.25m long. Flume tank contains 1.7 million liters of water when full and is divided horizontally into 2 sections. The lower section allows water to circulate. The upper test section holds the gear and allows observation from above and from the side. Three pumps or impellers located in the return section circulate the water around the tank. Each impeller or pump is driven by a 125 HP DC motor. It is worth mentioning that the Flume Tank is the largest in the world of its type. Moreover, it is able to provide a water velocity up to 1 m/s. Figure 4.1 shows the Flume Tank as well as the immersed hybrid turbine.



Figure 4.1 Flume Tank (Left), Immersed Hybrid Turbine (Right)

The torque data are collected using a load cell (Model: LCKD-5, Omegadyne) of 0-5lbs and a torque arm of 15cm long. A Magnetic particle brake (Model: B115-H, Placid Industries) with a coil voltage of 12 volt and torque range 2.5-115 lb.-in., is used for force data measurement. Also, a gear-tooth sensor (Model: Cherry GS100102) has been used for speed measurement. Furthermore, sensors are calibrated to give mass in gram and speed in RPM. These arrangements are shown in Figure 4.2.

All sensors are setup above the water level with the extended shaft. Clamps are used to hold aluminum made frame with the base to avoid vibration and provide testing flexibility.

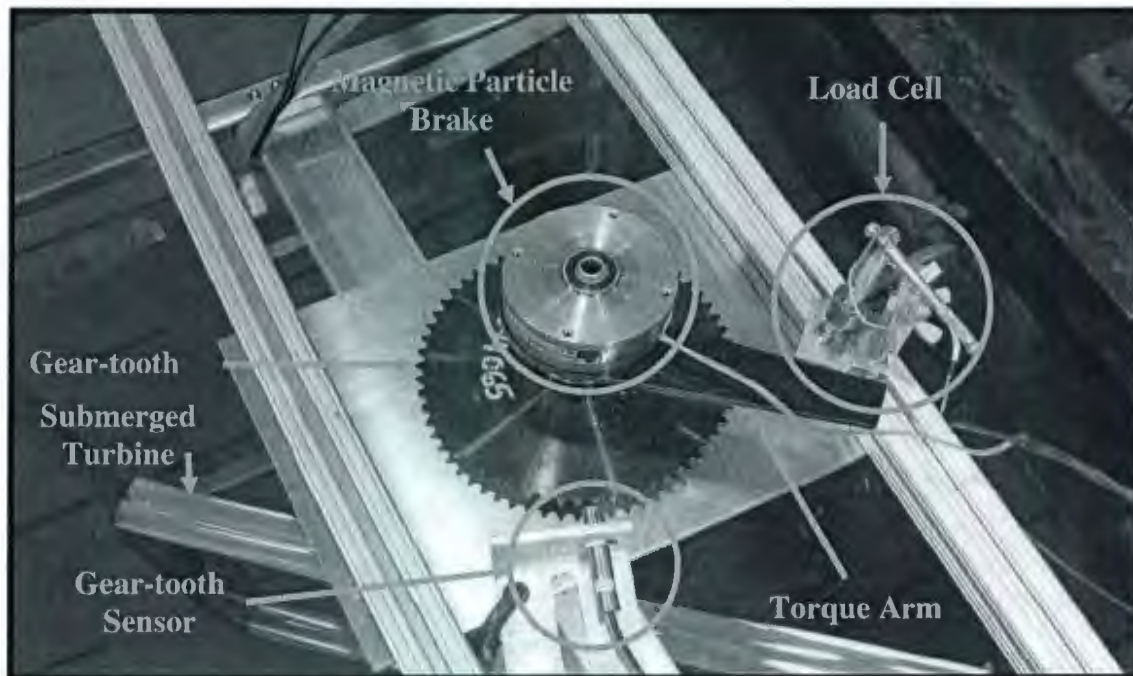


Figure 4.2 Torque and speed data collection

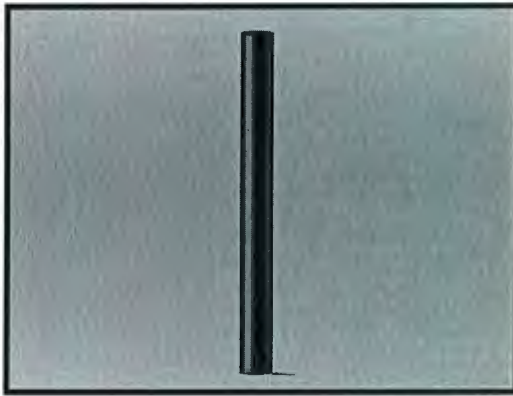
A Data Acquisition System (DAQ) board comprising a board model of OMB-DAQBOARD-3000 is used for data collection, which is connected to a laptop to store data using DaqView software. This arrangement is shown in Figure 4.3.



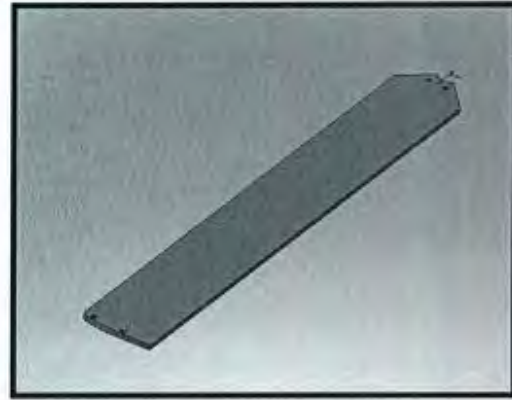
Figure 4.3 DAQ Board and Data Collection Terminal

4.1.1 Associated parts

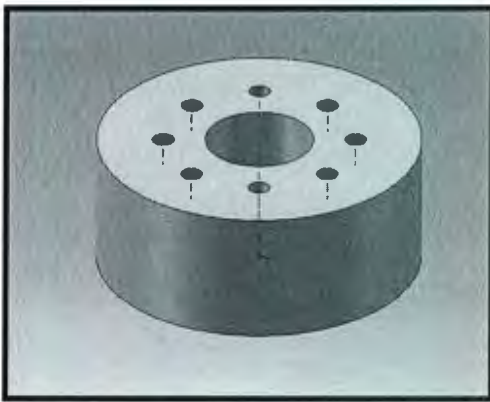
A 20 mm (diameter) of circular rod, made of aluminum is used as a central shaft. As the turbine total height is 1.4 meter, the central shaft is 2m long to facilitate testing process at Flume Tank, using the designed frame. Eight flat braces, (made of Aluminum) with a dimension of 500mm (0.5m) long, 69.34mm wide and 6.35mm height are used as radial arms to provide minimum drag while maintained a rugged structure. Two hubs with an outer diameter of 76.2mm and a height of 38.1mm are used to connect radial arms with the shaft. Bearing housing is prepared using a hub type aluminum made structure including same outer diameter. All these are shown in Figure 4.4.



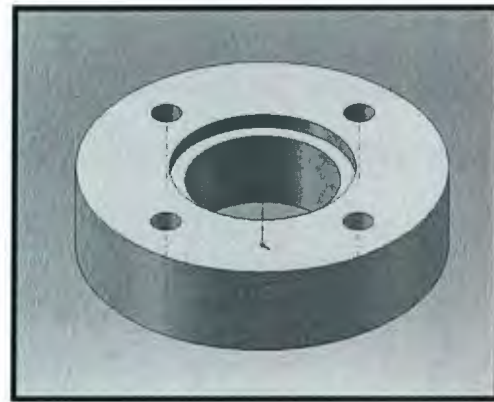
(a) Central Shaft



(b) Flat Brace (Radial Arm)



(c) Hub



(d) Bearing Housing

Figure 4.4 Associated parts (CAD View, SolidWorks)

4.2 Test Results

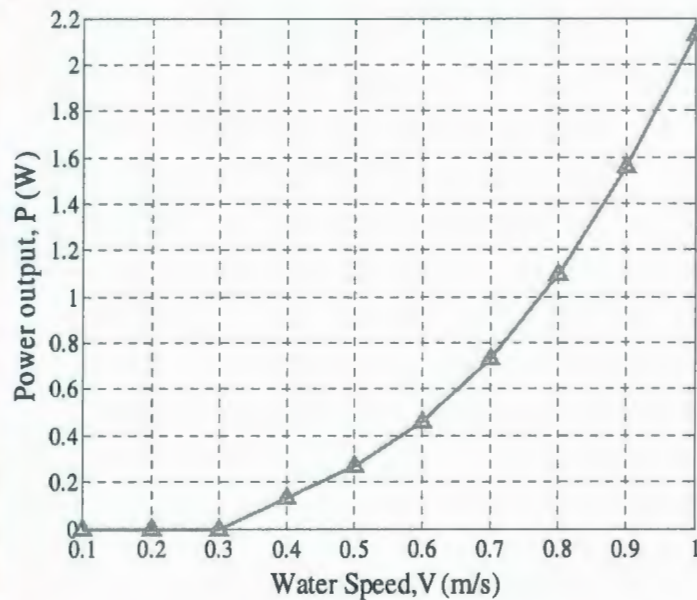
The experimental testing is conducted in three stages. In the first stage, the Savonius and Darrieus turbine are tested individually and then the hybrid turbine is tested. Before discussing the hybrid test data, test results of Savonius and Darrieus turbine are discussed. MATLAB (Version 7.4.0.287) has been used for data processing (see Appendix A and Appendix B).

4.2.1 Savonius turbine test results

The designed two step savonius (shown in Figure 4.5a) is tested at the same environment discussed before. Water speed is varied from 0.1m/s to 1 m/s and the mechanical power is measured using the sensors discussed before. The power achieved through this measurement is shown in Figure 4.5b.



(a)



(b)

Figure 4.5 (a) Double step Savonius turbine (b) Experimental power output

The power curve provides a cut-in speed performance of the Savonius turbine below 0.4 m/s where it provides around 2.13 watt at the design speed of 1m/s. As explained previously, its TSR is always less than 1.

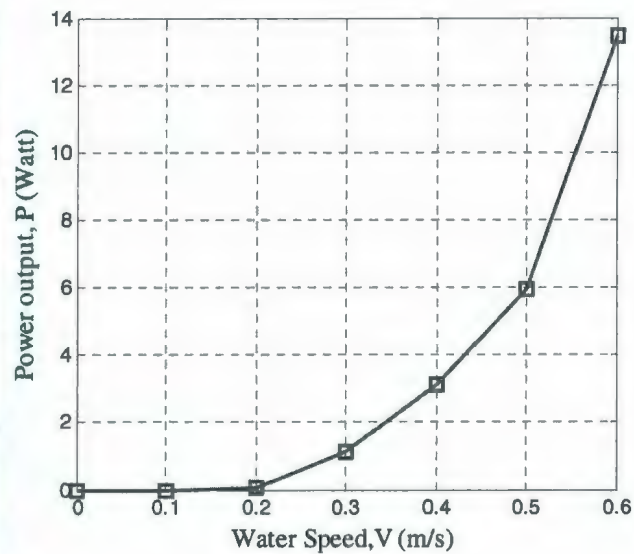
4.2.2 Darrieus turbine test results

Similar to the Savonius turbine, the Darrieus turbine is tested individually but it is not possible to test the turbine beyond 0.6 m/s of water flow due to the light structural

strength of the foam in airfoils. Excessive drag from the water cause bending of the foils and it become effective after 0.6m/s of water flow.



(a)



(b)

Figure 4.6 The H-Darrieus turbine (a) 4-bladed prototype (b) power output

Figure 4.6b demonstrates that the Darrieus turbine started to provide power at 0.3 m/s water speed. Also, it shows that as the flow is increased, the power generation increases to reach at around 13.5 Watt when water speed became 0.6 m/s. As the Darrieus turbine test is done before the hybrid turbine, water speed is limited to 0.6m/s to avoid airfoil damage.

Figure 4.7 shows the C_p vs. TSR (λ) for the H-Darrieus turbine. From C_p vs. TSR, it is assured that the maximum power coefficient of 0.1248 has been achieved at 0.6 m/s. At this point, the TSR found is around 2.67. Though the maximum TSR of 3.09 is found at 0.4m/s, the power coefficient is very low (0.012) during this time. In addition, a closer

investigation proves that the C_p vs. λ curves are almost same in pattern and very close to each other.

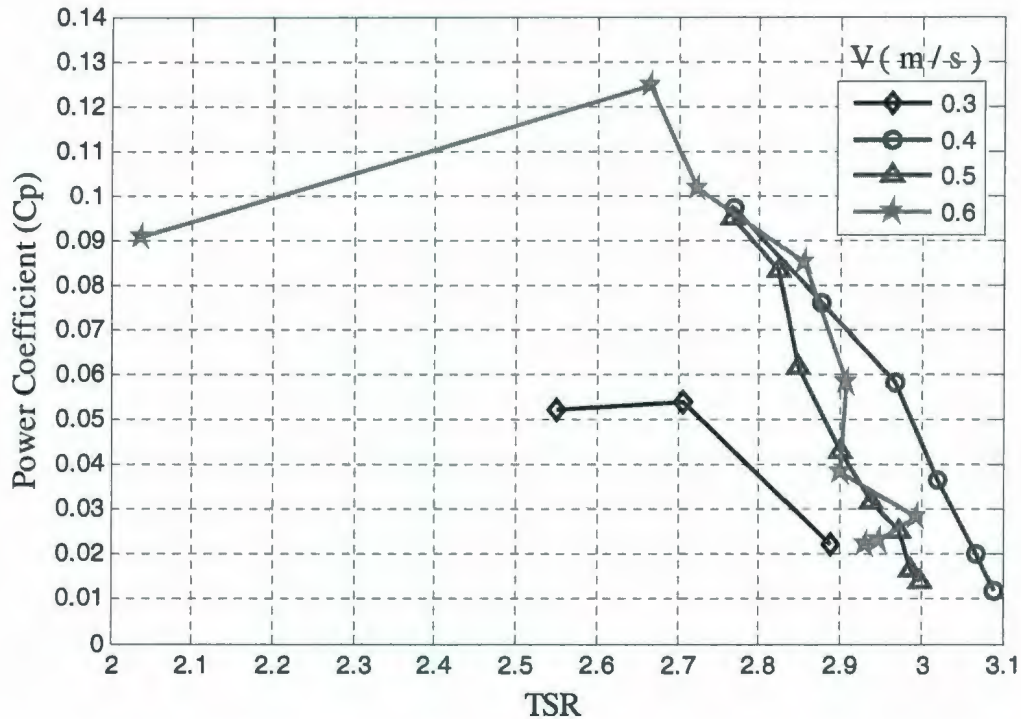


Figure 4.7 C_{pd} vs. TSR (λ) for H- Darrieus Turbine

The next sections explain the Darrieus turbine with its hybrid configuration in details.

4.2.3 Hybrid turbine experimental test results

As previously observed, it is imperative to mention that the force limitation (0-0.51b) in load cell arrangement limits the data point collection. Furthermore, the hybrid turbine is tested up to 0.8m/s of water flow to avoid blade damage, as it feels the same type of drag after 0.5 m /s.

4.2.3.1 Electrical generated power with water speed

The figure 4.8 demonstrates the electrical generated power as the function of the water speed for all three vertical axis turbines. Though the power generated by the Savonius turbine has been discussed earlier, the main comparison between the H-Darrieus turbine with its hybrid configuration are of major focus. In order to demonstrate the electrical generated power output using the proposed hybrid turbine with its H-darrieus structure, one arbitrary data point (at 0.7m/s with power of 19 Watt) of H-Darrieus turbine is used depending on the previous data points. As discussed earlier, the Darrieus turbine starts its power generation at 0.3 m/s (known as cut-in speed) and it is able to produce maximum power of 13.5 Watt at 0.6 m/s. In case of the proposed hybrid turbine, it is quite evident from Figure 4.8 that its power generation of 0.73 watt starts at 0.2 m/s.

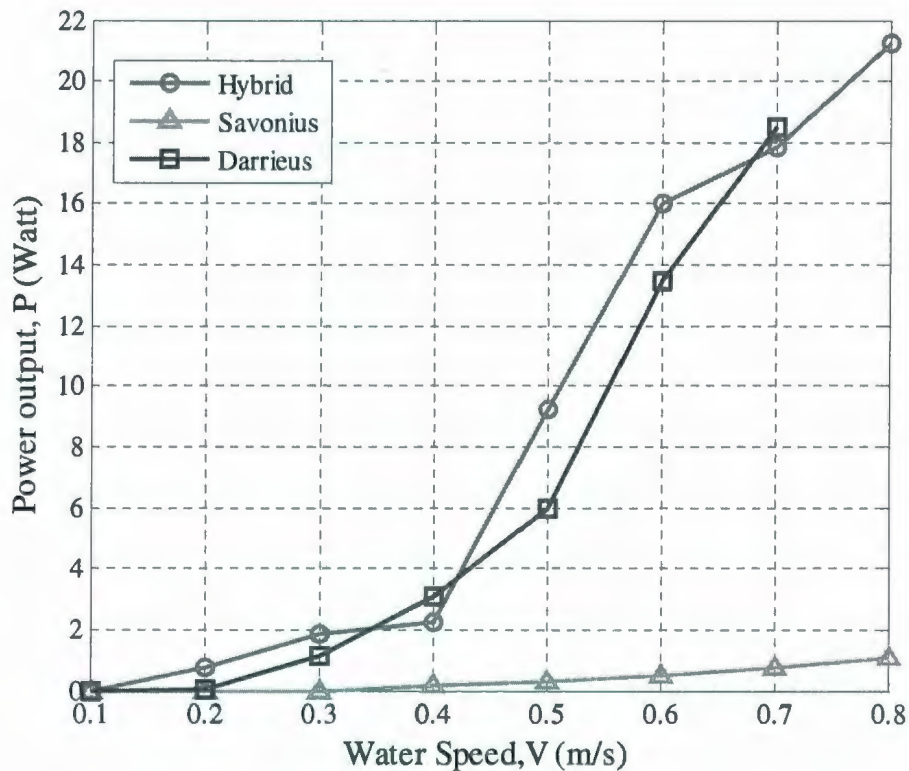


Figure 4.8 Power plots for the Savonius, Darrieus and hybrid turbine

In other words, Savonius turbine has improved the initial torque produced by the Darrieus turbine and strengthened the self-starting characteristic of its hybrid structure. Moreover, the electric power generation of designed prototype has led the Darrieus turbine throughout the test frame except over 0.35m/s to 0.42m/s water speed range, where the drag device became dominant and reduced the electrical power generation. As the speed goes up, the hybrid turbine lift becomes dominant. It should be mentioned that, the difference in electrical power generation becomes lower as the water speed goes high and reduce the contribution of the start-up device. This phenomenon is also demonstrated using the extended data point of the Darrieus structure. A crossover point is also shown between 0.6 to 0.7 m/s, where the maximum power achieved with the hybrid configuration at 0.8 m/s is approximately 21.3 Watt.

A closer investigation also indicates that the hybrid turbine made transition between drag to lift type turbine as the water speed increases from 0.2 m/s. Later test results (C_p vs. λ) provide the evidence in this issue.

4.2.3.2 Electrical generated power with turbine speed

Figure 4.9 shows that the power generated for different turbine speeds (ω) of hybrid turbine. Maximum speed achieved is around 4.4 rad/s for 0.8 m/s. It is quite evident that for each water flow, the turbine angular motion goes to a higher value and it produces a lower torque and ultimately ends up with low power generation. At 0.3m/s and 0.4m/s water speed, the turbine is stopped before applying the maximum available torque and it is not true for other flow rates (0.5m/s-0.8m/s). As the flow speed increases, both the power (P) as well as turbine speed (ω) increase.

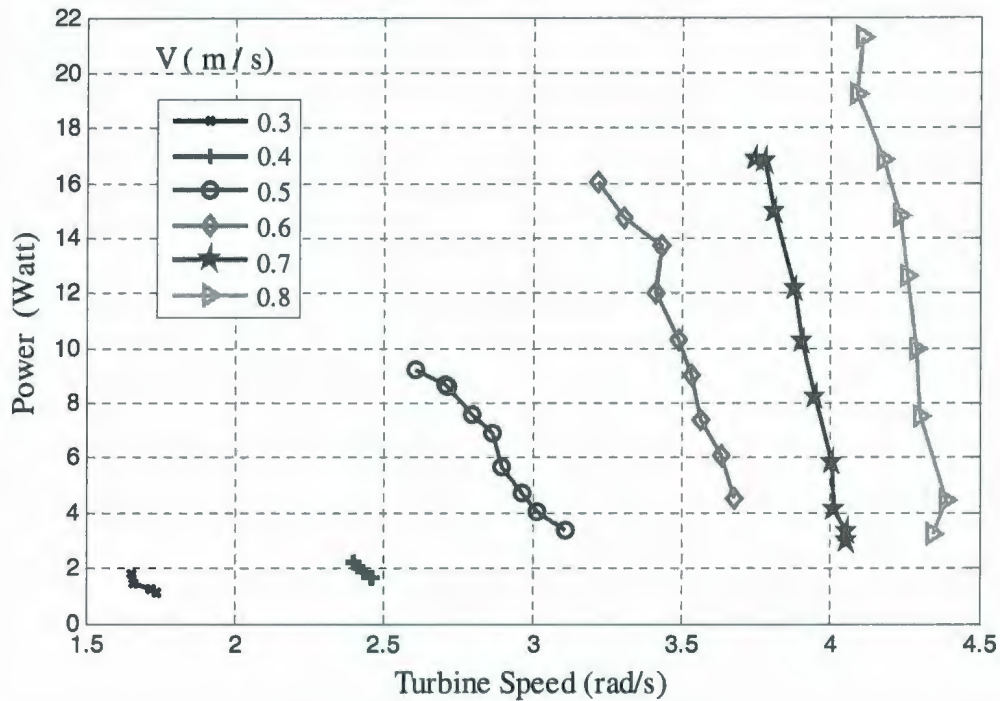


Figure 4.9 P vs. ω (Hybrid Turbine)

A TSR higher than 1.5 at 0.3m/s indicates that, the turbine to be lift type after its cut-in speed. Over the speed 0.2 and 0.3 m/s, the transition from a drag to a lift type turbine can be observed.

4.2.3.3 Power Coefficient (C_p) with Tip Speed Ratio (λ)

Figure 4.10 illustrates one of the important characteristics of the proposed hybrid turbine. It demonstrates the power coefficient with tip speed ratio for different water flow rate. The maximum conversion efficiency is found at 0.6m/s, which is about 15%. At this point, the TSR is found to be 2.7. Though, the maximum TSR of 3.1 achieved at 0.5 m/s, the conversion efficiency at that point is comparatively low.

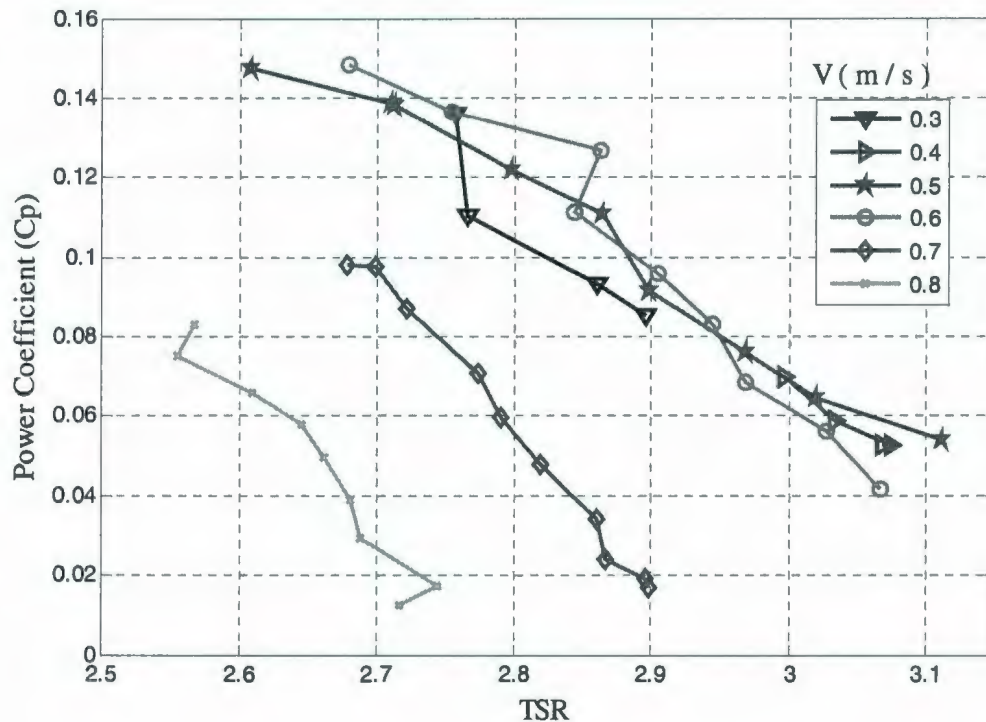


Figure 4.10 C_p vs. TSR (λ) for Hybrid Turbine

Comparing with the Darrieus type alone, the maximum conversion efficiency is found at 0.6 m/s during both cases. However, an increase in efficiency of about 2.5 % (12.48% to 14.84 %) is really a good indicator for the overall performance of hybrid turbine for such place when marine currents are not beyond 0.6 m/s. It is also to be noticed that the C_p vs. λ curves, for 0.3m/s to 0.6 m/s water flow, follow almost similar pattern and are close to each other. On the other hand, the airfoil bending has introduced obstacles for which the curves achieved for 0.7m/s-0.8m/s water speed, ended up with a different and low C_p as well as different TSR.

It should be noted that the turbine efficiency is higher between the TSR of 2.6 to 2.8, where, turbine power should be extracted in this region to get higher conversion efficiency.

4.3 Conclusion

In spite of having practical limitations during the experimental tests, the designed turbine has met the major criteria except the efficiency achieved. Further improvement in efficiency can be using higher solidity ratio [19] but it should be limited to avoid the increase in moment of inertia. A cambered airfoil of NACA 4412 [19] can be tested to get more torque at low TSR. The added point did not make any difference to discuss the design objective rather assisted to understand the principal of operation. The Savonius turbine without a central shaft may increase the cut-in speed of the hybrid turbine. Also, proper combination of the magnetic particle brake and load cell is extremely important to achieve smoother characteristics during experimental tests. The hydrofoils can be manufactured with the suggested material (fiber glass or PVC), for better structural strength. Finally, turbine power should be extracted during low TSR (2.6 to 2.8) to make it more efficient and it should be placed where the current speed varies from 0.2 to 0.6m/s and provides an average speed of at least 0.4m/s throughout a year.

CHAPTER 5

MARINE CURRENT ENERGY CONVERSION SYSTEM (MCECS)

5.0 Introduction

This chapter presents the structure and design of a Marine Current Energy Conversion System (MCECS). The main components of MCECS are discussed along with some theoretical analysis of the dc-dc converter. The designed converter circuit is explained with its test results as well as practical considerations for its operation.

5.1 Marine Current Energy Conversion System (MCECS)

Electrical Energy Conversion Systems are integrated systems, which can be composed of power electronic converters, electrical machines, actuators, energy storage devices, and control systems. The adoption of electrical energy conversion systems is being driven by the need to increase energy efficiency and controllability, while reducing system weight, maintenance and overall costs.

A marine current energy conversion system may consist of a turbine, a generator, a gearbox, a signal conditioning circuits (power electronic converters), an energy storage system etc. A block representation of MCECS is shown in Figure 5.1.

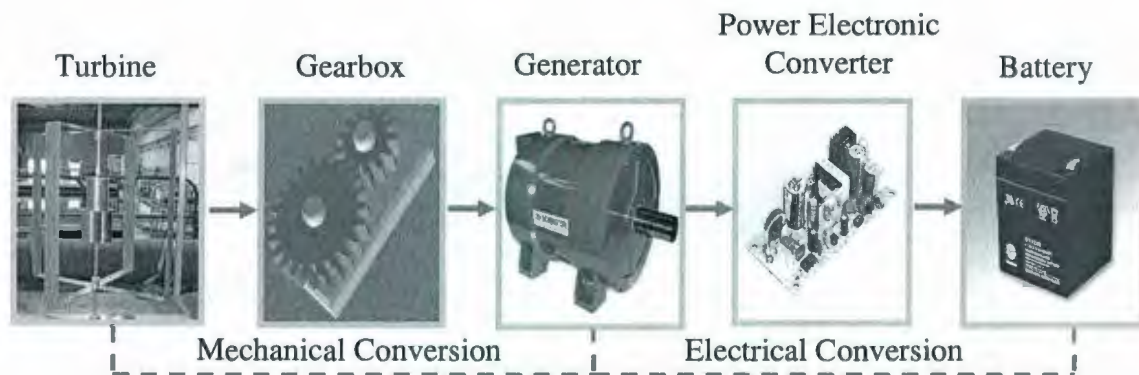


Figure 5.1 Marine Current Energy Conversion System

As the turbine design discussed in chapter 4, electrical conversion systems is to be discussed in the sections of this chapter. Furthermore, due to practical considerations, this chapter rationalizes avoiding the gearbox.

5.2 Generator Selection for MCT

The generator provides a means of energy conversion from the mechanical torque of the water turbine, as prime mover, to the electrical voltage and current. The mechanical connection to the turbine rotor is through the main shaft. The connection may be a direct drive or through a gearbox. However, small scale marine current power applications require a cost effective and mechanically simple generator. The use of direct driven generators, instead of geared ones, reduces the number of drive components, which offers the opportunity to reduce costs and increase system reliability and efficiency.

Moreover, a typical water current turbine rotates below 100 rpm, which makes a direct drive permanent magnet generator (PMG) the best option [20]. PMGs can be advantageous due to their self excitation, high efficiency, high power factor, high reliability and low maintenance cost.

5.2.1 Permanent Magnet Generator

A permanent magnet is classified as a “hard” magnetic material in which the domain orientation is permanently fixed by an applied magnetizing force. In a permanent magnet generator, excitation is supplied by a permanent magnet, rather than a typical DC source. This is the main difference between a PMG and other generators; it consists of a stator with armature winding and a rotor mounted with permanent magnets to provide the field flux. In general, the use of permanent magnet excitation provides the generator designer with a greater degree of freedom in physical configuration than with most other classes of rotating electric machines. There are several physical configurations of the PMG, two of the most common configurations being the Radial Flux PMG and Axial Flux PMG, as seen in Figure 5.2.

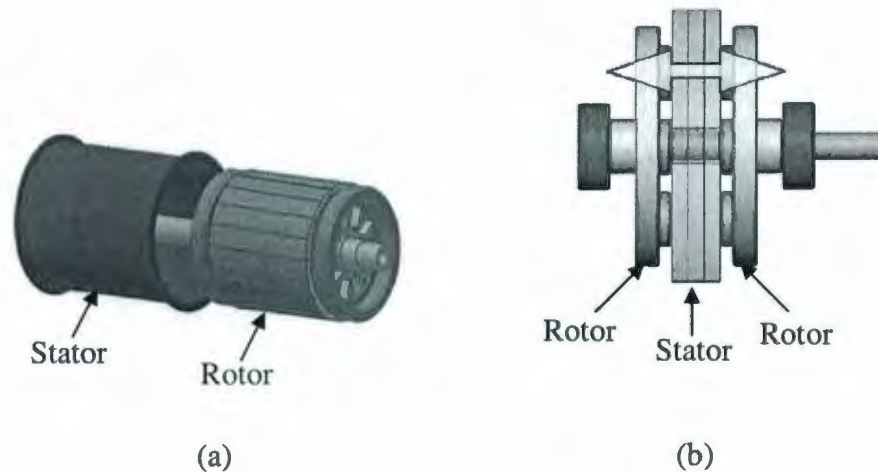


Figure 5.2 (a) Radial Flux and (b) Axial Flux PMG

For low power applications at low speeds of rotation the axial flux permanent magnet generator is particularly well suited [21-24]. The selection of this type of PMGs is based on the ability to design it with large pole number and high strength permanent magnets.

Axial Flux Permanent Magnet Generators (AFPM) have an air-gap surface perpendicular to the rotating axis and the air-gap generates magnetic fluxes parallel to the axis. The rotor is in the form of a disc attached to a permanent magnet (Nd-Fe-B). The generator has two rotors on each side of the stator (See Figure 5.2(b)). In addition, depending on the orientation of magnetization, the rotor can be classified into two types: the radially-oriented type and the circumferential type [21]. The advantages of AFPM generator is that it has efficient cooling, high power density, and can be manufactured in slim styles. The number of permanent magnets can be increased by two rotors on each side of the stator windings. Therefore, the two sides of the conductor can be used concurrently in the designing of high-efficiency PMGs. The two disc-type rotors with permanent magnets also operate as fans to ease the exhaustion of heat generated by the stator windings.

5.2.3 Cogging Torque

Two undesired pulsating torque components in Permanent Magnet (PM) machines affect the machine performance [25]. One is ripple torque arising from the harmonic content of the machine voltages and currents, and the other is the cogging torque. As the cogging, is an inherent characteristic of PMGs, it affects the self-start ability and produces noise and mechanical vibration. The cogging torque is a serious concern in low power applications of PMGs.

In general, cogging torque is the torque produced by the shaft when the rotor of a PMG is rotated with respect to the stator at no load condition. The cogging effect is the attraction between the magnets and the stator poles when at rest; this attraction and cogging is easily felt when trying to turn an electric motor by hand. An unequal attraction between the magnets and the stator results in the rotor's reluctance to turn. The magnets sit comfortably at rest over a pole, and when the rotor is turned, they must move over an air gap, before reaching the next pole. The rotor resists the turning while the magnets attempt to stay bonded to their current poles, until just over halfway through the air gap where the attraction to the next pole is stronger than that of the previous pole, resulting in a "clunking" or jumping effect at low speeds (as in trying to turn by hand). This is the cogging effect, resulting in a large torque required to begin rotation.

The cogging torque considered for two [26] specific situations in case of water turbines, are:

Water Turbine Start-up: During start-up both, the rotor speed as well as the TSR are low. At low TSR, the C_p of the turbine is also low, thus it creates a low hydrodynamic power. Therefore, it is desirable that during start-up the cogging torque of the PM

generator is low enough that the aerodynamic power can overcome it. Otherwise, with a large cogging torque, the water turbine may never start.

Water Turbine Running Condition: Small water turbines typically have lower rotor inertia than large turbines due to shorter blades and lower mass. Thus, the cogging torque excites the structure of the water turbine and the smoothing effect of inertia is not very dominant. This is particularly apparent in a small water turbine during low water speeds, when the rotor rotational speed is low. Noise and mechanical vibrations may be excited by the cogging torque. This type of vibration may threaten the integrity of the mechanical structure of an improperly designed small water turbine. In high water speeds, the amount of torque and the kinetic energy stored in the rotor is large enough so that the cogging torque is rendered insignificant.

5.2.4 Elimination of Cogging Torque

There are many techniques [25-26] associated with the reduction of a cogging torque in PMGs. These techniques include:

- Odd number of stator coils and even number of magnets
- Skewing stator stack or magnets
- Using fractional slots per pole
- Modulating drive current waveform
- Optimizing the magnet pole arc or width

Almost all techniques used to reduce the cogging torque can also reduce the generated electromotive force (EMF) and result in lower efficiencies of PMGs.

A new approach to eliminate the cogging torque has been proposed [25] by one of the Seaformatics group member and the generator prototype is under construction. In that approach, four strategies have been used together to eliminate the cogging torque, namely TORUS configuration, alternating pole arc, magnet shifting and fractional number of slots per pole.

An ironless axial flux or PCB stator base axial flux permanent magnet generator can also be used where the cogging torque is zero. PCB stator base axial flux PMG is also at the research phase with the Seaformatics Members.

5.2.5 Generator Losses

In general, there are three types of losses in PMGs that are:

- Copper Loss in Stator Winding
- Magnetic Losses
- Mechanical losses

The power lost in the form of heat in the stator winding of a generator is known as Copper loss. Heat is generated any time current flows in a conductor. I^2R loss is the Copper loss, which increases as current increases. The amount of heat generated is also proportional to the resistance of the conductor. The resistance of the conductor varies directly with its length and inversely with its cross-sectional area. Copper loss is minimized in rotor windings by using large diameter wire.

Magnetic losses are also known as an iron or core losses. These losses are mainly divided into hysteresis Loss and eddy current Loss.

Mechanical or Rotational Losses consist of friction loss at bearings and air-friction loss.

5.3 Power Electronic Converters

In general the employment of any power electronic converters are mainly dependent on the type of application. In the designed energy conversion system, the generated electric power is used to power up the marine sensor pods. As a result, an ac-dc rectifier and a dc-dc boost converter are necessary to supply the sensor pods as well as to charge battery. The boost converter (step up) comprising MPPT algorithm has been implemented. As a part of this, the boost converter with its test results has been discussed in next sections, while the MPPT algorithm is discussed in the next chapter.

5.3.1 DC-DC Converter

A dc-dc converter or switch mode power converter is a power electronic system, which converts one level of electrical energy into another level of electrical energy through a set of sequential switching actions. These converters are employed in a variety of applications, including power supplies for personal computers, office equipment, spacecraft power systems, laptop computers, and telecommunications equipment, as well as dc motor drives.

A simple dc-dc converter circuit consists of two semiconductor switching elements (usually one MOSFET and one diode), an inductor, and a capacitor, as shown in Figure 5.3. The arrangement of these switches and the active elements defines the topology of the converter. The principal merits of the switching converter are its high conversion efficiency and its high power packing density, which result in significant weight reduction. However, switching converters often require complex control circuits, and

noise or electromagnetic interference (EMI) filters. An input line filter is often required for some applications.

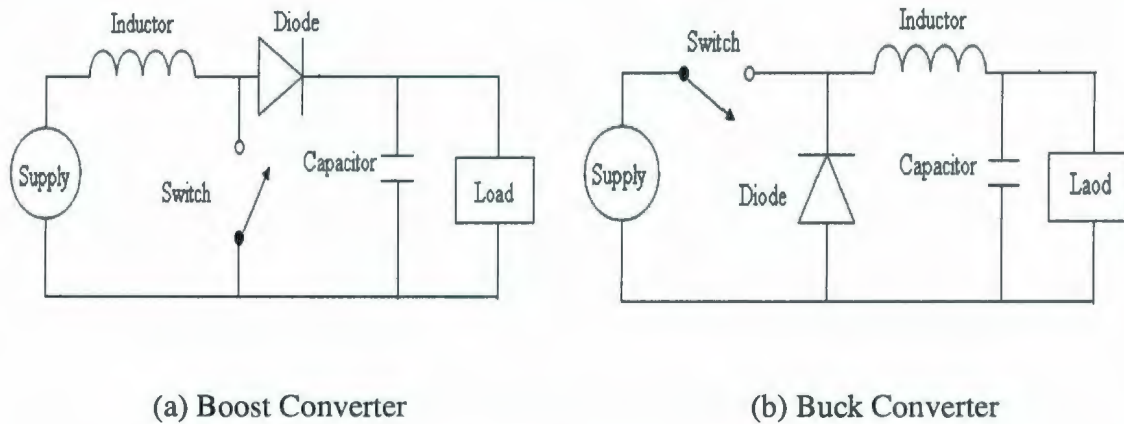


Figure 5.3 Basic Switching converter components

The fundamental concept of the switching converter can be illustrated using the simple switching circuit of Figure 5.4 (a). The switch opens and closes for DT and $(1-D)T$, respectively. D is the duty cycle and is defined as:

$$D = \frac{t_{on}}{T} = t_{on} f_s \quad (5.1)$$

where, f_s is the switching frequency and T is the switching period.

During the time interval DT , the load is connected to the supply voltage V_s , while the load is disconnected from V_s during the time interval $(1-D)T$. The resulting voltage across the load resistor $v_{out}(t)$ is a chopped version of V_s in Figure 5.4(b) shows the waveform of load voltage $v_{out}(t)$. The average value of $v_{out}(t)$ is V_a , which can be expressed as:

$$V_a = \frac{1}{T} \int_0^{DT} V_s dt = \frac{V_s DT}{T} = DV_s \quad (5.2)$$

Equation (5.2) shows that the average value of the output voltage $v_{out}(t)$ is proportional to the duty cycle D . When the duty cycle is one, the output will be same as the input

voltage. In such a case, there is no switching action and the switch is closed at all times.

The average load current I_a can be determined using Ohm's law as:

$$I_a = \frac{V_a}{R_L} = \frac{DV_s}{R_L} \quad (5.3)$$

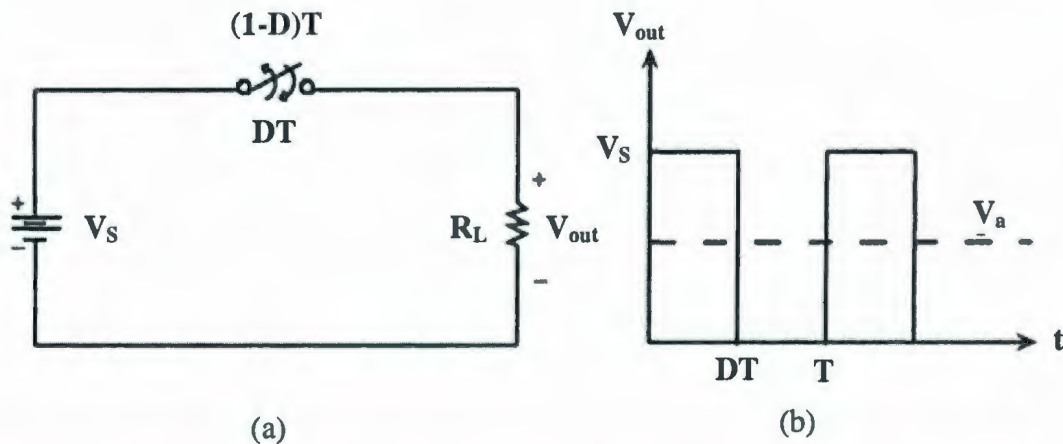


Figure 5.4 (a) Fundamental switching converter circuit (b) voltage waveform across load resistor, R_L

The root-mean-square (rms) value of the output voltage $v_{out}(t)$ can be stated as:

$$V_{out,rms} = \sqrt{\frac{1}{T} \int_0^{DT} V_s^2 dt} = V_s \sqrt{D} \quad (5.4)$$

The average input power of this switching converter, assuming a V_{ce} drop across the switching MOSFET, is calculated as:

$$P_{in} = \frac{1}{T} \int_0^{t_{on}} V_s i_a dt = \frac{1}{T} \int_0^{t_{on}} \frac{V_s (V_s - V_{ce})}{R_L} dt = \frac{V_s (V_s - V_{ce}) t_{on}}{R_L T} \quad (5.5)$$

Also, the output power P_0 is calculated as:

$$P_0 = \frac{1}{T} \int_0^{t_{on}} \frac{(V_s - V_{ce})^2}{R_L} dt = \frac{t_{on}}{T} \frac{(V_s - V_{ce})^2}{R_L} \quad (5.6)$$

Calculating both P_{in} and P_o can facilitate evaluating the efficiency of the converter circuit as:

$$\eta = \frac{P_o}{P_{in}} = \frac{V_s - V_{ce}}{V_s} \quad (5.7)$$

As seen from equation (5.7), the conversion efficiency can be increase by increasing input voltage, V_s .

There is various types of dc-dc converter, each of which tends to be more suitable for specific types of applications. It is worth mentioning that dc-dc converters can be categorized based on their ability to provide dielectric isolation between their input and output sides. Needless to say that this can be very important for some applications, although it may not be important in many others. In general, dc-dc converters are classified based on the ratio of output voltage and input voltage. Considering both approaches to distinguish between different dc-dc converters, the following provide general classification of these electronic converters:

A. Non-isolating converters

- i. Buck Converter (Step Down)
- ii. Boost Converter (Step-Up)
- iii. Buck-Boost converter
- iv. Cuk Converter

B. Isolating converters

- i. Flyback Converter
- ii. Forward Converter

Figure 5.5 shows the relationship of the voltage ratio and the duty cycle for the buck, boost and buck-boost converters.

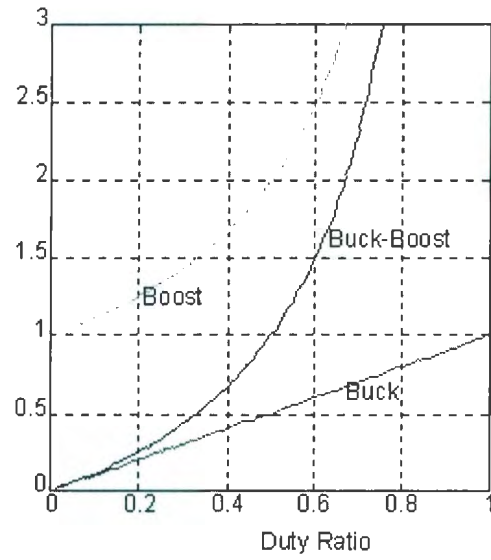


Figure 5.5 Voltage ratio and duty cycle of dc-dc converters

For this project, a dc-dc converter is needed for providing the required voltage level in order to charge the used battery.

5.3.2 Boost Converter Design Equations

The boost dc-dc converter is capable of providing an output voltage $v_{out}(t)$ that higher than its input voltage V_S . It is known as a *ringing choke* or a step-up converter. The circuit diagram of boost dc-dc converter using a power MOSFET switching element is shown in Figure 5.6.

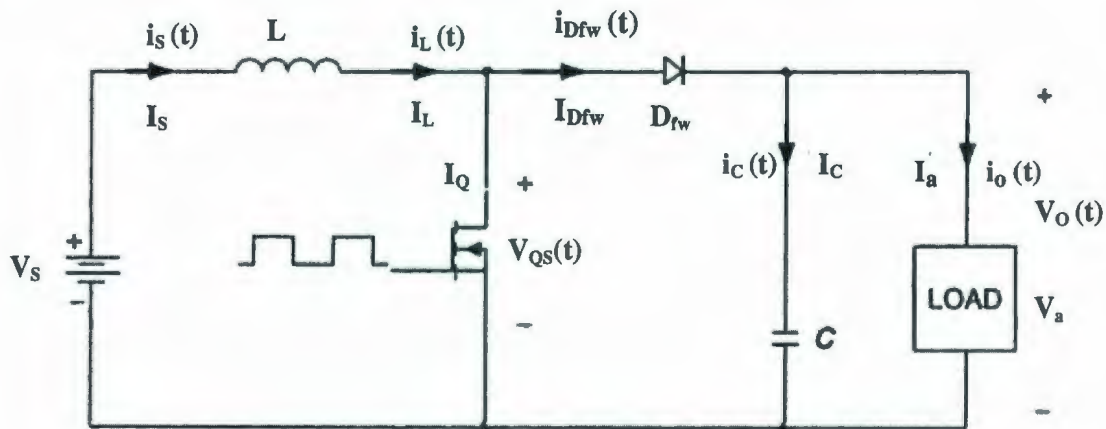


Figure 5.6 The circuit diagram of a boost converter

The switching waveforms of the dc-dc boost converter of Figure 5.6 are shown in figure 5.7. The dc-dc operation of the boost converter can be divided into two modes, depending on the status of the MOSFET switching element. There are two possible modes of operating a dc-dc boost converter; namely the continuous mode ($I_L(t)$ is continuous) and the discontinuous mode ($I_L(t)$ is not continuous) . In this work, the dc-dc boost converter is used to charge the battery, which demands continuous mode of operation.

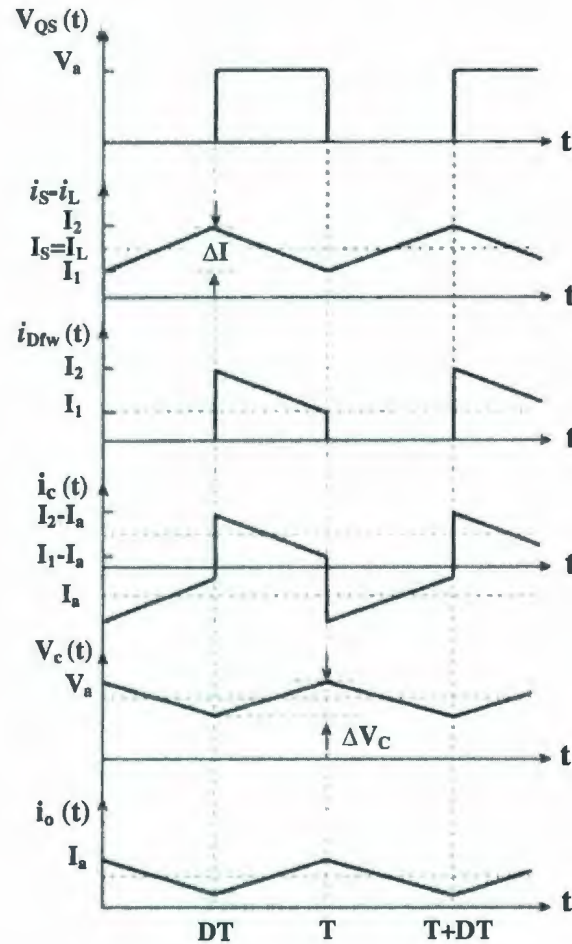


Figure 5.7 The switching waveforms for the dc-dc boost converter (continuous mode)

Continuous Mode Conduction: When a boost converter operates in continuous mode, the current through the inductor (L) never falls to zero. Continuous mode conduction can be discussed in two different modes named as mode1 and mode2.

Model ($0 < t \leq t_{on}$): Model1 of continuous mode conduction begins when the switching MOSFET Q_S is switched ON at $t = 0$ and OFF at $t = t_{on}$ (i.e., $0 < t \leq t_{on}$). The equivalent circuit for mode1 is shown in Figure 5.8.

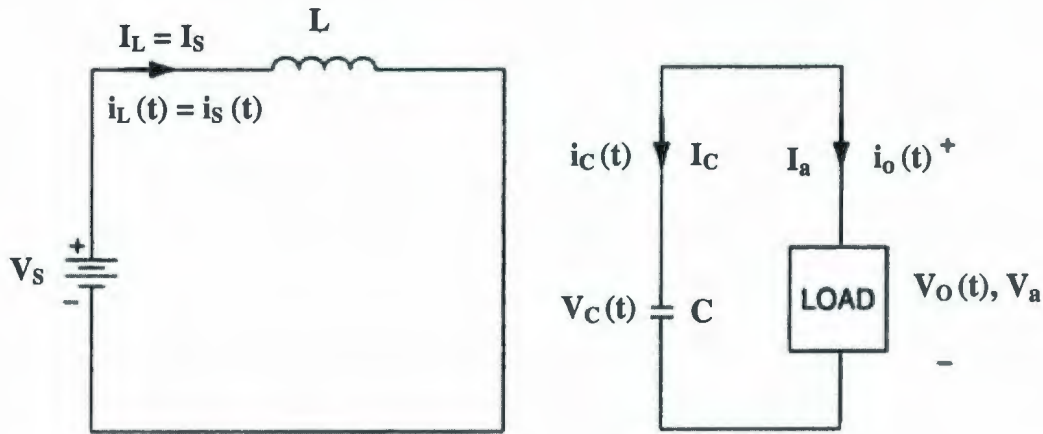


Figure 5.8 Mode 1 equivalent circuit for the boost converter ($0 < t \leq t_{on}$)

The diode D_{fw} is reverse biased since the voltage drop across the MOSFET Q_S is smaller than the output voltage $V_o(t)$. The inductor current $i_L(t)$ ramps up linearly from I_1 to I_2 in time t_{on} . This can be expressed as:

$$V_S = L \frac{I_2 - I_1}{t_{on}} = L \frac{\Delta I}{t_{on}} \quad (5.8)$$

The duration of this interval t_{on} can be expressed as:

$$t_{on} = \frac{L \Delta I}{V_S} \quad (5.9)$$

The energy stored in the inductor E is calculated as:

$$E = \frac{1}{2} L (\Delta I)^2 = \frac{1}{2L} V_S^2 t_{on}^2 \quad (5.10)$$

The output current during this interval is supplied entirely from the capacitor C , which is chosen large enough to supply the load current during t_{on} , with a minimum specified drop in output current.

Mode 2 ($t_{on} \leq t < T$): Mode 2 begins when the MOSFET Q_S is switched OFF at $t = t_{on}$. The equivalent circuit for this mode is shown in Figure 5.9. Since the current in the inductor

$I_L(t)$ cannot change instantaneously, the voltage across the inductor reverses its polarity in an attempt to maintain a constant $I_L(t)$. The current, which was flowing through the switching MOSFET Q_S , would now flow through L , C , diode D_{fw} , and the load. The inductor current $I_L(t)$ starts decreasing until the MOSFET Q_S is turned on again in the next cycle. The inductor delivers its stored energy to the capacitor C and charges it up via

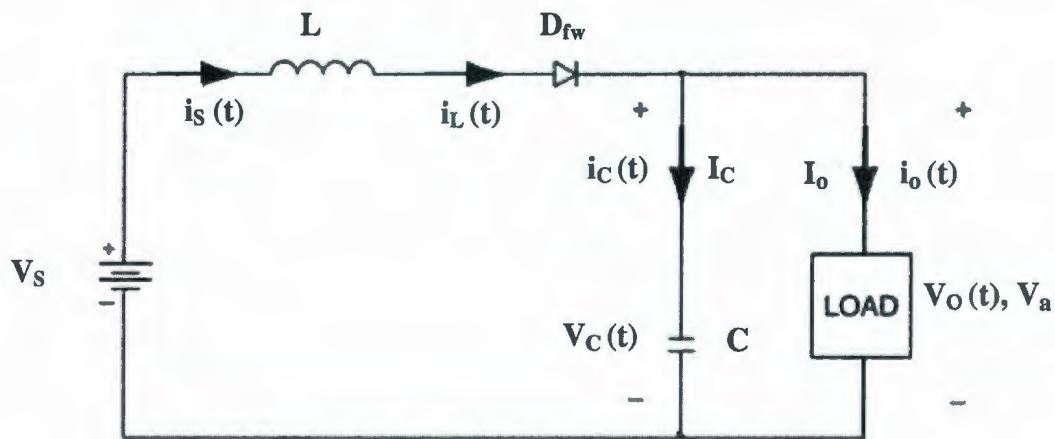


Figure 5.9 Mode2 equivalent circuit for the boost converter ($t_{on} \leq t < T$)

the diode D_{fw} to a higher voltage than the input voltage V_S . This energy supplies the current and replenishes the charge drained away from the capacitor C during t_{on} . The voltage across the inductor is $(V_S - V_a)$ and its current falls linearly from I_2 to I_1 in time t_{off} . This can be described as:

$$V_S - V_a = L \frac{I_1 - I_2}{t_{off}} \quad (5.11)$$

Let, $\Delta I = I_2 - I_1$, Substituting ΔI in equation (5.11) yields,

$$V_a - V_S = L \frac{\Delta I}{t_{off}} \quad (5.12)$$

The duration of the interval t_{off} can be expressed as:

$$t_{\text{off}} = \frac{L\Delta I}{V_a - V_s} \quad (5.13)$$

Since the change in the peak-to-peak current ΔI is the same during t_{on} and t_{off} for steady state operation, it can be shown from equations (5.9) and (5.13) that

$$\Delta I = \frac{V_s t_{\text{on}}}{L} = \frac{(V_a - V_s) t_{\text{off}}}{L} \quad (5.14)$$

Substituting $t_{\text{on}} = DT$ and $t_{\text{off}} = (1-D)T$ into equation (5.13) provides:

$$V_s DT = (V_a - V_s)(1-D)T = V_a(1-D)T - V_s(1-D)T \quad (5.15)$$

Simplifying the above equation, as:

$$V_s DT = V_a(1-D)T - V_s T + V_s DT \quad (5.16)$$

Or,

$$V_s = V_a(1-D) \quad (5.17)$$

The average output voltage V_a of a boost converter operated in the continuous mode can be stated as:

$$V_a = \frac{V_s}{1-D} \quad (5.18)$$

Equation (5.18) indicates that the average output voltage V_a is inversely proportional to $(1-D)$. Since the duty cycle D is selected as $0 < D < 1$, the relationship between the input current I_s and the output current I_o can be derived as:

$$V_s I_s = V_a I_a = \frac{V_s I_a}{(1-D)} \quad (5.19)$$

Or,

$$I_s = \frac{I_a}{(1-D)} \quad (5.20)$$

Note that the average output current I_a is reduced by the factor of $(1-D)$ from the average input current since the output power can only be, at best, equal to the input power. The switching period T is the sum of t_{on} and t_{off} as:

$$T = \frac{1}{f_s} = t_{on} + t_{off} = \frac{L\Delta I}{V_s} + \frac{L\Delta I}{V_a - V_s} = \frac{L\Delta I V_a}{V_s(V_a - V_s)} \quad (5.21)$$

The peak-to-peak inductor current ripple ΔI is stated as:

$$\Delta I = \frac{V_s(V_a - V_s)T}{LV_a} = V_s \frac{(V_s/(1-D)) - V_s}{f_s LV_a} \quad (5.22)$$

Simplifying the above equation produces:

$$\Delta I = \frac{V_s D}{f_s L} \quad (5.23)$$

From equation (5.23), it can be seen that the magnitude of the peak to peak inductor current ΔI is inversely proportional to the switching frequency f_s and the inductance L .

Furthermore, the average inductor current can be expressed as:

$$I_L = \frac{\Delta I}{2} = \frac{V_s D}{2f_s L} \quad (5.24)$$

Since the average input current I_s is also equal to the average inductor current, I_L , then

$$V_s \frac{V_s D}{2f_s L} = \frac{V_a^2}{R} \quad (5.25)$$

In order to ensure that $I_L \neq 0$ (continuous mode), the critical value of the inductance, L_c can be evaluated as:

$$L_c = \frac{RD(1-D)^2}{2f_s} \quad (5.26)$$

The boost converter will be operating in the discontinuous mode if the load resistance R , is greater than its critical resistance R_c , which is given as:

$$R_c = \frac{R_{nom}}{D(1-D)^2} \tag{5.27}$$

Where, R_{nom} is given as,

$$R_{nom} = 2f_s L$$

5.3.3 Designed Boost Converter

A dc-dc boost converter is designed and built in the laboratory using aforementioned discussion. MATLAB is used to determine the designed circuit parameters (See Appendix C.1). MATLAB, as well as Multisim (version10.1), are used to investigate the performance of the designed converter. The schematic diagram is shown in Figure 5.10.

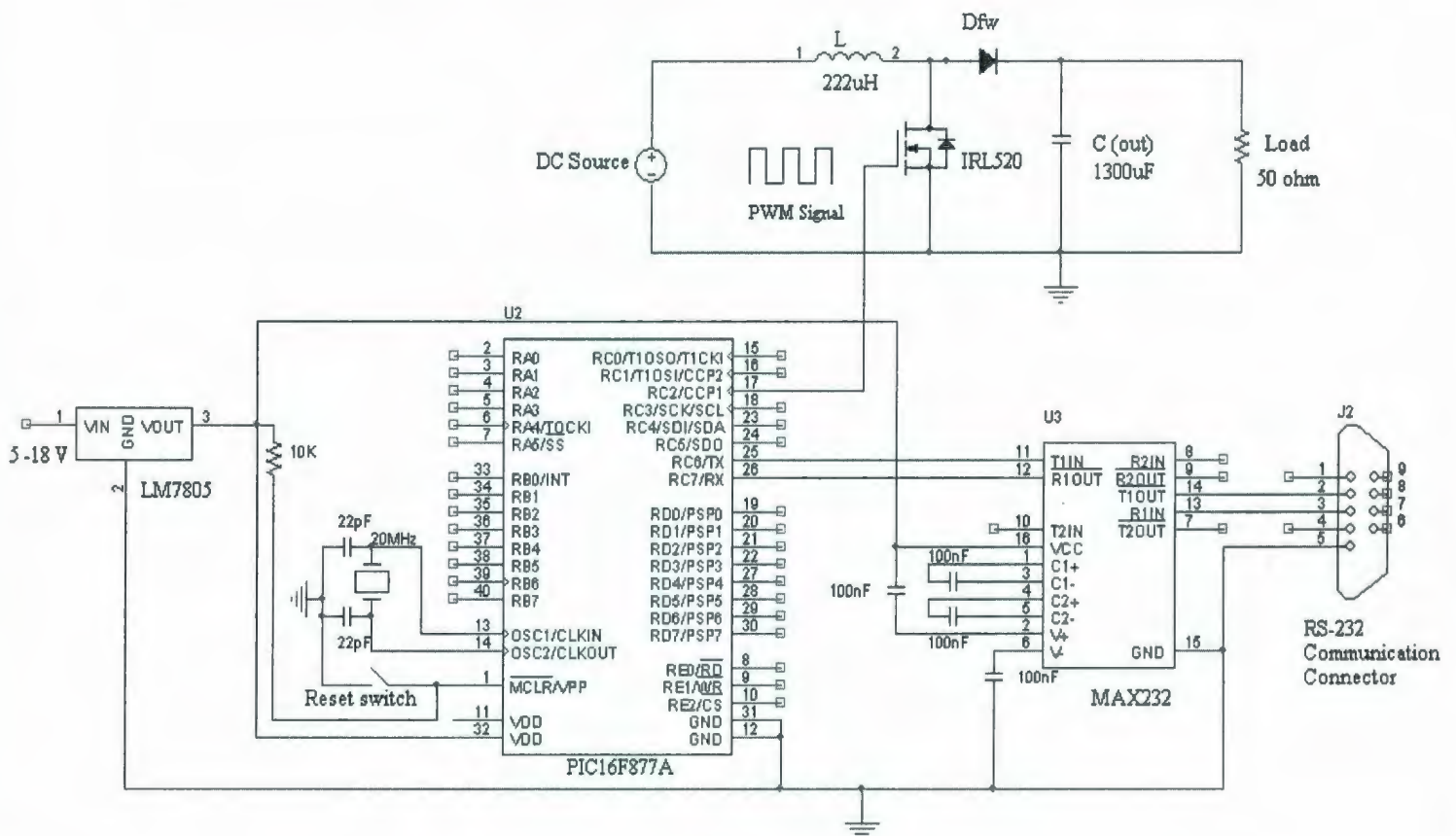


Figure 5.10 The schematic diagram of the designed boost converter (using a microcontroller)

A ferrite core based inductor ($222\mu\text{H}$) (commonly used for low power application (1W-100W) and low switching frequencies (1 to 50 KHz usually)) is utilized during the inductor design, the inductor peak current should not exceed the core saturation current. As a switching element, MOSFET is selected due to its high switching capabilities, low current for ON switching and thermal characteristics. In addition, a microcontroller (PIC16F877A) that can generate a 10 KHz PWM signal is used to switch the MOSFET.

There are two basic switching mechanisms of the MOSFET that are the soft and hard switching. Popular soft switching mechanisms include, but are not limited to, zero-voltage switching, zero-current switching, multi resonant switching and lossless snubber. Hard switching mechanisms refers to turning ON and OFF to the MOSFET as fast as possible. A hard switching mechanism has less switching losses but it needs higher current to carry out the switching. On the other hand, the microcontroller can supply only 20mA, which cannot realize hard switching mechanism. As a result, a logic level enhancement mode MOSFET (IRL520, V_{GS} is 4V-5V) is used as a switching element in order to avoid the driver circuit. Moreover, an ultrafast MUR815 switching diode is used in the designed converter as well as a $1300\mu\text{F}$, electrolytic capacitor is used as an output filter. Figure 5.11 shows the actual built dc-dc boost converter.

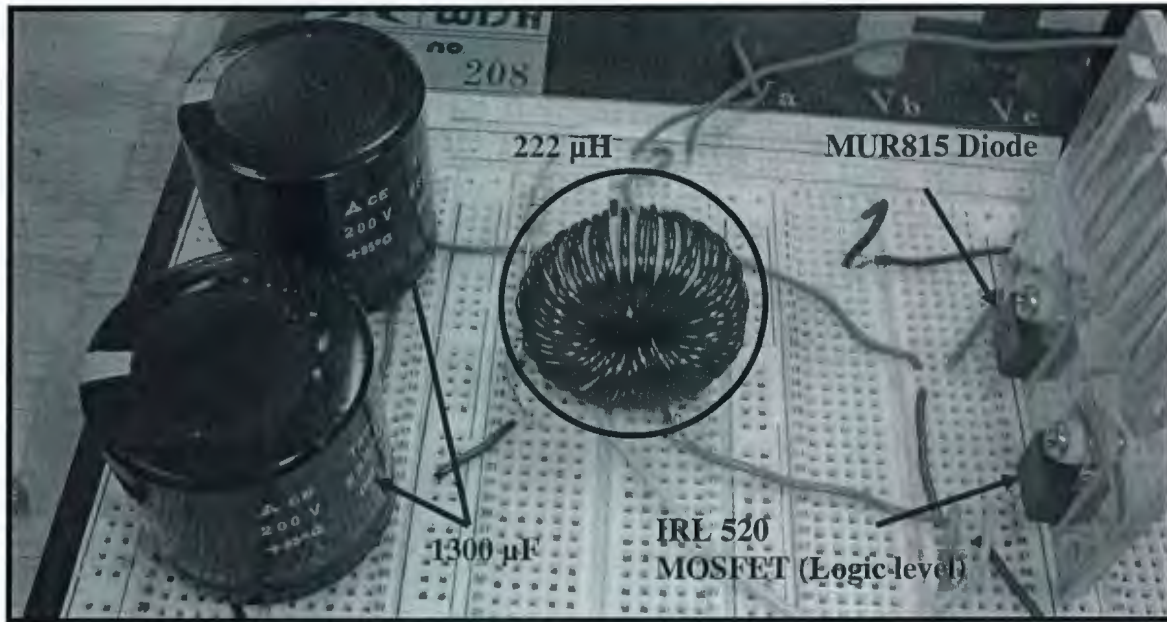


Figure 5.11 The designed dc-dc boost converter

Table 5.1 provides a summary of the used components to build the dc-dc boost converter.

Table 5.1 Designed Boost Converter Components

Component Name	Model /Value/Description	Quantity
Inductor	222 μ H	1
MOSFET	IRL 520 (Logic level)	1
Diode	MUR 815	1
Electrolytic Capacitor	680 μ F	2
Microcontroller	PIC16F877A	1
Compiler	CCS C	1

5.3.3.1 Theoretical and Experimental results

Once the designed dc-dc boost converter is constructed, its experimental performance can be investigated. Several experimental tests are conducted and the results are presented in this section.

Figure 5.12 shows the output voltage versus input voltage of the designed dc-dc boost converter. Theoretical values are compared with the experimental values through this figure. The experimental values are less than the theoretical ones due to voltage drops in different parts of the converter, including diode. More than 12 Volt output is achieved for an input of 5.5 Volt (at 66.67 % duty ratio). Although theoretical values of $V_{out}(t)$ are three times input voltage V_s , experimental values hardly reached to that level. Increasing voltages has increased the losses within the different components of the circuit and, hence increased the difference between the investigated performances.

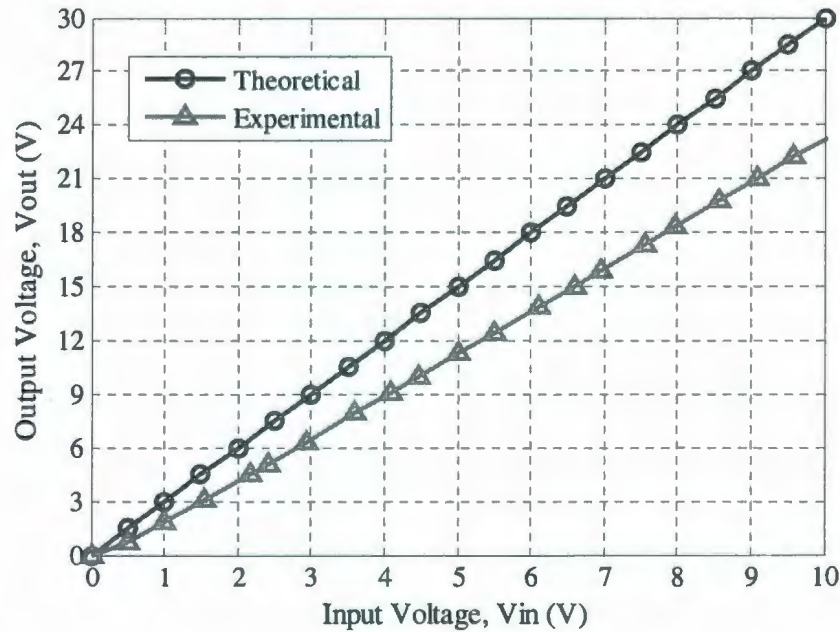


Figure 5.12 Output voltage vs. input voltage

Figure 5.13 demonstrate the output current versus output voltage of the designed boost converter. Experimental data closely follow the theoretical one. However, at 5.5 volt of experimental input voltage, almost 0.1A current flows through the 50 Ω load.

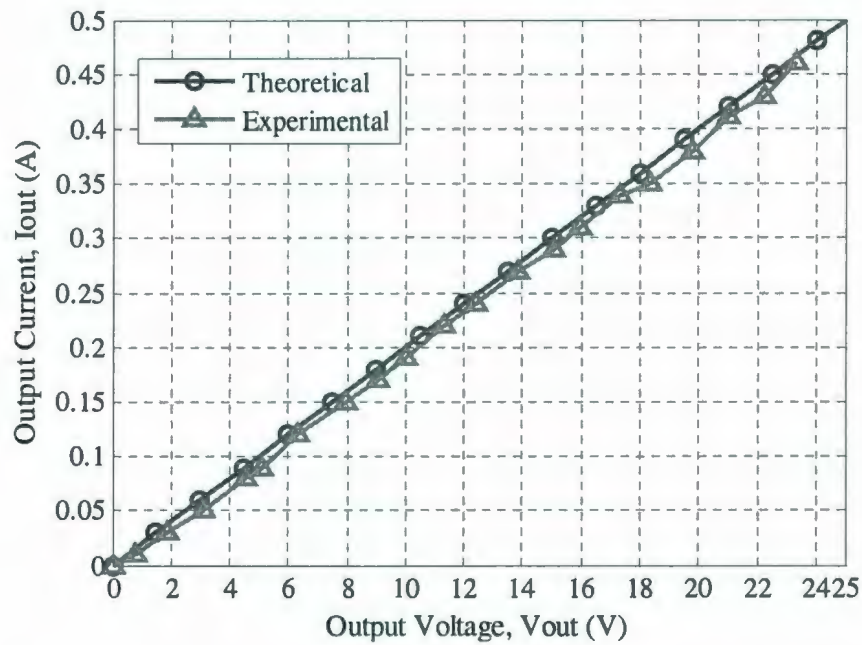


Figure 5.13 Output current vs. output voltage

Figure 5.14 shows the output power versus input voltage of the designed dc-dc converter. As can be seen from the figure 5.14, differences between theoretical and experimental values increase as V_{in} increases.

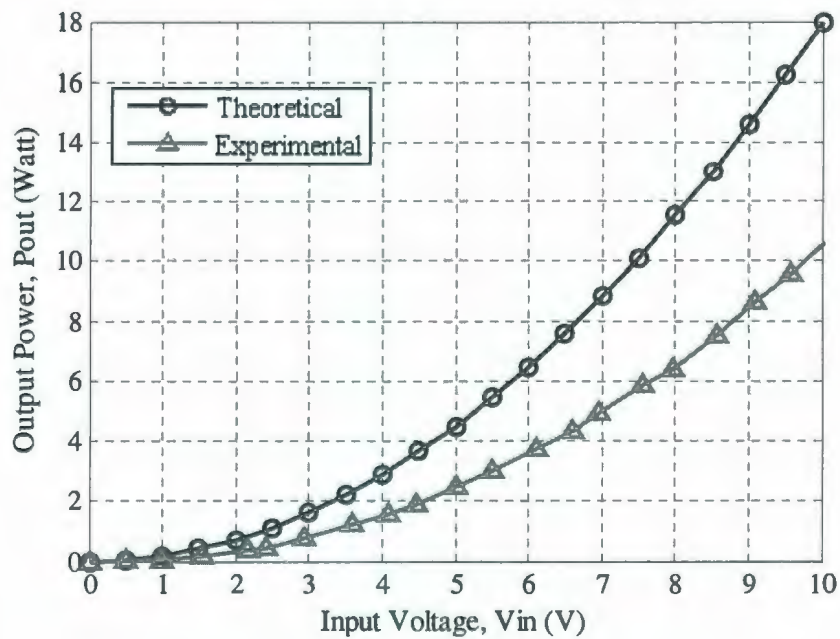


Figure 5.14 Output power vs. input voltage

Figure 5.15 shows an important characteristic curve for a dc-dc converter that is the efficiency of the converter. As for the designed dc-dc boost converter the efficiency has increased with the increase of the input voltage. Though some variations are visible throughout the test data, the efficiency almost remains constant (65%-70%) between the voltages around 4.8V to 10V.

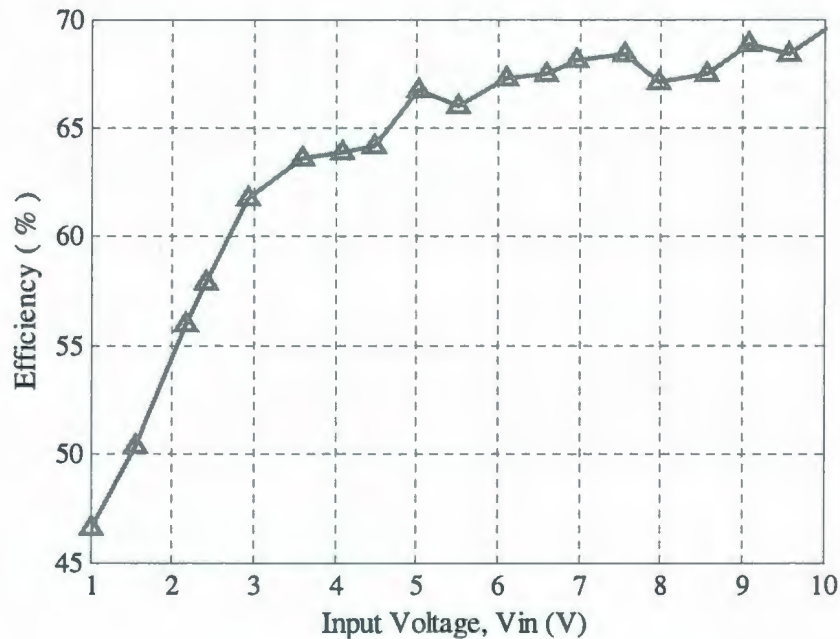


Figure 5.15 Efficiency vs. input voltage

5.3.3.2 Pulse Width Modulation (PWM)

The pulse width modulation (PWM) technique is very popular that holds a wide range of application in power electronics including switched-mode power supplies. In general, for a dc-dc converter, the switching process is used to perform the regulatory function by interrupting the flow of current from the unregulated supply.

The technique of modulating the duration of the ON or OFF pulses, or both, that are applied to the switching element is called pulse-width modulation (PWM). There are two

schemes of PWM, the fixed frequency and the variable frequency PWM. The major problem associated with the variable-frequency PWM is the unpredictable electromagnetic interference (EMI), due to the varying switching frequencies. On the other hand, the fixed-frequency PWM is more popular due to its ease of implementation by commercially available integrated-circuit controllers, and because its generated EMI can be easily filtered out.

PWM signals can be generated in a number of methods, including analogue, digital, discrete IC and onboard microcontroller methods.

Since a peripheral interface controller (PIC) (discussed in the next chapter) is easier and flexible to implement by avoiding additional hardware, the onboard microcontroller methods has been used for generating the PWM signals.

A Microchip PIC 16F877A is used as a microcontroller. The CCS C compiler, comprised of standard C operators and built-in libraries, is used for programming the 16F877A chip. The used PIC Microchip's 16F877A includes two on-chip PWM units, which has a selectable on-time and, a period. In order to start PWM operation, the software should be structured as:

- Set the period in the on-chip timer/counter to provide a modulating square wave
- Set the on-time in the PWM control register
- Set the direction of the PWM output, which is one of the general-purpose I/O pins
- Start the timer
- Enable the PWM controller.

Although, specific PWM controllers do vary in their programmatic details, the basic idea is generally the same. For this work, the microcontroller has been used with a 20 MHz

clock signal frequency. Among three available timers, timer2 is an 8 bit timer with a prescaler and a postscaler. The Timer2 can be used as a time base for the desired PWM signal generation. For setting the PWM frequency, a CCS C command of “*setup_timer_2 (T2_DIV_BY_4, 127, 1)*” is employed, which commands the microcontroller first set the timer2 prescaler, overflow and postscaler values. As a consequence, the frequency of the PWM signal will depend on each of these values and the microcontroller frequency. The cycle time T_s can be calculated using the following formula:

$$T_s = \frac{1}{\text{Clock}} \times 4 \times t2\text{div} \times (\text{period} + 1) \quad (5.28)$$

$$\text{or, } T_s = \frac{1}{20000000} \times 4 \times 4 \times (127 + 1)$$

$$\text{or, } T_s = 102.4 \mu\text{s}$$

$$\therefore \text{PWM Frequency, } f_s = \frac{1}{T_s} = 9.765 \text{ KHz} \approx 10 \text{ KHz}$$

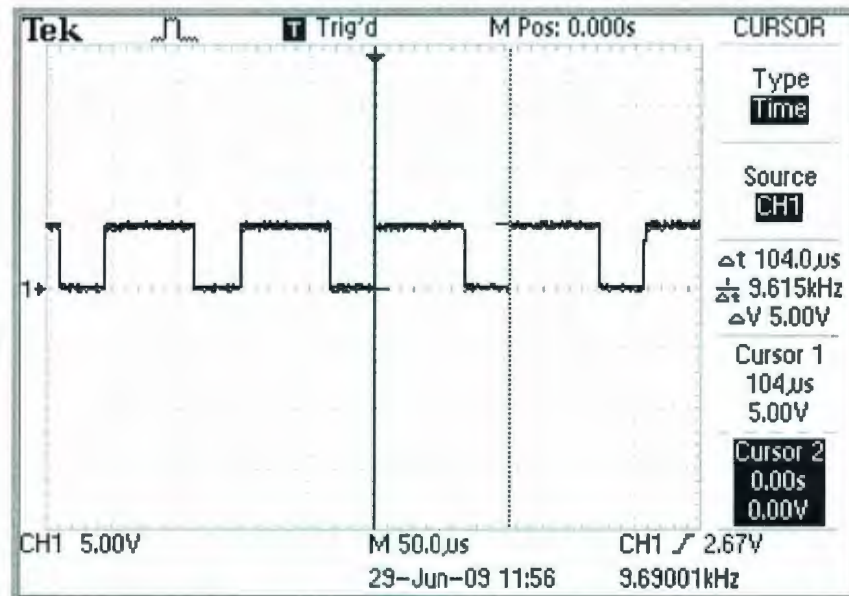


Figure 5.16 Generated PWM Signal with 66.67% Duty Ratio

Figure 5.16 shows an experimental PWM signal generated using the PIC. This signal is collected using a 2-channel Tektronics TDS1002B digital storage oscilloscope. As the converter's designed duty ratio is 66.66%, a numerical value of almost 86 set this duty ratio; 127 provide a 100% duty ratio for the generated PWM signal.

5.4 Energy Storage System

Generally, energy storage systems are the key to expanding the utilization of renewable energy. The variable water current energy production needs an energy storage device, so that it can meet the sensor power requirements.

Among several energy storage devices, batteries are the most popular devices that are available for implementation into the designed MCECS. There are hundreds of types of batteries that are available, which makes selecting the right battery to match all system requirements a daunting task. The best method for speeding up the process to a final selection of a battery is to narrow down the options as much as possible. There are many battery technologies currently being developed, with Lead-Acid (Pb-acid), nickel cadmium (NiCd), and nickel metal hydride (NiMH) as promising technologies.

For the purposes of comparing the advantages and disadvantages of the aforementioned three different types of batteries, the Table 5.2 summarizes different considerable areas, including the specific energy, specific power, specific cost, and cycle life based on estimates from industry experts.

Table 5.2 Pb-acid, NiCad and NiMH Battery Comparison

Areas of Consideration	Lead Acid (Pb-acid)	NiCad	NiMH
Commercialization	1881	1956	1990
Cell Voltage	2.0	1.2	1.2
Energy by Weight: Wh/Kg	30-40	40-60	30-80
Specific Power: W/Kg	180	150	250-1000
Energy by Volume: Wh/L	60-75	50-150	140-300
Max. Discharge Rate	10C		20C
Recharge Time	>10 Hours	8 Hours	6 Hours
Cycle Life Cycles	500-800	2000	1500
Self Discharge (Per Month)	3%-4%	20%	30%
Efficiency	70%-92%	70%-90%	66%
Temp Range °C		-40° to +60°	-20° to +60°
Preferred Charge Method	Constant Voltage	Constant Current (-Delta V)	Dt / dt (-Delta V) and Timer
Average Energy Cost	\$150	\$400-800	\$250
Environmental Impact	Moderate	Very High	Low
<i>Comments</i>	Deteriorates with microcycles	Memory Effect	High self discharge rate useful power down to 50% DOD

By narrowing down the options, when cost, life, efficiency, maintenance, availability and reliability are the major concerns, then for MCECS application, NiMH batteries are suitable as an electrical energy storage device. Nickel-metal-hydride batteries are related to sealed nickel-cadmium batteries and only differ from them in that instead of cadmium, hydrogen is used as the active element at a hydrogen-absorbing negative electrode

(anode). This electrode is made from a metal hydride usually alloys of Lanthanum and rare earths that serve as a solid source of reduced hydrogen that can be oxidized to form protons. The electrolyte is alkaline potassium hydroxide. Like NiCd batteries, Nickel-metal Hydride batteries are susceptible to a "memory effect" although to a lesser extent. However, the cell voltage is 1.2 volts.

5.5 Conclusion

A low rpm permanent magnet generator with low or no cogging torque is desirable for a small marine current energy conversion system. The generator should also be matched with the designed turbine. A boost converter is needed to boost the low voltage output of generator for charging a battery. The designed boost converter has been discussed with its test results. Finally, available batteries are compared and a NiMH battery is selected for energy storage.

CHAPTER 6

EXPERIMENTAL ENERGY CONVERSION SYSTEM

6.0 Introduction

This chapter firstly introduces the maximum power point tracking (MPPT) based control strategy that is common in wind energy conversion systems. Also, this chapter discusses the development of a simple MPPT based control system realized, using perturbation & observation algorithm. The developed energy conversion system details and testing results are presented in this chapter.

6.1 Conventional MPPT- Based Energy Conversion Systems

This section briefly describes the conventional MPPT-based energy conversion systems employed in wind energy applications. There are several wind generator (WG) control systems available to support MPPT based energy conversion systems. Figures 6.1 and 6.2 show general structures of MPPT-based wind energy conversion systems [28, 29].

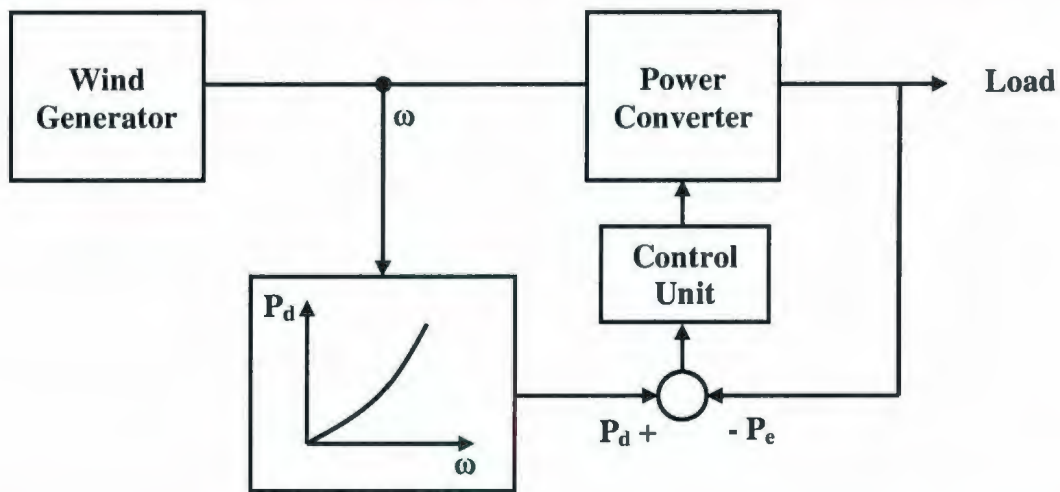


Figure 6.1 Control system based on rotating-speed measurements (WG MPPT Method)

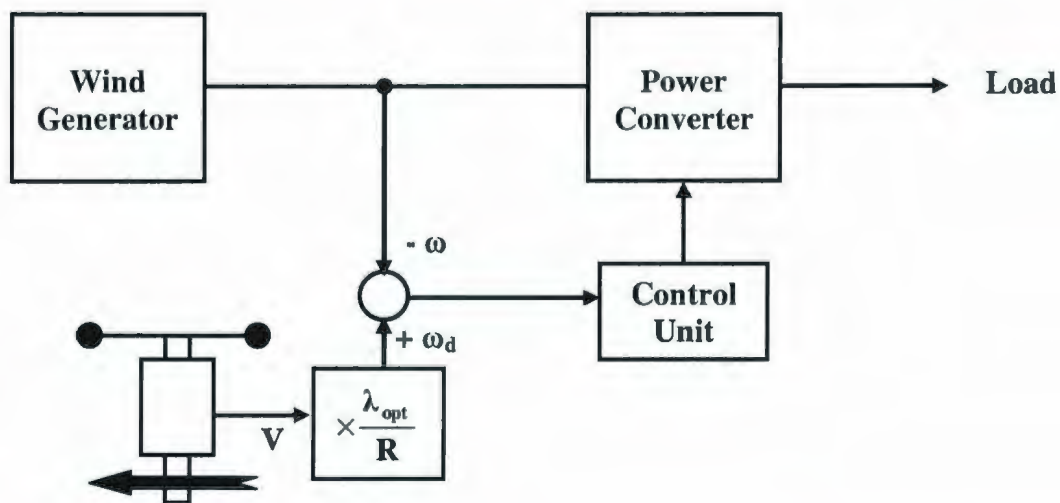


Figure 6.2 Control system based on wind-speed measurements (WG MPPT Method)

The system topology shown in Figure 6.1 is based on the WG optimal power versus the rotating speed characteristic, which is usually realized using microcontroller platforms. The WG rotating speed is measured; then optimal output power is calculated and compared to the actual WG output power. The resulting error is used to control a power interface. A similar version found in [30], the WG output power is measured and the target rotor speed for optimal power generation is derived from the WG optimal power versus rotor-speed characteristic. The target rotor speed is compared to the actual speed and the error is used to control a dc-dc converter.

A control system based on wind speed measurements is shown in Figure 6.2. The wind speed is measured, and the required rotor speed for maximum power generation is computed. The rotor speed is also measured and compared to the calculated optimal rotor speed, while the resulting error is used to control a power interface. Fuzzy-logic, as well as neural network, based control systems for MPPT are also used in some wind energy conversion systems.

The aforementioned MPPT-based wind energy conversion systems can suffer from a difficulty of the required knowledge of the WG optimal power characteristics. Such characteristics are usually not available with a high degree of accuracy, and also changes with rotor aging. An accurate anemometer is also required, for some of above mentioned control systems, which increases the system cost.

6.2 Proposed MCECS

If the previous MPPT-based energy conversion systems are used in the proposed marine current conversion system, then measuring the water current speed or/and the rotation speed of the turbine will be required. Such requirements can decrease the system reliability due measuring errors, system complexity and additional costs to accommodate these measurements. The proposed approach for marine current turbine's MPPT-based control system is shown in Figure 6.3.

In the proposed marine current energy conversion system, the generated mechanical power is used to drive a permanent magnet generator. Then the output voltage of the PM generator is fed to the ac-dc rectifier. The output dc voltage of the rectifier is then supplied to a dc-dc boost converter through a dc filter. The dc output of dc-dc boost converter is then used to charge the battery.

The MPPT-based control in this MCECS is based on monitoring the turbine output power through measuring the turbine output voltage and current, and directly adjusting the dc-dc boost converter duty cycle. The adjustment of the duty cycle is made comparing successive turbine output power values. Thus, neither the knowledge of marine current turbine power vs. the rotor speed of rotation or water- speed characteristic, nor measurements of the rotor speed are required. This MPPT-based control is explained in details during the coming sections.

A resistive dummy load is used to protect the water turbine generator from over-speeding. Although, the proposed method has been tested on a resistive load, it can be easily extended for battery charging using a proper battery charger depending on the

charging method. The PIC microcontroller (16F877A) can easily perform additional operations such as a battery management system.

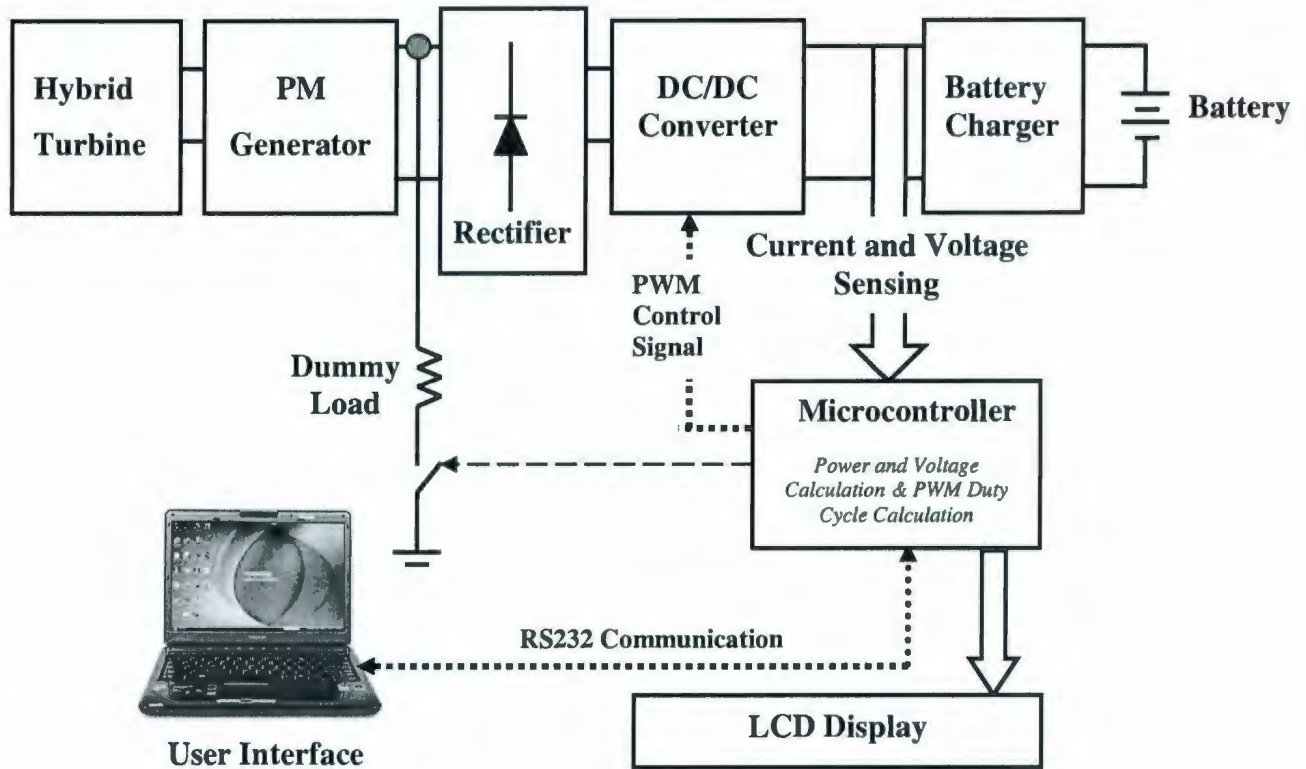


Figure 6.3 The structure of the proposed marine current energy conversion system with MPPT-based control

6.3 Maximum Power Point Tracking

Due to changes in marine currents, it is necessary to extract the available maximum power from the turbine. Using the turbine characteristics, there is a maximum power point for different water speeds as discussed in chapter 4. The devices which are responsible for tracking and operating the system to that maximum point for a specific water speed know as “*Maximum Power Point Tracker*”. Maximizing power means is

meant to deliver the maximum available electrical power to the load side. A MPPT-based control is essentially a specialized switching power supply, where the input and output currents are regulated to achieve equal input and output powers. This can be viewed using figure 6.4.

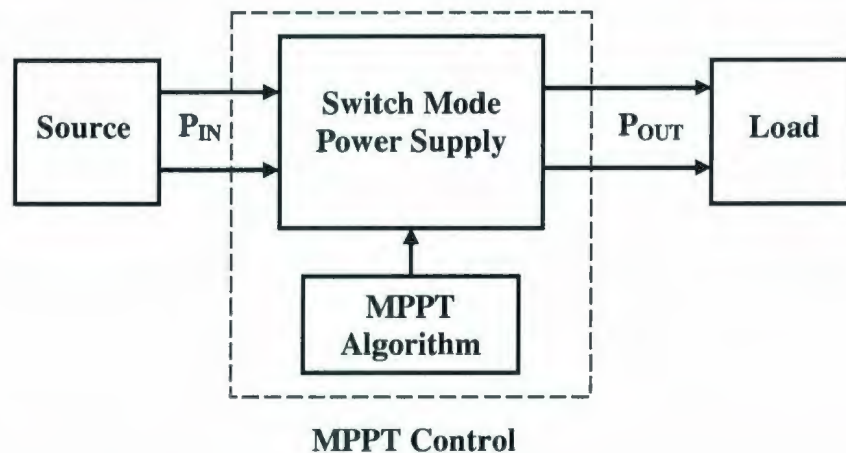


Figure 6.4 The MPPT-based controlled power supply control blocks

If the losses are neglected, then:

$$P_{IN} = P_{OUT} \quad (6.1)$$

The function of MPPT-based controller indicates that any changes in the output voltage will directly affect the output current. Equations (5.18) and (5.20) describe these relations for a dc-dc boost converter. There are several MPPT-based control algorithms available, mostly used in Solar Power systems. Moreover, some of these MPPT-based controllers are utilized in wind energy conversion systems. There are several algorithms to realize MPPT-based controls, among are [31],

1. Perturb and Observe (P&O) Method
2. Incremental Conductance (INC) Method
3. Constant Voltage (CV) Method

Methods 1 and 2 are known as the “*Hill Climbing Method*”. The P & O method is widely used due to its simple implementation in its basic form. There are three main versions [32] of the P & O method including i) conventional P & O ii) modified P & O and iii) estimate perturb and perturb (EPP). The conventional P & O method is discussed in the following subsection.

6.3.1 Conventional P & O Method

The P&O method implementation flow chart is shown in Figure 6.5. After one perturbation the current power is calculated and compared with a previous value to determine the change ΔP . If $\Delta P > 0$, then the operation continues in the same direction of perturbation, otherwise the operation reverses the perturbation direction.

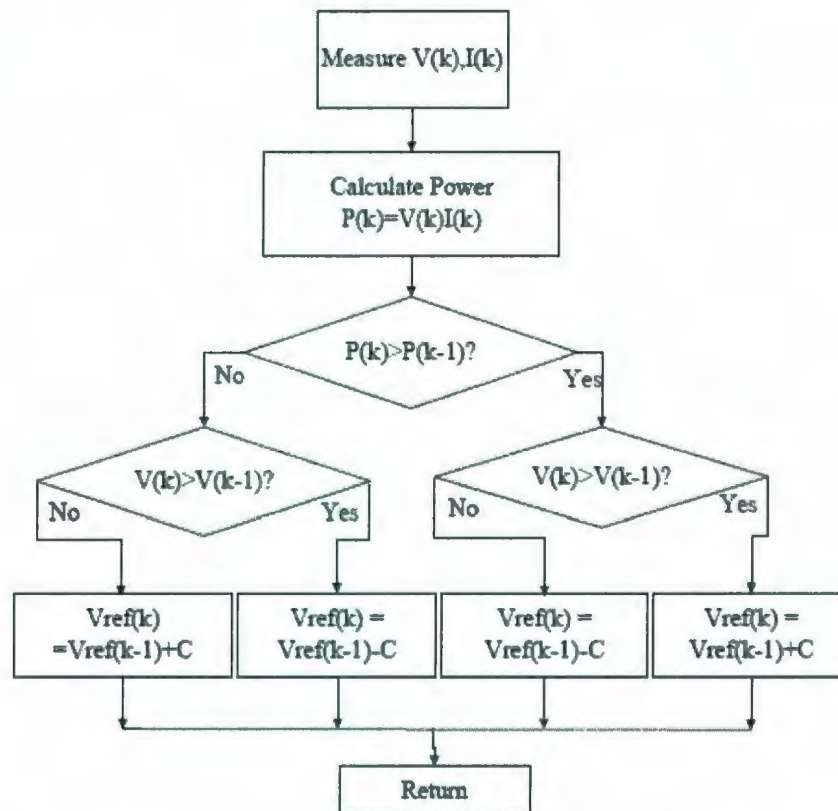


Figure 6.5 Conventional P & O Method

6.3.2 Proposed MPPT Algorithm

The proposed algorithm is based on the perturb and observe (P&O) method, where the operating voltage is perturbed in every MPPT cycle. If the maximum power point (MPP) is reached, then the voltage oscillates around the MPP as shown in Figure 6.6. The voltage perturbation is obtained through changing the duty cycle of the PWM signal.

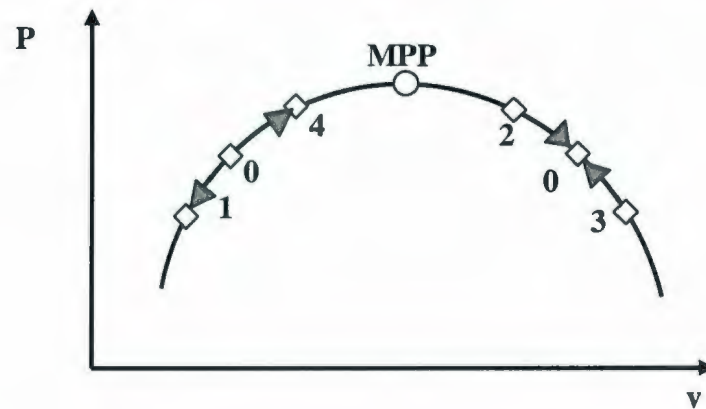


Figure 6.6 The MPPT action

For example, when the microcontroller senses that the $dP < 0$ and $dv > 0$ in case $0 \rightarrow 2$, the PWM duty cycle will be decreased until it reaches to the maximum point. In other cases, the actions are taken according to the Table 6.1.

Table 6.1 MPPT Actions

Case	dP	dv	Action
$0 \rightarrow 1$	< 0	< 0	+
$2 \rightarrow 0$	< 0	> 0	-
$3 \rightarrow 0$	> 0	< 0	-
$0 \rightarrow 4$	> 0	> 0	+

The PIC 16F877A is programmed by the CCS C compiler, which is close to ANSI compatibility. It supports the PIC compiler needs and the necessary superset of ANSI C to work with embedded micros, such as fuse and interrupt level support. The program code is given in Appendix D1, and the flow chart is provided in figure 6.7.

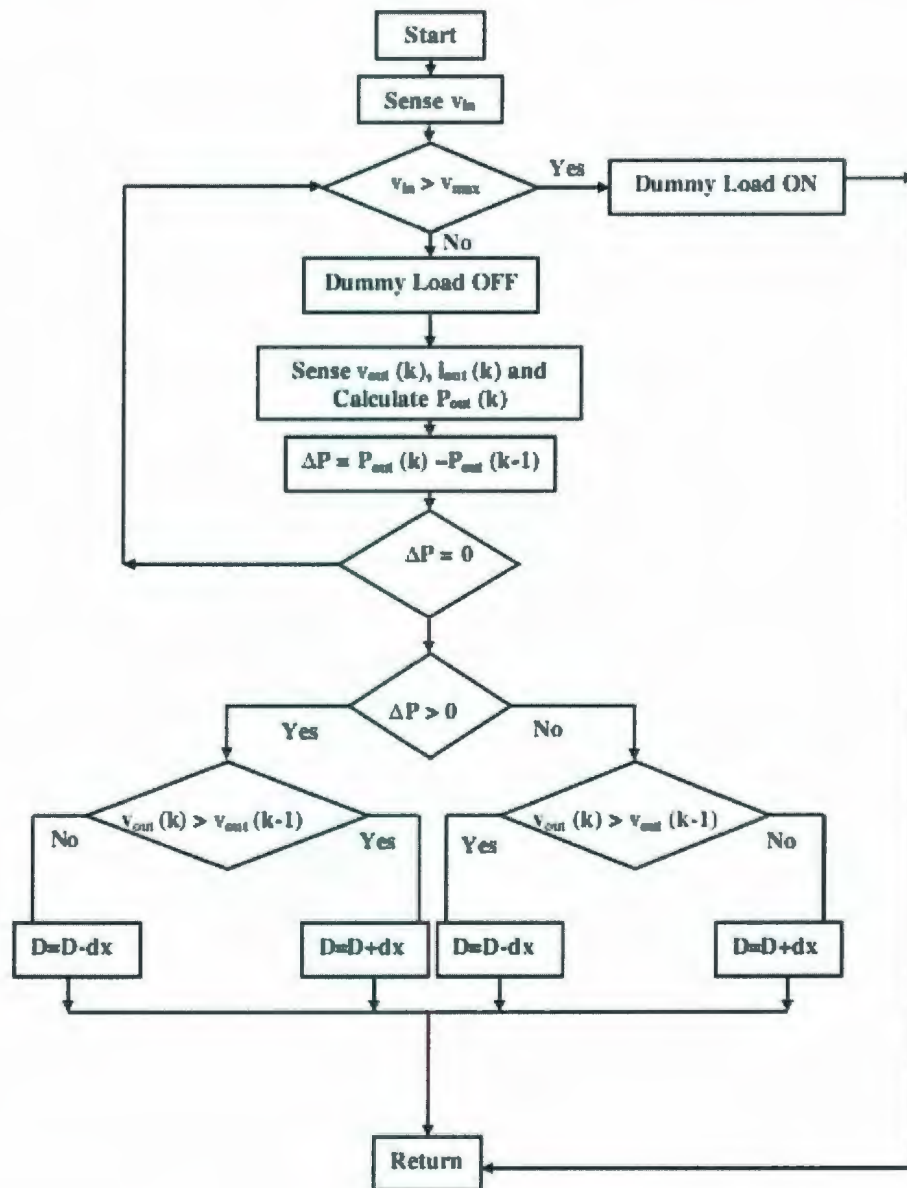


Figure 6.7 The MPPT Flow chart

6.4 Experimental Setup of the Proposed MCECS

The experimental setup of the laboratory test using a 50Ω load is shown in Figure 6.8. For proposed testing the experimental performance of the proposed MCECS, a dc power supply is used as the input of the dc-dc boost converter. First voltage divider (using R1 and R2) is used to sense the input voltage, which actually used to determine the over speeding voltage generated at the input terminal of boost converter. A logic level MOSFET (IRL520) is used for connecting the dummy load according to the sensed voltage. Microcontrollers RB0 pin is used for the switching of first MOSFET. In this case, the dc supply is feeds the dc-dc boost converter through the first divider circuit.

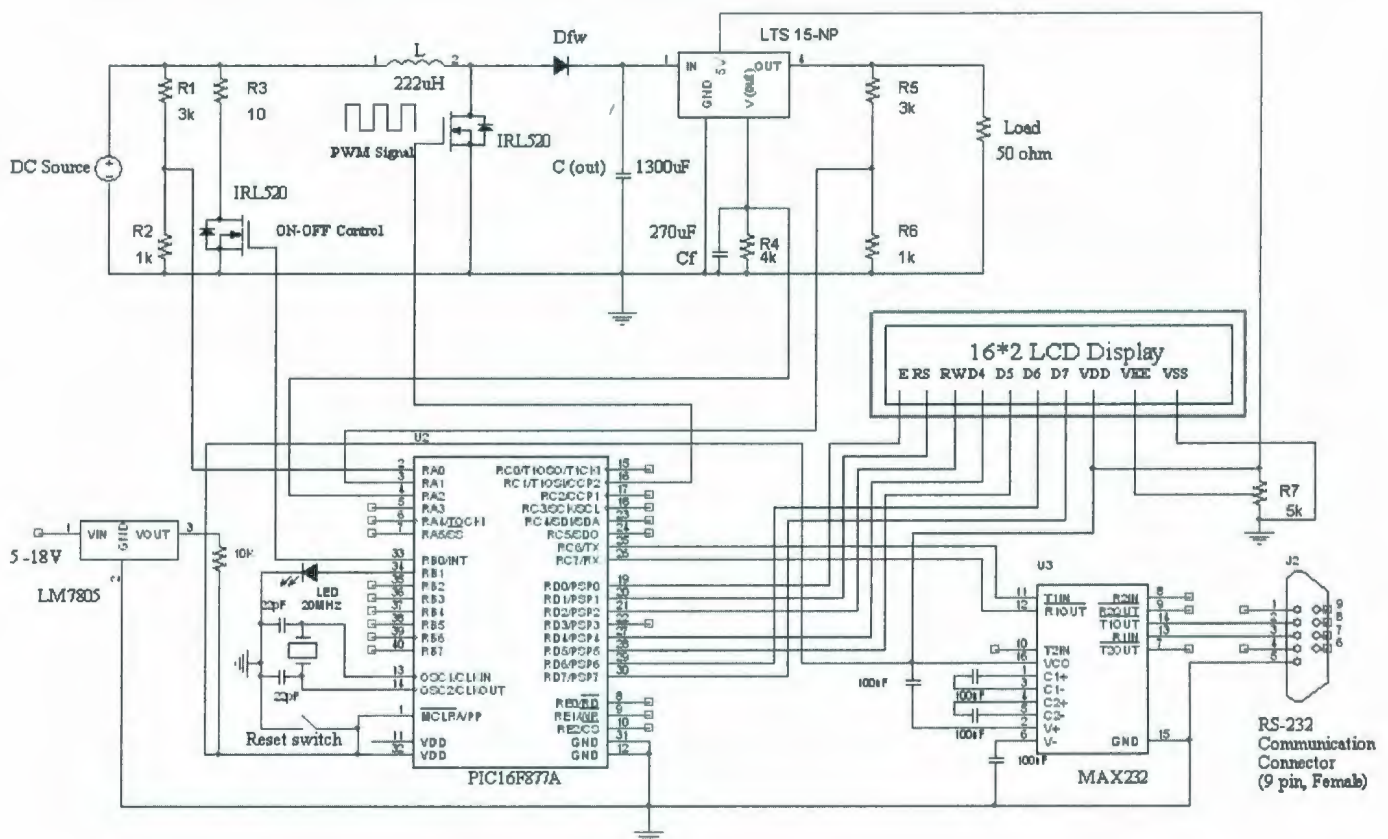


Figure 6.8 The experimental structure of the proposed marine current energy conversion

system

Second MOSFET switching is realized using the PWM signal generated at pin CCP2 for continuous mode. An output capacitor is used on the output side of the dc-dc boost converter. LTS 15-NP current sensor is fed to RC (R4 and Cf) filter circuit to minimize the ripple at the voltage fed to the microcontroller. A second voltage divider is used to sense the output voltage using RA1 channel and the on chip ADC converter of the microcontroller. In addition, a standard RS232 communication is performed between the user terminal (Laptop, Model-TOSHIBA, Intel Celeron, 1.6GHz, 1GB RAM) and the PIC microcontroller. The standard RS232 defines the signal level requirements at the transmitter and receiver. Hence, to make it compatible with the TTL output, an interface IC is employed. The interface IC converts the TTL logic to RS232 standard and vice versa. In this work, MAX 232 is used. A laboratory setup of the energy conversion system is shown in Figure 6.9.

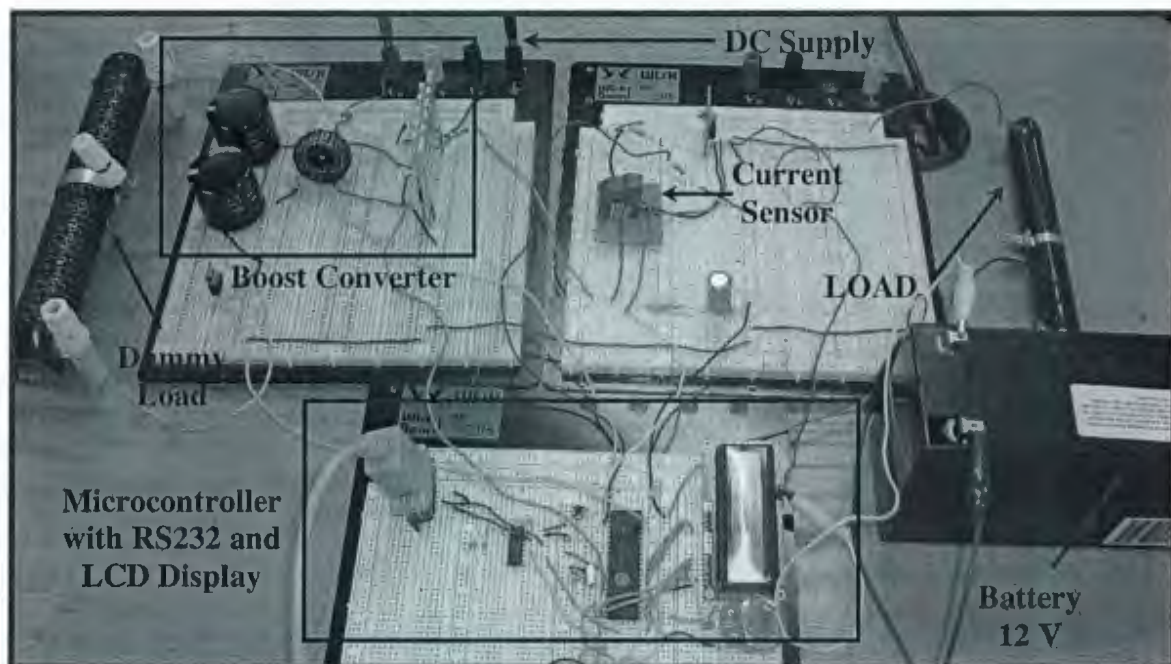


Figure 6.9 Experimental Marine Current Energy Conversion System (Lab Setup)

Several components are used during the design of this converter are listed in Table 6.2.

Table 6.2 Component of the proposed MCECS

Component Name/Label	Model /Value/Description	Quantity
R1,R5	3k Ω	2 (total)
R2,R6	1k Ω	2 (total)
R3	10 Ω (Power Resistor, 300W)	1
R4	4k Ω	1
R7	5 k Ω (Variable)	1
LOAD	50 Ω (Power Resistor, 200W)	1
Inductor (L)	222 μ H	1
C(out)	680 μ F (Electrolytic Capacitor)	2
Cf	270 μ F (Electrolytic Capacitor)	1
Diode	MUR 815	1
MOSFET	IRL 520 (Logic level)	2
5V Regulator	LM 7805	1
Microcontroller	PIC16F877A	1
RS232 Converter	MAX 232	1
Display	16 \times 2 Character LCD Display	1
Compiler	CCS C	1

6.4.1 Current Sensor

Electrical current sensors are used to measure both AC or DC currents. Open loop DC current sensors are preferred in battery-powered applications. They typically take less power to operate and tend to have a high ability to withstand overloads. Closed loop sensors typically offer faster response times with better linearity. They are often preferred in high frequency circuits such as switching power supplies, where they offer quick response and noise immunity. Ratings for current overload are important, as they determine the amount over the standard sensing level that the sensors can handle. A closed loop current transducer modeled as LTS 15-NP (Shown in Figure 6.10) is used for constructing the proposed energy conversion system.

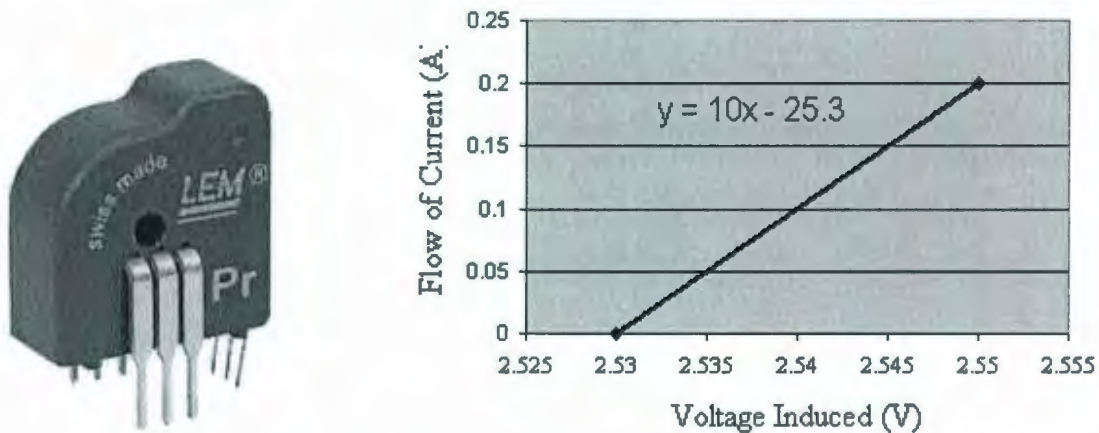


Figure 6.10 LTS 15-NP and its characteristic curve

The above current sensor uses the Hall Effect technology and is designed for 5A, 7.5A and 15A rating. The used LTS 15-NP current sensor's appropriate pins are shorted according to the datasheet to sense a maximum of 5A. It is powered with a +5V supply, while its output voltage is collected using a 4k resistor. Proper calibration is done during

sensing based on the characteristic curve of Figure 6.10. A detailed diagram and pin connections are shown in figure 6.11.

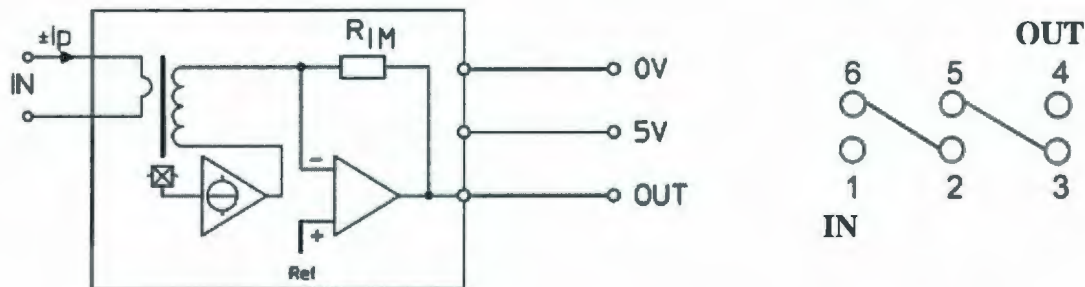


Figure 6.11 The LTS 15-NP current sensor (diagram, pin connections)

6.4.2 Voltage Sensor

The Voltage sensor is composed of a voltage divider and an analog-to-digital (ADC) converter for sensing voltages higher than 5V. A voltage divider is necessary due to the limitation of voltage sensing capability of the PIC microcontroller. As the PIC microcontroller is able to sense up to 5 volts, a voltage divider with some calibration equation can resolve the problem. One of the major aspects of choosing a voltage divider in case of a voltage sensing device is that, the resistive value should be high enough to reduce the current loss at the divider circuit and to provide isolation between the PIC and power circuit. The voltage sensing circuit, used for the proposed energy conversion system is shown in Figure 6.12.

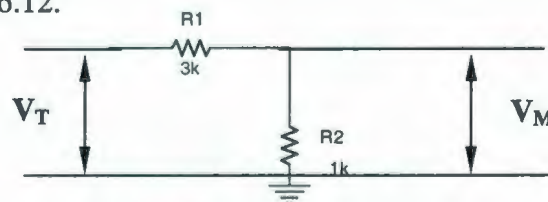


Figure 6.12 The voltage sensor

If V_T is a voltage to be sensed, and V_M is a voltage that is fed to the PIC microcontroller, then the maximum value of V_M is 5V. The voltage sensing circuit of Figure 6.12 can

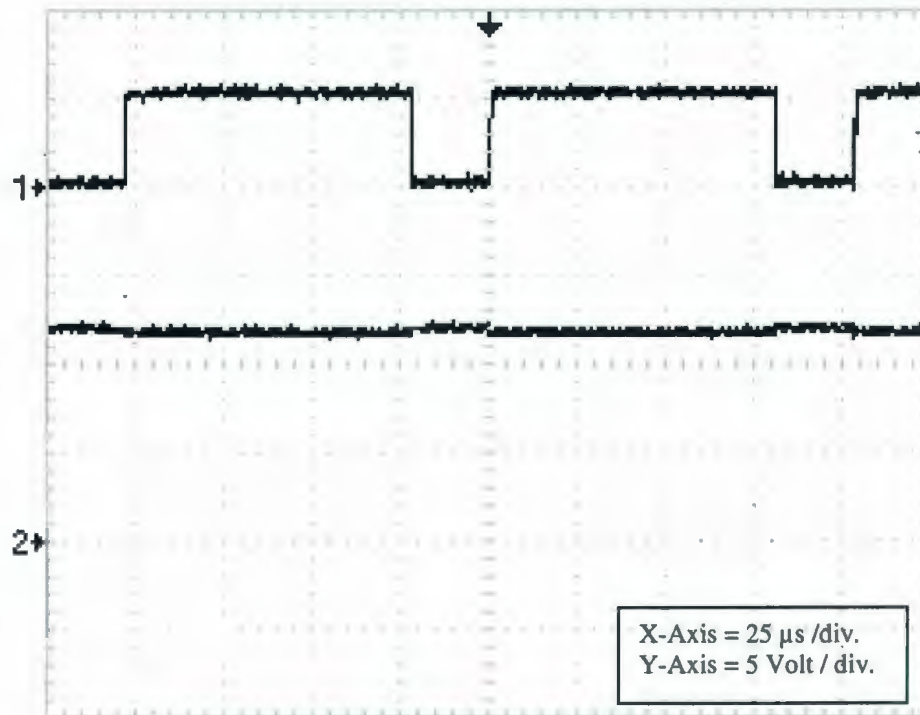
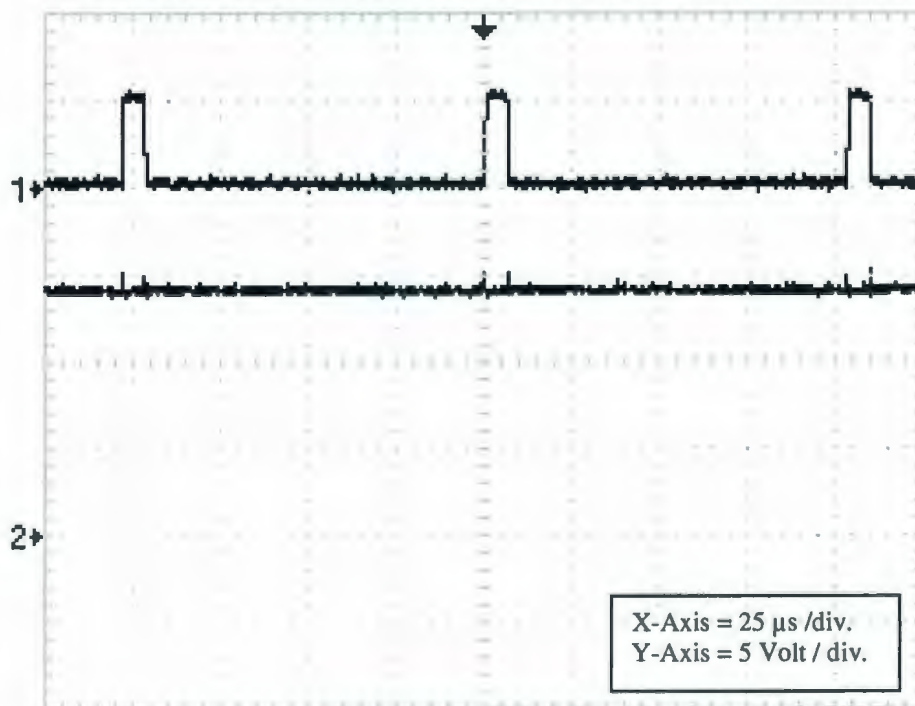
sense up to 20Volt based on selecting the values of R1 and R2. However, the resistor values should be selected such that the maximum sensing voltage $V_M \leq 5V$. Furthermore, an on chip 10 bit ADC converter is used by 16F877A microcontrollers has quantization steps determined as:

$$\text{Quantization steps} = \frac{5}{1023} \approx 49\text{mV}$$

Among the eight available channels (RA0-RA7 in 16F877A, in case of a 40 pin devices), any can be used to sense the voltage using the on chip ADC. The voltage read through these channels is multiplied by 4 due to the fact that the actual voltage is four times the sensed voltage.

6.5 Test Results

The developed MPPT is tested by observing the duty ratio with the changes in power fed to the conversion circuit by the input dc power supply. The converter output is moved to the MPP point as soon as it reached the reference voltage. Also, changes in duty cycle affect both the output current and the output voltage of the dc-dc boost converter. While the operating voltage is below the reference level (14V), the duty ratio starts increasing to a maximum value. When the operating voltage starts getting higher than the reference voltage, then the duty ratio decreases until it comes to a minimum value and brings the operating voltage to its reference level. The decreasing duty ratio ensures that the available maximum power is transferred to the load by increasing the current while maintaining the reference voltage at the converter output side. This experimental results are shown in Figure 6.13(a) and 6.13(b), where channel-1 shows the PWM signal and channel-2 shows the output voltage.

Figure 6.13 (a) Maximum duty ratio for $V_{out} < V_{ref}$ Figure 6.13 (b) Minimum duty ratio for $V_{out} \geq V_{ref}$

When the operating voltage is below the reference level, the duty ratio starts increasing to its maximum value. It ensures that the boost converter maintains the reference voltage at its output. This is shown in Figure 6.14.

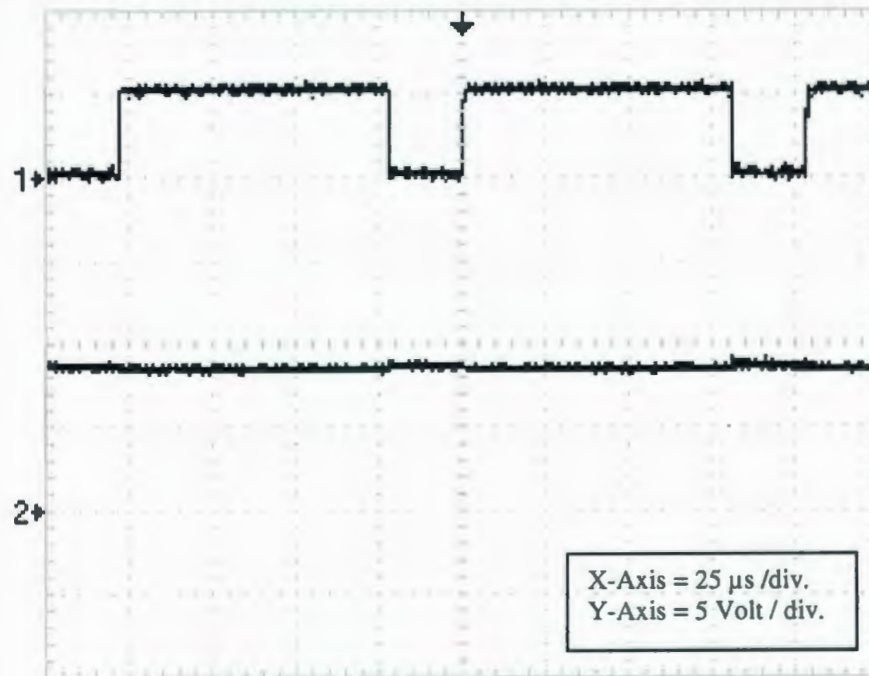


Figure 6.14 Maximum duty ratio for $V_{out} < V_{ref}$

6.6 Conclusion

A simple, low cost PIC microcontroller system, comprising an over speed protection, has been proposed. This control system has been developed, and discussed with its experimental test results. Also, maximum available power has been tracked and delivered to the load by using a MPPT-based control. The developed control system can easily extended with minimum requirement of electronic devices for further control.

CHAPTER 7

CONCLUSIONS

7.0 Research Conclusion

The research conducted in this work has been focused on mitigating the practical challenges associated with the low speed marine currents in the North Atlantic region. Throughout this research time frame, several literature reviews have been done on existing marine current turbines as well as associated control systems. The general observation of existing marine current turbines is their high cost and applicability only. In

order to overcome such challenges, a combination of two existing designs (the Savonius and Darrieus turbine) has been considered for designing a hybrid turbine.

The designed hybrid turbine has been built at the Machine shop of Memorial University of Newfoundland (MUN), Canada. Almost every part of the turbine has been built at the university, but some parts were bought from the manufacturers. Moreover, the designed turbine has been tested at the Flume Tank with high accuracy of water flow. The test results have been analyzed and a solution was found for a low cut-in speed turbine needed for implementing the MECS.

Several control schemes for wind turbines have been studied and a control scheme known as perturbation and observation MPPT algorithm has been selected, built and tested at the Instrumentation, Control and Automation (INCA) lab of MUN. The designed control has been implemented on a low cost microcontroller (PIC16F877A). Furthermore, a dc-dc boost converter has been designed to facilitate charging a battery. The circuit has been tested to ensure that the maximum available power is transferred to the load. Though some problems were faced regarding the current sensor, an RC filter mitigated the problem. In summary, a successful marine energy conversion system has been designed and tested with all its associated components.

7.1 Thesis Contribution

To summarize the thesis contribution during this research work, the following can be highlighted:

- A complete marine current energy conversion system has been built, tested and analyzed.

- A simple, low cut-in speed, high Tip Speed Ratio (TSR), lift type hybrid vertical axis turbine has been designed and analyzed.
- The designed turbine has been tested in a real world situation and the test results are compared with the design.
- A low cost PIC microcontroller based control system has been designed, built and tested to ensure maximum power transfer.

7.2 Future Work & Suggestions

As the research work has taken into account for the power requirements of Seaformatics pods, to be developed by 2011, some future work can be done to spur the scope of the research and to upgrade the designed energy conversion system.

- More water current data should be collected where the proposed system will be installed around St. John's.
- Before the actual turbine design and tests, a Computational Fluid Dynamic (CFD) analysis should be done. The CFD will assist to virtually understand the effect of the lift and drag forces produced by the turbine for different speed of fluid flow, which is also related to the Reynolds Number.
- To get a higher torque at a comparatively low TSR of the designed turbine, cambered airfoils should also be considered.
- A low speed DC permanent magnet generator can be used to avoid gearbox and rectifier losses.
- The MOSFET switching needs more research, because it has competitive advantages of both soft and hard switching. As the peak to peak inductor current

is inversely proportional to the switching frequency, this should be taken into consideration during the switching frequency selection.

- A more sophisticated MPPT algorithm can also be implemented.
- Digital filters can be introduced to reduce the number of components in the control circuit.

Bibliography

- [1] A.S. Bahaj, L.E. Myers “Fundamentals applicable to the utilisation of marine current turbines for energy production” *Renewable Energy* Vol. 28 (2003), pp. 2205–2211
- [2] Technical Report, April 2006, on “Inventory of Canada’s Marine Renewable Energy Resources” by A. Cornett, Canadian Hydraulics Centre, National Research Council, Canada
- [3] Ayan H. Chaudhuri, Avijit Gangopadhyay, James J. Bisagni, “Interannual variability of Gulf Stream warm-core rings in response to the North Atlantic Oscillation”, *Continental Shelf Research* 29 (2009), pp. 856–869
- [4] Barbie Bischof, Arthur J. Mariano, Edward H. Ryan (2003) “The North Atlantic Drift Current”. <http://oceancurrents.rsmas.miami.edu/atlantic/north-atlantic-drift.html>
- [5] Bacon, S., 1997: Circulation and Fluxes in the North Atlantic between Greenland and Ireland, *Journal of Oceanography*, Vol. 27, pp.1420-1435
- [6] Elizabeth Rowe, Arthur J. Mariano, Edward H. Ryan. "The North Atlantic Current." <http://oceancurrents.rsmas.miami.edu/atlantic/north-atlantic.html>
- [7] Md. Nahidul Islam Khan, M. T. Iqbal, M. Hinchey, Sea-Floor Power Generation System, presented at 17th IEEE NECEC conference, November 8, 2007, St. John s, NL
- [8] M.J.Khan, M.T.Iqbal, J.E.Quaicoe, “A technology review and simulation based performance analysis of river current turbine systems”, presented at CCECE, Ottawa, May 2006. ISBN: 1- 4244 -0038-4 2006, pp.2288-2293
- [9] “Ocean Renewable Energy in Canada” by Ocean Renewable Energy Group. www.oreg.ca

- [10] Robin Pelc, Rod M.Fujita "Renewable energy from the ocean" *Marine Policy*, Vol. 26 (2002), pp. 471–479
- [11] "A Scoping Study for an Environmental Impact Field Programme in tidal current energy", by Centre for Environmental Engineering and Sustainable Energy, The Robert Gordon University, UK, ETSU T/04/00213/REP, 2002
- [12] Md. Nahidul Islam Khan, M. T. Iqbal, M. Hinchey, "Sea-Floor Power Generation System", presented at 17th IEEE NECEC conference, St. Johns, NL, November 8, 2007
- [13] J.-L. Menet, "A double-step Savonius rotor for local production of electricity: a design study" *Renewable Energy* vol.19 September 2004, page 1843-1862, Science Direct
- [14] D.P Cairo , U. Maisto, F. Scherillo, S.Melone,F. Grasso, "Horizontal Axis Tidal Current Turbine" *Owemes* 2006, 20-22 April. Civitavecchia, Italy
- [15] Manohar K, Rampartap, Ramkissoon R, "Self starting Hybrid 'H' type wind turbine" *Energy Sustainability* 2007, Long Beach, California, June 27-30
- [16] Wakui T, Tanzawa Y, Hashizume T, Nagao T, "Hybrid configuration of Darrieus and Savonius rotors for stand-alone wind turbine-generator systems" *Electrical Engineering in Japan*, Vol.150, No.4, 2005
- [17] Miley, S.J. "Catalog of low-Reynolds-number airfoil data for wind turbine applications", Technical Report, 1982 Feb 01, RFP-3387
- [18] Godfrey Boyle, *Renewable Energy: power for sustainable future*, Oxford university press 2004
- [19] B. Kirke, L. Lazauskas, "Variable Pitch Darrieus Water Turbines", *Journal of Fluid Science and Technology*, Vol.3, 2008, pp. 430-438

- [20] L.H Hansen, L.Helle, F.Blaabjerg, E.Ritchie, S. Munk-Nielsen, H.Bindner, P.Sorensen and B.Bak-Jensen "Conceptual Survey of Generators and Power Electronics for Wind Turbines", Riso National Laboratory, Denmark, December 2001, ISBN 87-550-2745-8 (Internet)
- [21] A. P. Ferreira¹, A. M. Silva, A. F. Costa "Prototype of an Axial Flux Permanent Magnet Generator for Wind Energy Systems Applications" European Conference on Power Electronics and Applications, 2-5 Sept. 2007, ISBN: 978-92-75815-10-8, pp. 1-9
- [22] Andrew S. Holmes, Guodong Hong, and Keith R. Pullen "Axial-Flux Permanent Magnet Machines for Micropower Generation" Journal of Microelectromechanical Systems, Vol.14, No.1, February 2005, pp.54-62
- [23] Garrison F. Price, Todd D. Batzel, Mihai Comanescu, and Bruce A. Muller "Design and Testing of a Permanent Magnet Axial Flux Wind Power Generator" Proceedings of The 2008 IAJC-IJME International Conference, ISBN 978-1-60643-379-9
- [24] D. P. Arnold¹, I. Zana¹, F. Herrault, P. Galle, J.-W. Park, S. Das, J. H. Lang, and M. G. Allen, "Optimization of a Microscale, Axial-Flux, Permanent-Magnet Generator" Technical Report, Georgia Institute of Technology, School of Electrical and Computer Engineering, 2005
- [25] Sanjida Moury, M. Tariq Iqbal, " A new approach to minimize the cogging torque of axial flux PMG for under water applications" 22nd CCECE'09, St.John's, NL, Canada, 03-06 May, 2009. ISBN: 978-1-4244-3508-1, pp.1167-1171
- [26] E. Muljadi and J. Green, "Cogging Torque Reduction in a Permanent Magnet Wind Turbine Generator", 21st American Society of Mechanical Engineers Wind Energy Symposium Reno, Nevada, January 14-17, 2002, NREL/CP-500-30768

- [27] Hui Li, Danwei Liu and Cesar A. Luongo, "Investigation of Potential Benefits of MOSFETS Hard-Switching and Soft-Switching Converters at Cryogenic Temperature" IEEE Transactions on Applied Superconductivity , Vol.15 , No.2, June 2005, pp.2376-2380
- [28] L.L.Freris, "Wind Energy Conversion Systems", Englewood Cliffs, NJ: Prentice-Hall, 1990, pp.182-184
- [29] Eftichios Koutroulis and Kostas Kalaitzakis, "Design of a Maximum Power Point Tracking System for Wind-Energy- Conversion Applications" IEEE Transactions on industrial Electronics Vol.53,No.2, April 2006, pp.484-494
- [30] A.M.De Broe, S. Drouilhet and V. Gevorgian, "A Peak Power Tracker for small wind Turbine in battery charging Applications", IEEE Transaction of Energy Conversion., Vol.5, no.4, pp. Dec.1999, pp.1630-1635
- [31] D. Sera, T. Kerekes, R.Teodorescu, F.Blaabjerg, "Improved MPPT Algorithms for Rapidly Changing Environmental Conditions", Power Electronics and Motion Control Conference, 2006. EPE-PEMC 2006,12th International, ISBN: 1-4244-0121-6, pp. 1614-1619
- [32] A. Yafaoui., B. Wu and R. Cheung, " Implementation of maximum power point tracking algorithm for residential Photovoltaic systems" 2nd Canadian Solar Buildings Conference, Calgary, June 10 – 14, 2007

Appendix A

A.1

▪ Power (P) vs. Water Speed (V) for Savonius Turbine

```
V = [0.1 0.2 0.3 0.4 0.5 0.6 0.7 0.8 0.9 1]
P = [0 0 0 0.1365 0.2669 0.4612 0.7323 1.093 1.556 2.13]
plot(V,P),grid
xlabel('Water Speed,V (m/s)')
ylabel('Power output,P (W)')
```

A.2

▪ Power (P) vs. Water Speed (V) for H-Darrieus Turbine (+ Data Processing)

```
clc
% Water Speed=0.2m/s

ws21=load('d21.txt');
ws21(:,[1 2 4])=[];
t21=(mean(ws21(:,1))/1000)*9.8*0.15; %Torque
w21=mean(ws21(:,2))*((2*pi)/60); % Speed in Radian/S
p21=t21*w21;
Pmax2=p21

% Water Speed=0.3m/s

ws31=load('d31.txt');
ws31(:,[1 2 4])=[];
t31=(mean(ws31(:,1))/1000)*9.8*0.15;
w31=mean(ws31(:,2))*((2*pi)/60);
p31=t31*w31;

ws32=load('d32.txt');
ws32(:,[1 2 4])=[];
t32=(mean(ws32(:,1))/1000)*9.8*0.15;
w32=mean(ws32(:,2))*((2*pi)/60);
p32=t32*w32;

ws33=load('d33.txt');
ws33(:,[1 2 4])=[];
t33=(mean(ws33(:,1))/1000)*9.8*0.15;
```

```
w33=mean(ws33(:,2))*((2*pi)/60);
p33=t33*w33;
```

```
ws34=load('d34.txt');
ws34(:,[1 2 4])=[];
t34=(mean(ws34(:,1))/1000)*9.8*0.15;
w34=mean(ws34(:,2))*((2*pi)/60);
p34=t34*w34;
```

```
ws35=load('d35.txt');
ws35(:,[1 2 4])=[];
t35=(mean(ws35(:,1))/1000)*9.8*0.15;
w35=mean(ws35(:,2))*((2*pi)/60);
p35=t35*w35;
```

```
ws36=load('d36.txt');
ws36(:,[1 2 4])=[];
t36=(mean(ws36(:,1))/1000)*9.8*0.15;
w36=mean(ws36(:,2))*((2*pi)/60);
p36=t36*w36;
```

```
t3=[t31 t32 t33 t34 t35 t36]
w3=[w31 w32 w33 w34 w35 w36]
p3=[p31 p32 p33 p34 p35 p36]
Pmax3=max(p3)
```

% Water Speed=0.4m/s

```
ws41=load('d41.txt');
ws41(:,[1 2 4])=[];
t41=(mean(ws41(:,1))/1000)*9.8*0.15;
w41=mean(ws41(:,2))*((2*pi)/60);
p41=t41*w41;
```

```
ws42=load('d42.txt');
ws42(:,[1 2 4])=[];
t42=(mean(ws42(:,1))/1000)*9.8*0.15;
w42=mean(ws42(:,2))*((2*pi)/60);
p42=t42*w42;
```

```
ws43=load('d43.txt');
ws43(:,[1 2 4])=[];
t43=(mean(ws43(:,1))/1000)*9.8*0.15;
w43=mean(ws43(:,2))*((2*pi)/60);
p43=t43*w43;
```

```

ws44=load('d44.txt');
ws44(:,[1 2 4])=[];
t44=(mean(ws44(:,1))/1000)*9.8*0.15;
w44=mean(ws44(:,2))*((2*pi)/60);
p44=t44*w44;

```

```

ws45=load('d45.txt');
ws45(:,[1 2 4])=[];
t45=(mean(ws45(:,1))/1000)*9.8*0.15;
w45=mean(ws45(:,2))*((2*pi)/60);
p45=t45*w45;

```

```

ws46=load('d46.txt');
ws46(:,[1 2 4])=[];
t46=(mean(ws46(:,1))/1000)*9.8*0.15;
w46=mean(ws46(:,2))*((2*pi)/60);
p46=t46*w46;

```

```

ws47=load('d47.txt');
ws47(:,[1 2 4])=[];
t47=(mean(ws47(:,1))/1000)*9.8*0.15;
w47=mean(ws47(:,2))*((2*pi)/60);
p47=t47*w47;

```

```

t4=[t41 t42 t43 t44 t45 t46 t47]
w4=[w41 w42 w43 w44 w45 w46 w47]
p4=[p41 p42 p43 p44 p45 p46 p47]

```

```

Pmax4=max(p4)

```

```

% Water Speed=0.5m/s

```

```

ws51=load('d51.txt');
ws51(:,[1 2 4])=[];
t51=(mean(ws51(:,1))/1000)*9.8*0.15;
w51=mean(ws51(:,2))*((2*pi)/60);
p51=t51*w51;

```

```

ws52=load('d52.txt');
ws52(:,[1 2 4])=[];
t52=(mean(ws52(:,1))/1000)*9.8*0.15;
w52=mean(ws52(:,2))*((2*pi)/60);
p52=t52*w52;

```

```
ws53=load('d53.txt');
ws53(:,[1 2 4])=[];
t53=(mean(ws53(:,1))/1000)*9.8*0.15;
w53=mean(ws53(:,2))*((2*pi)/60);
p53=t53*w53;

ws54=load('d54.txt');
ws54(:,[1 2 4])=[];
t54=(mean(ws54(:,1))/1000)*9.8*0.15;
w54=mean(ws54(:,2))*((2*pi)/60);
p54=t54*w54;

ws55=load('d55.txt');
ws55(:,[1 2 4])=[];
t55=(mean(ws55(:,1))/1000)*9.8*0.15;
w55=mean(ws55(:,2))*((2*pi)/60);
p55=t55*w55;

ws56=load('d56.txt');
ws56(:,[1 2 4])=[];
t56=(mean(ws56(:,1))/1000)*9.8*0.15;
w56=mean(ws56(:,2))*((2*pi)/60);
p56=t56*w56;

ws57=load('d57.txt');
ws57(:,[1 2 4])=[];
t57=(mean(ws57(:,1))/1000)*9.8*0.15;
w57=mean(ws57(:,2))*((2*pi)/60);
p57=t57*w57;

ws58=load('d58.txt');
ws58(:,[1 2 4])=[];
t58=(mean(ws58(:,1))/1000)*9.8*0.15;
w58=mean(ws58(:,2))*((2*pi)/60);
p58=t58*w58;

ws59=load('d59.txt');
ws59(:,[1 2 4])=[];
t59=(mean(ws59(:,1))/1000)*9.8*0.15;
w59=mean(ws59(:,2))*((2*pi)/60);
p59=t59*w59;

ws510=load('d510.txt');
ws510(:,[1 2 4])=[];
t510=(mean(ws510(:,1))/1000)*9.8*0.15;
w510=mean(ws510(:,2))*((2*pi)/60);
```

```
p510=t510*w510;
```

```
t5=[t51 t52 t53 t54 t55 t56 t57 t58 t59 t510]
w5=[w51 w52 w53 w54 w55 w56 w57 w58 w59 w510]
p5=[p51 p52 p53 p54 p55 p56 p57 p58 p59 p510]
```

```
Pmax5=max(p5)
```

```
% Water Speed=0.6m/s
```

```
ws61=load('d61.txt');
ws61(:,[1 2 4])=[];
t61=(mean(ws61(:,1))/1000)*9.8*0.15;
w61=mean(ws61(:,2))*((2*pi)/60);
p61=t61*w61;
```

```
ws62=load('d62.txt');
ws62(:,[1 2 4])=[];
t62=(mean(ws62(:,1))/1000)*9.8*0.15;
w62=mean(ws62(:,2))*((2*pi)/60);
p62=t62*w62;
```

```
ws63=load('d63.txt');
ws63(:,[1 2 4])=[];
t63=(mean(ws63(:,1))/1000)*9.8*0.15;
w63=mean(ws63(:,2))*((2*pi)/60);
p63=t63*w63;
```

```
ws64=load('d64.txt');
ws64(:,[1 2 4])=[];
t64=(mean(ws64(:,1))/1000)*9.8*0.15;
w64=mean(ws64(:,2))*((2*pi)/60);
p64=t64*w64;
```

```
ws65=load('d65.txt');
ws65(:,[1 2 4])=[];
t65=(mean(ws65(:,1))/1000)*9.8*0.15;
w65=mean(ws65(:,2))*((2*pi)/60);
p65=t65*w65;
```

```
ws66=load('d66.txt');
ws66(:,[1 2 4])=[];
t66=(mean(ws66(:,1))/1000)*9.8*0.15;
w66=mean(ws66(:,2))*((2*pi)/60);
p66=t66*w66;
```

```

ws67=load('d67.txt');
ws67(:,[1 2 4])=[];
t67=(mean(ws67(:,1))/1000)*9.8*0.15;
w67=mean(ws67(:,2))*((2*pi)/60);
p67=t67*w67;

ws68=load('d68.txt');
ws68(:,[1 2 4])=[];
t68=(mean(ws68(:,1))/1000)*9.8*0.15;
w68=mean(ws68(:,2))*((2*pi)/60);
p68=t68*w68;

ws69=load('d69.txt');
ws69(:,[1 2 4])=[];
t69=(mean(ws69(:,1))/1000)*9.8*0.15;
w69=mean(ws69(:,2))*((2*pi)/60);
p69=t69*w69;

t6=[t61 t62 t63 t64 t65 t66 t67 t68 t69]
w6=[w61 w62 w63 w64 w65 w66 w67 w68 w69]
p6=[p61 p62 p63 p64 p65 p66 p67 p68 p69]

Pmax6=max(p6)

P=[0 0 Pmax2 Pmax3 Pmax4 Pmax5 Pmax6]
V=[0 0.1 0.2 0.3 0.4 0.5 0.6]

plot(V,P), grid on
%title('Power vs. Water Speed for Darrieus Turbine')
xlabel('Water Speed, V (m/s)')
ylabel('Power output, P (Watt)')

```

A.3

▪ C_{pd} vs. TSR (λ_d) for H-Darrieus Turbine

```

%0.3 m/s
p3=(0.5*1000*1*(0.3)^3);
w3=[1.5300 1.6229 1.7334];
lamda3=(w3*0.5)/0.3;
pt3=[0.7027 0.7297 0.2995];
cp3=pt3./p3;
tsr3max=max(lamda3);
tsr3min=min(lamda3);
cp33max=max(cp3)

```

```
cp33min=min(cp3);
```

```
%0.4 m/s
```

```
p4=(0.5*1000*1*(0.4)^3);
w4=[2.2139 2.3001 2.3731 2.4167 2.4548 2.4710];
lamda4=(w4*0.5)/0.4
pt4=[3.1171 2.4407 1.8591 1.1738 0.6439 0.3789];
cp4=pt4./p4
tsr4max=max(lamda4)
tsr4min=min(lamda4);
cp44max=max(cp4)
cp44min=min(cp4);
```

```
%0.5 m/s
```

```
p5=(0.5*1000*1*(0.5)^3);
w5=[2.7668 2.8224 2.8470 2.9002 2.9373 2.9716 2.9853 2.9993];
lamda5=(w5*0.5)/0.5;
pt5=[5.9550 5.2118 3.8698 2.6856 1.9973 1.5744 1.0349 0.8780];
cp5=pt5./p5;
tsr5max=max(lamda5)
tsr5min=min(lamda5);
cp55max=max(cp5)
cp55min=min(cp5);
```

```
% 0.6 m/s
```

```
p6=(0.5*1000*1*(0.6)^3);
w6=[2.4446 3.1985 3.2669 3.4255 3.4879 3.4791 3.5910 3.5363 3.5180];
lamda6=(w6*0.5)/0.6
pt6=[9.8113 13.4786 10.9878 9.1785 6.3008 4.1407 3.0462 2.5259 2.3988];
cp6=pt6./p6
tsr6max=max(lamda6)
tsr6min=min(lamda6);
cp66max=max(cp6)
cp66min=min(cp6);
```

```
TSR=[lamda3,lamda4,lamda5,lamda6];
```

```
Cp=[cp3,cp4,cp5,cp6];
```

```
MaximumTSR=max(TSR)
```

```
MinimumTSR=min(TSR);
```

```
MaximumCp=max(Cp)
```

```
MinimumCp=min(Cp);
```

```
plot(lamda3,cp3,lamda4,cp4,lamda5,cp5,lamda6,cp6),grid
```

```
xlabel('TSR')
```

```
ylabel('Power Coefficient(Cp)')
```

Appendix B

B.1

- **Power Comparison for Savonius, H-Darrieus and Hybrid Turbine(+ Data Processing)**

% Data Processing

clc

% Water Speed=0.2m/s

ws21=load('h21.txt');

ws21(:,[1 2 4])=[];

t21=(mean(ws21(:,1))/1000)*9.8*0.15; %Torque

w21=mean(ws21(:,2))*((2*pi)/60); % Speed in Radian/S

p21=t21*w21;

Pmax2=p21

% Water Speed=0.3m/s

ws31=load('h31.txt');

ws31(:,[1 2 4])=[];

t31=(mean(ws31(:,1))/1000)*9.8*0.15;

w31=mean(ws31(:,2))*((2*pi)/60);

p31=t31*w31;

ws32=load('h32.txt');

ws32(:,[1 2 4])=[];

t32=(mean(ws32(:,1))/1000)*9.8*0.15;

w32=mean(ws32(:,2))*((2*pi)/60);

p32=t32*w32;

ws33=load('h33.txt');

ws33(:,[1 2 4])=[];

t33=(mean(ws33(:,1))/1000)*9.8*0.15;

w33=mean(ws33(:,2))*((2*pi)/60);

p33=t33*w33;

ws34=load('h34.txt');

ws34(:,[1 2 4])=[];

t34=(mean(ws34(:,1))/1000)*9.8*0.15;

w34=mean(ws34(:,2))*((2*pi)/60);

```

p34=t34*w34;

ws35=load('h35.txt');
ws35(:,[1 2 4])=[];
t35=(mean(ws35(:,1))/1000)*9.8*0.15;
w35=mean(ws35(:,2))*((2*pi)/60);
p35=t35*w35;

t3=[t31 t32 t33 t34 t35]
w3=[w31 w32 w33 w34 w35]
p3=[p31 p32 p33 p34 p35]
Pmax3=max(p3)

% Water Speed=0.4m/s

ws41=load('h41.txt');
ws41(:,[1 2 4])=[];
t41=(mean(ws41(:,1))/1000)*9.8*0.15;
w41=mean(ws41(:,2))*((2*pi)/60);
p41=t41*w41;

ws42=load('h42.txt');
ws42(:,[1 2 4])=[];
t42=(mean(ws42(:,1))/1000)*9.8*0.15;
w42=mean(ws42(:,2))*((2*pi)/60);
p42=t42*w42;

ws43=load('h43.txt');
ws43(:,[1 2 4])=[];
t43=(mean(ws43(:,1))/1000)*9.8*0.15;
w43=mean(ws43(:,2))*((2*pi)/60);
p43=t43*w43;

ws44=load('h44.txt');
ws44(:,[1 2 4])=[];
t44=(mean(ws44(:,1))/1000)*9.8*0.15;
w44=mean(ws44(:,2))*((2*pi)/60);
p44=t44*w44;

ws45=load('h45.txt');
ws45(:,[1 2 4])=[];
t45=(mean(ws45(:,1))/1000)*9.8*0.15;
w45=mean(ws45(:,2))*((2*pi)/60);
p45=t45*w45;

t4=[t41 t42 t43 t44 t45]

```

```
w4=[w41 w42 w43 w44 w45]
p4=[p41 p42 p43 p44 p45]
Pmax4=max(p4)
```

```
% Water Speed=0.5m/s
```

```
ws51=load('h51.txt');
ws51(:,[1 2 4])=[];
t51=(mean(ws51(:,1))/1000)*9.8*0.15;
w51=mean(ws51(:,2))*((2*pi)/60);
p51=t51*w51;
```

```
ws52=load('h52.txt');
ws52(:,[1 2 4])=[];
t52=(mean(ws52(:,1))/1000)*9.8*0.15;
w52=mean(ws52(:,2))*((2*pi)/60);
p52=t52*w52;
```

```
ws53=load('h53.txt');
ws53(:,[1 2 4])=[];
t53=(mean(ws53(:,1))/1000)*9.8*0.15;
w53=mean(ws53(:,2))*((2*pi)/60);
p53=t53*w53;
```

```
ws54=load('h54.txt');
ws54(:,[1 2 4])=[];
t54=(mean(ws54(:,1))/1000)*9.8*0.15;
w54=mean(ws54(:,2))*((2*pi)/60);
p54=t54*w54;
```

```
ws55=load('h55.txt');
ws55(:,[1 2 4])=[];
t55=(mean(ws55(:,1))/1000)*9.8*0.15;
w55=mean(ws55(:,2))*((2*pi)/60);
p55=t55*w55;
```

```
ws56=load('h56.txt');
ws56(:,[1 2 4])=[];
t56=(mean(ws56(:,1))/1000)*9.8*0.15;
w56=mean(ws56(:,2))*((2*pi)/60);
p56=t56*w56;
```

```
ws57=load('h57.txt');
ws57(:,[1 2 4])=[];
t57=(mean(ws57(:,1))/1000)*9.8*0.15;
w57=mean(ws57(:,2))*((2*pi)/60);
```

```
p57=t57*w57;
```

```
ws58=load('h58.txt');
ws58(:,[1 2 4])=[];
t58=(mean(ws58(:,1))/1000)*9.8*0.15;
w58=mean(ws58(:,2))*((2*pi)/60);
p58=t58*w58;
```

```
ws59=load('h59.txt');
ws59(:,[1 2 4])=[];
t59=(mean(ws59(:,1))/1000)*9.8*0.15;
w59=mean(ws59(:,2))*((2*pi)/60);
p59=t59*w59;
```

```
t5=[t51 t52 t53 t54 t55 t56 t57 t58 t59]
w5=[w51 w52 w53 w54 w55 w56 w57 w58 w59]
p5=[p51 p52 p53 p54 p55 p56 p57 p58 p59]
```

```
Pmax5=max(p5)
```

```
% Water Speed=0.6m/s
```

```
ws61=load('h61.txt');
ws61(:,[1 2 4])=[];
t61=(mean(ws61(:,1))/1000)*9.8*0.15;
w61=mean(ws61(:,2))*((2*pi)/60);
p61=t61*w61;
```

```
ws62=load('h62.txt');
ws62(:,[1 2 4])=[];
t62=(mean(ws62(:,1))/1000)*9.8*0.15;
w62=mean(ws62(:,2))*((2*pi)/60);
p62=t62*w62;
```

```
ws63=load('h63.txt');
ws63(:,[1 2 4])=[];
t63=(mean(ws63(:,1))/1000)*9.8*0.15;
w63=mean(ws63(:,2))*((2*pi)/60);
p63=t63*w63;
```

```
ws64=load('h64.txt');
ws64(:,[1 2 4])=[];
t64=(mean(ws64(:,1))/1000)*9.8*0.15;
w64=mean(ws64(:,2))*((2*pi)/60);
```

```

p64=t64*w64;

ws65=load('h65.txt');
ws65(:,[1 2 4])=[];
t65=(mean(ws65(:,1))/1000)*9.8*0.15;
w65=mean(ws65(:,2))*((2*pi)/60);
p65=t65*w65;

ws66=load('h66.txt');
ws66(:,[1 2 4])=[];
t66=(mean(ws66(:,1))/1000)*9.8*0.15;
w66=mean(ws66(:,2))*((2*pi)/60);
p66=t66*w66;

ws67=load('h67.txt');
ws67(:,[1 2 4])=[];
t67=(mean(ws67(:,1))/1000)*9.8*0.15;
w67=mean(ws67(:,2))*((2*pi)/60);
p67=t67*w67;

ws68=load('h68.txt');
ws68(:,[1 2 4])=[];
t68=(mean(ws68(:,1))/1000)*9.8*0.15;
w68=mean(ws68(:,2))*((2*pi)/60);
p68=t68*w68;

ws69=load('h69.txt');
ws69(:,[1 2 4])=[];
t69=(mean(ws69(:,1))/1000)*9.8*0.15;
w69=mean(ws69(:,2))*((2*pi)/60);
p69=t69*w69;

t6=[t61 t62 t63 t64 t65 t66 t67 t68 t69]
w6=[w61 w62 w63 w64 w65 w66 w67 w68 w69]
p6=[p61 p62 p63 p64 p65 p66 p67 p68 p69]

Pmax6=max(p6)

% Water Speed=0.7m/s

ws71=load('h71.txt');
ws71(:,[1 2 4])=[];
t71=(mean(ws71(:,1))/1000)*9.8*0.15;
w71=mean(ws71(:,2))*((2*pi)/60);
p71=t71*w71;

```

```
ws72=load('h72.txt');  
ws72(:,[1 2 4])=[];  
t72=(mean(ws72(:,1))/1000)*9.8*0.15;  
w72=mean(ws72(:,2))*((2*pi)/60);  
p72=t72*w72;
```

```
ws73=load('h73.txt');  
ws73(:,[1 2 4])=[];  
t73=(mean(ws73(:,1))/1000)*9.8*0.15;  
w73=mean(ws73(:,2))*((2*pi)/60);  
p73=t73*w73;
```

```
ws74=load('h74.txt');  
ws74(:,[1 2 4])=[];  
t74=(mean(ws74(:,1))/1000)*9.8*0.15;  
w74=mean(ws74(:,2))*((2*pi)/60);  
p74=t74*w74;
```

```
ws75=load('h75.txt');  
ws75(:,[1 2 4])=[];  
t75=(mean(ws75(:,1))/1000)*9.8*0.15;  
w75=mean(ws75(:,2))*((2*pi)/60);  
p75=t75*w75;
```

```
ws76=load('h76.txt');  
ws76(:,[1 2 4])=[];  
t76=(mean(ws76(:,1))/1000)*9.8*0.15;  
w76=mean(ws76(:,2))*((2*pi)/60);  
p76=t76*w76;
```

```
ws77=load('h77.txt');  
ws77(:,[1 2 4])=[];  
t77=(mean(ws77(:,1))/1000)*9.8*0.15;  
w77=mean(ws77(:,2))*((2*pi)/60);  
p77=t77*w77;
```

```
ws78=load('h78.txt');  
ws78(:,[1 2 4])=[];  
t78=(mean(ws78(:,1))/1000)*9.8*0.15;  
w78=mean(ws78(:,2))*((2*pi)/60);  
p78=t78*w78;
```

```
ws79=load('h79.txt');  
ws79(:,[1 2 4])=[];  
t79=(mean(ws79(:,1))/1000)*9.8*0.15;  
w79=mean(ws79(:,2))*((2*pi)/60);
```

```
p79=t79*w79;
```

```
ws710=load('h710.txt');
ws710(:,[1 2 4])=[];
t710=(mean(ws710(:,1))/1000)*9.8*0.15;
w710=mean(ws710(:,2))*((2*pi)/60);
p710=t710*w710;
```

```
t7=[t71 t72 t73 t74 t75 t76 t77 t78 t79 t710]
w7=[w71 w72 w73 w74 w75 w76 w77 w78 w79 w710]
p7=[p71 p72 p73 p74 p75 p76 p77 p78 p79 p710]
```

```
Pmax7=max(p7)
```

```
% Water Speed=0.8m/s
```

```
ws81=load('h81.txt');
ws81(:,[1 2 4])=[];
t81=(mean(ws81(:,1))/1000)*9.8*0.15;
w81=mean(ws81(:,2))*((2*pi)/60);
p81=t81*w81;
```

```
ws82=load('h82.txt');
ws82(:,[1 2 4])=[];
t82=(mean(ws82(:,1))/1000)*9.8*0.15;
w82=mean(ws82(:,2))*((2*pi)/60);
p82=t82*w82;
```

```
ws83=load('h83.txt');
ws83(:,[1 2 4])=[];
t83=(mean(ws83(:,1))/1000)*9.8*0.15;
w83=mean(ws83(:,2))*((2*pi)/60);
p83=t83*w83;
```

```
ws84=load('h84.txt');
ws84(:,[1 2 4])=[];
t84=(mean(ws84(:,1))/1000)*9.8*0.15;
w84=mean(ws84(:,2))*((2*pi)/60);
p84=t84*w84;
```

```
ws85=load('h85.txt');
ws85(:,[1 2 4])=[];
t85=(mean(ws85(:,1))/1000)*9.8*0.15;
w85=mean(ws85(:,2))*((2*pi)/60);
p85=t85*w85;
```

```

ws86=load('h86.txt');
ws86(:,[1 2 4])=[];
t86=(mean(ws86(:,1))/1000)*9.8*0.15;
w86=mean(ws86(:,2))*((2*pi)/60);
p86=t86*w86;

ws87=load('h87.txt');
ws87(:,[1 2 4])=[];
t87=(mean(ws87(:,1))/1000)*9.8*0.15;
w87=mean(ws87(:,2))*((2*pi)/60);
p87=t87*w87;

ws88=load('h88.txt');
ws88(:,[1 2 4])=[];
t88=(mean(ws88(:,1))/1000)*9.8*0.15;
w88=mean(ws88(:,2))*((2*pi)/60);
p88=t88*w88;

ws89=load('h89.txt');
ws89(:,[1 2 4])=[];
t89=(mean(ws89(:,1))/1000)*9.8*0.15;
w89=mean(ws89(:,2))*((2*pi)/60);
p89=t89*w89;

t8=[t81 t82 t83 t84 t85 t86 t87 t88 t89]
w8=[w81 w82 w83 w84 w85 w86 w87 w88 w89]
p8=[p81 p82 p83 p84 p85 p86 p87 p88 p89]

Pmax8=max(p8)

P=[0 0 Pmax2 Pmax3 Pmax4 Pmax5 Pmax6 Pmax7 Pmax8]
V=[0 0.1 0.2 0.3 0.4 0.5 0.6 0.7 0.8]

% Power (P) vs. Water Speed (V) for Hybrid Turbine

plot(V,P), grid on
%title('Power vs. Water Speed for HYBRID Turbine')
xlabel('Water Speed,V (m/s)')
ylabel('Power output, P (Watt)')

% Power Comparison

V=[0.1 0.2 0.3 0.4 0.5 0.6 0.7 0.8]
ph=[0 0.7373 1.8342 2.2351 9.2201 16.0261 17.8774 21.2545]
V1=[0.1 0.2 0.3 0.4 0.5 0.6 0.7]
pd=[0 0.0555 1.1508 3.1171 5.9550 13.4786 18.5]

```

```
ps=[0 0 0 0.1365 0.2669 0.4612 0.7323 1.093]
```

```
plot(V,ph,'r',V,ps,V1,pd)
grid on
%title('Power vs. Water Speed')
xlabel('Water Speed,V (m/s)')
ylabel('Power output,P (Watt)')
```

B.2

▪ Power (P) vs. Turbine Speed (ω in rad/s) for Hybrid Turbine

```
clc;
```

```
w3=[1.6539 1.6592 1.7163 1.7372];
pt3=[1.8342 1.4885 1.2568 1.1533];
w4=[2.3974 2.4265 2.4590 2.4546];
pt4=[2.2351 1.8884 1.6876 1.6803];
w5=[2.6073 2.7098 2.7116 2.7973 2.8638 2.8988 2.9683 3.0189 3.1114];
pt5=[9.2201 8.6760 8.6473 7.6139 6.9279 5.7090 4.7580 4.0316 3.3678];
w6=[3.2153 3.3049 3.4344 3.4115 3.4863 3.5323 3.5619 3.6326 3.6803];
pt6=[16.0261 14.7380 13.6992 12.0266 10.3456 8.9957 7.3941 6.0777 4.5186];
w7=[3.7488 3.7780 3.8101 3.8820 3.9064 3.9461 4.0046 4.0134 4.0540 4.0568];
pt7=[16.844 16.7653 14.9283 12.1551 10.2734 8.1837 5.8463 4.1416 3.3052 2.9367];
w8=[4.1063 4.0862 4.1734 4.2314 4.2571 4.2881 4.3014 4.3911 4.3448];
pt8=[21.2545 19.2220 16.8322 14.7902 12.6602 9.9596 7.5053 4.4864 3.2308];
```

```
plot(w3,pt3,w4,pt4,w5,pt5,w6,pt6,w7,pt7,w8,pt8),grid
xlabel('Turbine Speed,w (rad/s)')
ylabel('Power (Watt)')
```

B.3

▪ Power Coefficient (C_p) vs. TSR (λ) for Hybrid Turbine

```
clc;
%0.3 m/s
```

```
p3=(0.5*1000*1*(0.3)^3);
w3=[1.6539 1.6592 1.7163 1.7372];
lamda3=(w3*0.5)./0.3;
pt3=[1.8342 1.4885 1.2568 1.1533];
cp3=pt3./p3;
```

```
tsr3max=max(lamda3);
tsr3min=min(lamda3);
cp33max=max(cp3)
cp33min=min(cp3);
```

%0.4 m/s

```
p4=(0.5*1000*1*(0.4)^3);
w4=[2.3974 2.4265 2.4590 2.4546];
lamda4=(w4*0.5)/0.4;
pt4=[2.2351 1.8884 1.6876 1.6803];
cp4=pt4./p4;
```

```
tsr4max=max(lamda4)
tsr4min=min(lamda4);
cp44max=max(cp4)
cp44min=min(cp4);
```

%0.5 m/s

```
p5=(0.5*1000*1*(0.5)^3);
w5=[2.6073 2.7098 2.7116 2.7973 2.8638 2.8988 2.9683 3.0189 3.1114];
lamda5=(w5*0.5)/0.5
pt5=[9.2201 8.6760 8.6473 7.6139 6.9279 5.7090 4.7580 4.0316 3.3678];
cp5=pt5./p5
```

```
tsr5max=max(lamda5)
tsr5min=min(lamda5);
cp55max=max(cp5)
cp55min=min(cp5);
```

% 0.6 m/s

```
p6=(0.5*1000*1*(0.6)^3);
w6=[3.2153 3.3049 3.4344 3.4115 3.4863 3.5323 3.5619 3.6326 3.6803];
lamda6=(w6*0.5)/0.6
pt6=[16.0261 14.7380 13.6992 12.0266 10.3456 8.9957 7.3941 6.0777 4.5186];
cp6=pt6./p6
```

```
tsr6max=max(lamda6)
tsr6min=min(lamda6);
cp66max=max(cp6)
cp66min=min(cp6);
```

%0.7 m/s

```

p7=(0.5*1000*1*(0.7)^3);
w7=[3.7488 3.7780 3.8101 3.8820 3.9064 3.9461 4.0046 4.0134 4.0540 4.0568];
lamda7=(w7*0.5)./0.7;
pt7=[16.844 16.7653 14.9283 12.1551 10.2734 8.1837 5.8463 4.1416 3.3052 2.9367];
cp7=pt7./p7;

```

```

tsr7max=max(lamda7)
tsr7min=min(lamda7);
cp77max=max(cp7)
cp77min=min(cp7);

```

%0.8 m/s

```

p8=(0.5*1000*1*(0.8)^3);
w8=[4.1063 4.0862 4.1734 4.2314 4.2571 4.2881 4.3014 4.3911 4.3448];
lamda8=(w8*0.5)./0.8;
pt8=[21.2545 19.2220 16.8322 14.7902 12.6602 9.9596 7.5053 4.4864 3.2308];
cp8=pt8./p8;

```

```

tsr8max=max(lamda8)
tsr8min=min(lamda8);
cp88max=max(cp8)
cp88min=min(cp8);

```

```

TSR=[lamda3,lamda4,lamda5,lamda6,lamda7,lamda8];
Cp=[cp3,cp4,cp5,cp6,cp7,cp8];

```

```

MaximumTSR=max(TSR)
MinimumTSR=min(TSR);
MaximumCp=max(Cp)
MinimumCp=min(Cp);

```

```

plot(lamda3,cp3,lamda4,cp4,lamda5,cp5,lamda6,cp6,lamda7,cp7,lamda8,cp8),grid
xlabel('TSR')
ylabel('Power Coefficient(Cp)')

```

Appendix C

C.1

▪ Design of Boost Converter

```

clc;
fs=10000;           % Switching frequency
ripple=0.001;      % Voltage ripple
vfw=0.7;           % Free Wheeling diode voltage
gain=3;
vin=0:0.5:10       % Input Voltage
vout= gain.*vin    % Output Voltage
d=(vout-vin)./vout; % Duty Ratio Calculation
t=1/fs;           % Time Period
ton=d.*t;         % Switching ON time
toff=(1-d).*t;    % Switching OFF time
r=50;             % 50 Ω Load
lmin=(r./(2*fs)).*d.*(1-d).*(1-d); % Minimum inductance for conduction model
l=1.2*lmin; % Inductance for this designed converter
c=d/(ripple*r.*fs); % Capacitance for this designed converter for ripple elimination

```

C.2

▪ Boost Converter's V_{out} vs. V_{in} , (Theoretical and Experimental)

```
% Experimental data
```

```

vin_Exp = [0 0.495 1.006 1.546 2.177 2.407 2.937 3.604 4.085 4.48 5.022 5.514 6.114
6.6 6.964 7.555 7.96 8.561 9.075 9.58 10.07];
vout_Exp = [0 0.776 1.876 3.116 4.57 5.11 6.35 7.95 9.06 9.99 11.28 12.43 13.86 15.04
15.92 17.32 18.31 19.75 21.03 22.25 23.36];

```

```
%Plot
```

```

plot(vin,vout,vin_Exp,vout_Exp),grid
xlabel('Input Voltage ( Vin )');
ylabel('Output Voltage ( Vout )');

```

C.3

- **Boost Converter's I_{out} vs. V_{out} , (Theoretical and Experimental)**

```
iout=vout/r;
```

```
% Experimental data
```

```
vout_Exp=[0 0.776 1.876 3.116 4.57 5.11 6.35 7.95 9.06 9.99 11.28 12.43 13.86 15.04  
15.92 17.32 18.31 19.75 21.03 22.25 23.36];
```

```
iout_Exp=[0 0.01 0.03 0.05 0.08 0.09 0.12 0.15 0.17 0.19 0.22 0.24 0.27 0.29 0.31 0.34  
0.35 0.38 0.41 0.43 0.46];
```

```
%Plot
```

```
plot(vout,iout,vout_Exp,iout_Exp),grid  
xlabel('Output Voltage ( Vout )');  
ylabel('Output Current ( Iout )');
```

C.4

- **Boost Converter's P_{out} vs. V_{in} , (Theoretical and Experimental)**

```
iout=vout/r;  
pout=vout.*iout;
```

```
% Experimental
```

```
vout_Exp=[0 0.776 1.876 3.116 4.57 5.11 6.35 7.95 9.06 9.99 11.28 12.43 13.86 15.04  
15.92 17.32 18.31 19.75 21.03 22.25 23.36];
```

```
iout_Exp=[0 0.01 0.03 0.05 0.08 0.09 0.12 0.15 0.17 0.19 0.22 0.24 0.27 0.29 0.31 0.34  
0.35 0.38 0.41 0.43 0.46];
```

```
pout_Exp=[0 0.00776 0.05628 0.1558 0.3656 0.4599 0.762 1.1925 1.5402 1.8981 2.4816  
2.9832 3.7422 4.3616 4.9352 5.8888 6.4085 7.505 8.6223 9.5675 10.7456];
```

```
%Plot
```

```
plot(vin,pout,vin_Exp,pout_Exp),grid  
xlabel('Input Voltage ( Vin )');  
ylabel('Output Power ( Pout )');
```

C.5

- **Boost Converter's Efficiency (%) vs. V_{in} , (Experimental)**

```
iout=vout/r;
pout=vout.*iout;
```

```
% Experimental
```

```
vin_Exp=[0 0.495 1.006 1.546 2.177 2.407 2.937 3.604 4.085 4.48 5.022 5.514 6.114 6.6
6.964 7.555 7.96 8.561 9.075 9.58 10.07];
iin_Exp=[0 0.05 0.12 0.2 0.3 0.33 0.42 0.52 0.59 0.66 0.74 0.82 0.91 0.98 1.04 1.14 1.2
1.3 1.38 1.46 1.53];
pin_Exp=[0 0.02475 0.12072 0.3092 0.6531 0.79431 1.23354 1.87408 2.41015 2.9568
3.71628 4.52148 5.56374 6.468 7.24256 8.6127 9.552 11.1293 12.5235 13.9868
15.4071];
vout_Exp=[0 0.776 1.876 3.116 4.57 5.11 6.35 7.95 9.06 9.99 11.28 12.43 13.86 15.04
15.92 17.32 18.31 19.75 21.03 22.25 23.36];
iout_Exp=[0 0.01 0.03 0.05 0.08 0.09 0.12 0.15 0.17 0.19 0.22 0.24 0.27 0.29 0.31 0.34
0.35 0.38 0.41 0.43 0.46];
pout_Exp=[0 0.00776 0.05628 0.1558 0.3656 0.4599 0.762 1.1925 1.5402 1.8981 2.4816
2.9832 3.7422 4.3616 4.9352 5.8888 6.4085 7.505 8.6223 9.5675 10.7456];
E=((pout_Exp*100)./pin_Exp);
```

```
%Plot
```

```
plot(vin_Exp,E),grid
xlabel('Input Voltage ( Vin )');
ylabel('Efficiency ( % )');
```

Appendix D

D.1

```

#include <16f877.h>
#DEVICE *=16 ADC=10
#fuses HS,NOWDT,NOPROTECT,NOLVP
#use Delay(Clock=20000000)
#use rs232(baud=9600,xmit=PIN_C6,rcv=PIN_C7)
#include <lcd.c>

//Constants and variables initialization

CONST byte v_in=0,v_out=1,i_out=2;
float output_power,input_power,old_o_power,out_p,in_p;
float vo,io,ii,vi;
int j;

// ADC Channel reading with average value

float analog_channel(byte ch){
int i, av_n=20;
float ag=0;
set_adc_channel(ch);
delay_us(10);
for (i=1;i<=av_n;++i){
ag+=read_adc();
delay_us(10);
}
return(ag/av_n);
}

//Output Power Calculation

void o_p(){
vo=analog_channel(v_out)*0.01955034; //delay_us(20)0.01955034,0.01965
io=((analog_channel(i_out)*0.049657869)-(25.3)); //io=(ir*10.16)-25.3;
//io=((analog_channel(i_out)*0.049657869)-(25.16));
output_power=vo*io; //delay_ms(100);
//io=io*10;
}

```

```
//input Power Calculation
```

```
void i_p(){
vi=analog_channel(v_in)*0.019550342;
ii=((io)/(1-(j/128)));
input_power=vi*ii;
}
```

```
void main(){
```

```
// Hardware initialization
```

```
setup_adc(adc_clock_div_32);
setup_timer_2(T2_DIV_BY_4,127,1); // change for 10K
setup_ccp2(CCP_PWM);
set_pwm2_duty(j);
setup_port_a(ALL_ANALOG);
j=64;
lcd_init();
old_o_power = 0;
```

```
elooop:
```

```
i_p();
o_p();
```

```
if (vi<=8) {
output_low(PIN_B0);
goto elooop;
}
else if (vi>8){
output_high(PIN_B0);
goto elooop;
}
```

```
if(vo>=14){
if(old_o_power>output_power){
j++;
set_pwm2_duty(j);
if(old_o_power<output_power){
j--;
set_pwm2_duty(j);
}
```

```

    }
}

if(vo<14){
    if(old_o_power>output_power){
        j--;
        set_pwm2_duty(j);
        if(old_o_power<output_power){
            j++;
            set_pwm2_duty(j);
        }
    }
}

output_power=old_o_power;

if(j>100){
    j=100;
    if(j<10){
        j=10;
    }
}

output_high(PIN_B1);

//LCD Display

lcd_putc('\f'); // clear the lcd
printf(lcd_putc, "vi=%4.2F",vi);
printf(lcd_putc, " ii=%4.2F \n",ii);
printf(lcd_putc, "vo=%4.2F",vo);
printf(lcd_putc, " io=%4.2F \n",io);

//Hyperterminal Display

printf("Input = ");
printf("%4.2F %4.2F %4.2F \n \r"ii,vi,in_p);
printf("Output = ");
printf("%4.2F %4.2F %4.2F \n \r"io,vo,out_p);
delay_us(500);
goto eloop;
}

```

